THE UNIVERSITY OF CHICAGO

SELF-ASSEMBLED HYBRID NANOMATERIALS FOR SYNERGISTIC CHEMOTHERAPY, CHEMOIMMUNOTHERAPY, AND PHOTODYNAMIC THERAPY OF CANCERS

A DISSERTATION SUBMITTED TO

THE FACULTY OF THE DIVISION OF THE PHYSICAL SCIENCES

IN CANDIDACY FOR THE DEGREE OF

DOCTOR OF PHILOSOPHY

DEPARTMENT OF CHEMISTRY

BY

WENBO HAN

CHICAGO, ILLINOIS

MARCH 2021

Table of Contents

List of Figures

List of Tables

List of Abbreviations

°C	Degrees Celsius
$^1O_2$	Singlet oxygen
ADC	Antibody-drug conjugate
AO	Acridine orange
Apo B-100	Apolipoprotein B-100
AUC	Areas under curve
BD	Biodistribution
BOD	4-(5,5-Difluoro-1,3,7,9-tetramethyl-5H-4l4,5l4-dipyrrolo[1,2-c:2',1'-f][1,3,2]diazaborinin-10-yl)benzoic acid
BODIPY	Boron-dipyrromethene
BSA	Bovine serum albumin
CAnP	CisPt and nab-PTX
Chol	Cholesterol
Chol-S-S-OH	Cholest-5-en-3-ol (3β)-, 3-(2-((2-hydroxyethyl)disulfanyl)ethyl) carbonate
CisPt	Cisplatin
CLSM	Confocal laser scanning microscopy
CRC	Colorectal cancer
CRT	Calreticulin
DAMP	Damage-associated molecular pattern
DC	Dendritic cell
DCM	Dichloromethane
DFO	Deferoxamine
DHA	Dihydroartemisinin

DIPEA	N,N-Diisopropylethylamine
DLS	Dynamic light scattering
DMAP	4-N,N-dimethylaminopyridine
DMF	N,N-dimethylformamide
DMSO	Dimethyl sulfoxide
DOPA	1,2-Dioleoyl-sn-glycero-3-phosphate
DOPC	1,2-Dioleyl-sn-glycero-3-phosphocholine
DSB	DNA double-strand break
DSPE-PEG2k	1,2-Diastearoyl-sn-glycero-3-phosphoethanolamine-N-[amino(polyethylene glycol)2000]
EDCI	1-Ethyl-3-(3-dimethylaminopropyl)carbodiimide hydrochloride
EM	Electron microscopy
EPR	Enhanced permeability and retention
ER	Endoplasmic reticulum
EtOAc	Ethyl acetate
FDA	Food and Drug Administration
Fer-1	Ferrostatin 1
FL-NCP	Fluorescently labeled NCP
GPX4	Glutathione peroxidase 4
GSH	Glutathione
H&E	Haematoxylin and eosin
H_2-DCFDA	2′,7′-Dichlorodihydrofluorescin diacetate
HDL	High-density lipoprotein
HR-MS	High-resolution mass spectrometry
i.p.	Intraperitoneal

i.v.	Intravenous
ICD	Immunogenic cell death
ICP-MS	Inductively coupled plasma-mass spectrometry
IDL	Intermediate-density lipoprotein
ISTD	Internal standard
LC-MS	Liquid chromatography-mass spectrometry
LDL	Low-density lipoprotein
LMP	Lysosomal membrane permeabilization
LPL	Lipoprotein lipase
MPS	Mononuclear phagocyte system
MRT	Mean retention time
MTS	(3-(4,5-Dimethylthiazol-2-yl)-5-(3-carboxymethoxyphenyl)-2-(4-sulfophenyl)-2H-tetrazo¬lium)
NCP	Nanoscale coordination polymer
NIR	Near-infrared
NMR	Nuclear magnetic resonance
NP	Nanoparticle
OxPt	Oxaliplatin
PBS	Phosphate buffered saline
PD-1	Programmed cell death protein 1
PDI	Polydispersity index
PD-L1	Programmed death ligand 1
PDT	Photodynamic therapy
PEG	Polyethylene glycol
PK	Pharmacokinetic

PS	Photosensitizer
PTFE	Polytetrafluoroethylene
PTX	Paclitaxel
PUFA	Polyunsaturated fatty acid
ROS	Reactive oxygen species
siRNA	Small interfering RNA
SOSG	Singlet oxygen generation green
TEM	Transmission electron microscopy
TGI	Tumor growth inhibition index
UV-vis	Ultraviolet and visible
VLDL	Very low-density lipoprotein
ZnP	Zn-pyrophosphate

Abstract

Wenbo Han: Self-Assembled Hybrid Nanomaterials For Synergistic Chemotherapy, Chemoimmunotherapy, And Photodynamic Therapy Of Cancers

Under the Direction of Professor Wenbin Lin

Although chemotherapeutic anticancer drugs have been developed and used in clinical practices for more than 80 years, there still exist many unsolved problems and limitations, including low bioavailability and high systemic toxicity. Moreover, different drugs usually do not share the same physicochemical properties and behave differently inside the body, which makes it difficult to combine multiple drugs to overcome resistance to one single drug or to achieve a synergetic effect. Nanoscale coordination polymer (NCP) is a nanoparticle platform that can load drugs with different physicochemical properties within a single particle by incorporating hydrophilic drugs inside its Zn-phosphate solid core and inserting hydrophobic drugs between its lipid bilayers. The drug-loaded particles are long-circulating and tumor-targeting. Evidence showed that when delivered by the NCP platform, drugs showed increased drug exposure and reduced systemic toxicity.

Chapter 1 of this thesis discussed the current application and limitations of chemotherapeutic drugs and strategies to overcome the limitations, with a focus on nanoparticle formulation and prodrug design.

Chapter 2 and Chapter 3 described two examples of using the NCP platform to deliver molecules that can cause immunogenic cell death. The combination of oxaliplatin and dihydroartemisinin showed high immunogenicity, while the combination of dihydroartemisinin and iron complexes triggered immunogenic ferroptosis. Both examples

showed long circulation of loaded prodrugs and low toxicity with improved anticancer efficacy when compared to free drugs. They synergized with α-PD-L1 immunotherapy in immunosuppressive tumor models.

Chapter 4 showed improvement of the well-established combination of cisplatin and paclitaxel therapy using the NCP platform. Detailed studies revealed the interaction between NCP particles and low-density lipoproteins and its influence on tumor-targeting effect of NCP particles.

Chapter 5 further extended the scope of stable nanoparticles via self-assembly of amphiphilic molecules. Lysosome-targeting dyes self-assembled into nanoparticles and showed high tumor accumulation and great efficacy in photodynamic therapy.

Acknowledgement

It is such a memorable period for me to work with so many talented and kind people in the Lin group during the past five years. Without their help and strong support, it would not have been possible for me to finish my research projects.

I would like to first express my thanks to my advisor Professor Wenbin Lin for providing me the great opportunity to work in his lab that gathered talented minds for solving real problems and his kind advice on my research. He guided me into a broad area from material chemistry and medicinal chemistry all the way to clinical studies. What touched me the most is his insight into real problems rather than artifacts. By looking deeply into each experiment, he is always able to unmask unexpected phenomena and point out the key problem. He also trained me to think into experimental details of research results rather than simply accept other's conclusions. Other than the help in research, Wenbin is also a kind person to share opinions about life experience and provide strong encouragement whenever I feel discouraged. I will bring his lessons on research and life with me and look forward to future interactions.

I also want to thank my thesis committee: Professor John Anderson and Professor Weixin Tang, for reviewing my dissertation. It is my pleasure to present my research and I am grateful for their suggestions.

There are many great scientists who shared their research experiences and taught me skills. I would like to thank Dr. Xiaopin Duan, Dr. Christina Chan, Dr. Chunbai He, Dr. Kaiting Yang, and Dr. Nining Guo for their help in biology-related research. Dr. Xiaopin Duan and Dr. Christina Chan helped a lot in the biological parts of my research. They trained me from culturing cells, taking confocal images to inoculating tumors and testing efficacy. I

used to be a green hand with no experience in any biology-related task, but now able to understand the biological aspect of each project with their help. Dr. Chunbai He, Dr. Kaiting Yang, and Dr. Nining Guo also taught me many useful skills and provided deep discussions on my research. I would also like to thank Dr. Zekai Lin and Dr. Nathan Thacker for their advice on organic synthesis and characterization. It was a great time working with Zekai and Nathan solving problems in synthetic chemistry. I also want to extend my thanks to Dr. Jianqin Lu and Dr. Xiang Ling. They introduced me to many research fields and provided encouragement.

I would also like to thank my fellow labmates. It is my luck to spend years with these talented minds and got help from them. Xiaomin Jiang worked with me on many projects and we had a great time discussing fine details of each experiment and other topics in our life as good friends. Deyan Gong shared a lot of his experience on photosensitizer-related projects and is such a kind guy to work with.

I would also like to especially thank Dr. Kaiyuan Ni and Dr. Guangxu Lan. As my close friends, they not only helped me with my research but also planned many interesting activities. Another close friend that I want to thank is Dr. Pengfei Ji. Although working on different fields, we share the same opinions on many topics and his questions often provide me new views of my research. I hope one day we can have our planned trip to Ethiopia.

I also want to thank my friends Rui Ge and Junyi Xie in financial companies. In the hardest time of my research, they made me believe that I should do something as a scientist to solve real problems and improve human life rather than simply giving up. My previous roommates Dr. Kuangda Lu and Dr. Tong Wu also helped me a lot in my life. Both of them are good chefs and we spent a great time living together. Dr. Zeqi Xu from Coordination

Pharmaceutical Inc. is like a kind uncle to me and shared lots of experiences both in research and in life. With his strong support, some of my projects are now in clinical studies and hopefully one of them may bring real benefits to cancer patients.

I also want to thank Yang Song, Xuanyu Feng, Taokun Luo, Zhe Li, Dr. Shuyi Li, Kui Yang, Ziwan Xu, Dr. Yangjian Quan, Jianqiao Liu, Youyou Li, Dr. Yingying Li, Geoffrey Nash, Wenjie Shi and other current and previous group members for their support and friendship.

Finally, I want to thank my family, especially my parents, Kongying Wang and Zhenguo Han. I left my hometown living with unfamiliar languages and culture for nine years. I would never imagine surviving abroad without their love and encouragement. I look forward to spending more time with them after graduation.

Chapter 1. Introduction to Cancer Therapy and Nanomedicine

1.1 Chemotherapy of cancer

Cancer is currently the second leading cause of death in the United States with about 1,762,540 new cases and 606,880 deaths reported in 2019.[1] Lung cancer, breast cancer, and colon cancer are among the leading types of cancer that caused deaths.[1] Surgery, radiotherapy, chemotherapy, and immunotherapy are widely used in the treatment of cancer.[2-4]

Since the discovery of nitrogen mustard activity towards lymphoma in 1940s[5], many chemotherapeutic drugs based on a variety of mechanisms have been developed (**Figure 1-1**). Among them, one of the most important discoveries is cisplatin in the late 1960s and its approval by the US Food and Drug Administration (FDA) in 1978.[6] Two other platinum drugs, carboplatin and oxaliplatin were developed later and received FDA approval in 1989 and 2004, respectively. By crosslinking DNAs in cancer cells, platinum-based anticancer drugs can cause DNA double-strand breaks to block DNA replication and many other effects to damage cancer cells.[7-9] Most platinum-based drugs lack hydrophobic groups so that they can form aqueous solutions and be infused into patients via intravenous injection easily. However, for the same reason, they can be easily cleared via kidneys without significant deposition in tumor cells.[10] As a result, cisplatin causes severe renal toxicity in many patients and can only be administered with aggressive hydration before and after cisplatin infusion.[11] Carboplatin has a worse leaving group and has the same mode of action as cisplatin. Carboplatin is thus much less cytotoxic than cisplatin and does not cause renal toxicity. However, carboplatin is administered at a much higher dose than cisplatin and can cause myelosuppression in some patients, leading to severe neutropenia and

thrombocytopenia in the clinic.[12, 13] Oxaliplatin is not particularly cytotoxic but is a backbone of many combination chemotherapy regimens such as FOLFOX (oxaliplatin, 5-fluorouracil, and folinic acid), CAPOX (capecitabine and oxaliplatin), and FOLFIRINOX (oxaliplatin, 5-fluorouracil, folinic acid, and irinotecan) for treating gastrointestinal cancers.[14] Oxaplatin is known to cause debilitating peripheral neuropathy in a significant percentage of colorectal cancer patients and this dose limiting toxicity is responsible for treatment failure among these patients.[15, 16]

Organic chemotherapeutic drugs based on a number of modes of actions were developed during the past 80 years.[5] For example, paclitaxel shows anticancer activity by binding with tubulin and preventing cancer cell division.[17] Irinotecan, the prodrug to the active metabolite SN38, works as a topoisomerase 1 inhibitor.[18, 19] The hydrophobic drug paclitaxel has to be administered using the surfactant cremophor, which can cause severe allergic reactions in some patients.[20] In addition, paclitaxel frequently causes neutropenia, anemia, peripheral neuropathy, nausea and vomiting, diarrhea, and alopecia.[21] Irinotecan was designed to be water soluble in its salt form but is known to cause severe and life-threatening neutropenia and diarrhea in some patients.[22, 23] Many organic drugs originally designed for treating other diseases that show anticancer activities also have poor bioavailability. For example, dihydroartemisinin is the active form of the most important anti-malaria drug, artemisinin. Dihydroartemisinin generates cytotoxic reactive oxygen species (ROSs) by breaking its peroxide bridge.[24] This process is catalyzed by free heme in parasites and provides the clinical benefit even with poor bioavailability.[25] Although many organic drugs were engineered to be more hydrophilic for better bioavailability,[26] some of them are still too hydrophobic to form aqueous solutions. Clinically, solubilizers

such as cremophor are generally used to dissolve or form emulsions of organic drugs before intravenous infusions.[27] These solubilizers can cause hypersensitivity reactions that can be even fatal in some patients.[20] There are thus significant problems with even the best chemotherapeutic drugs in terms of their adverse event profiles and tolerability.

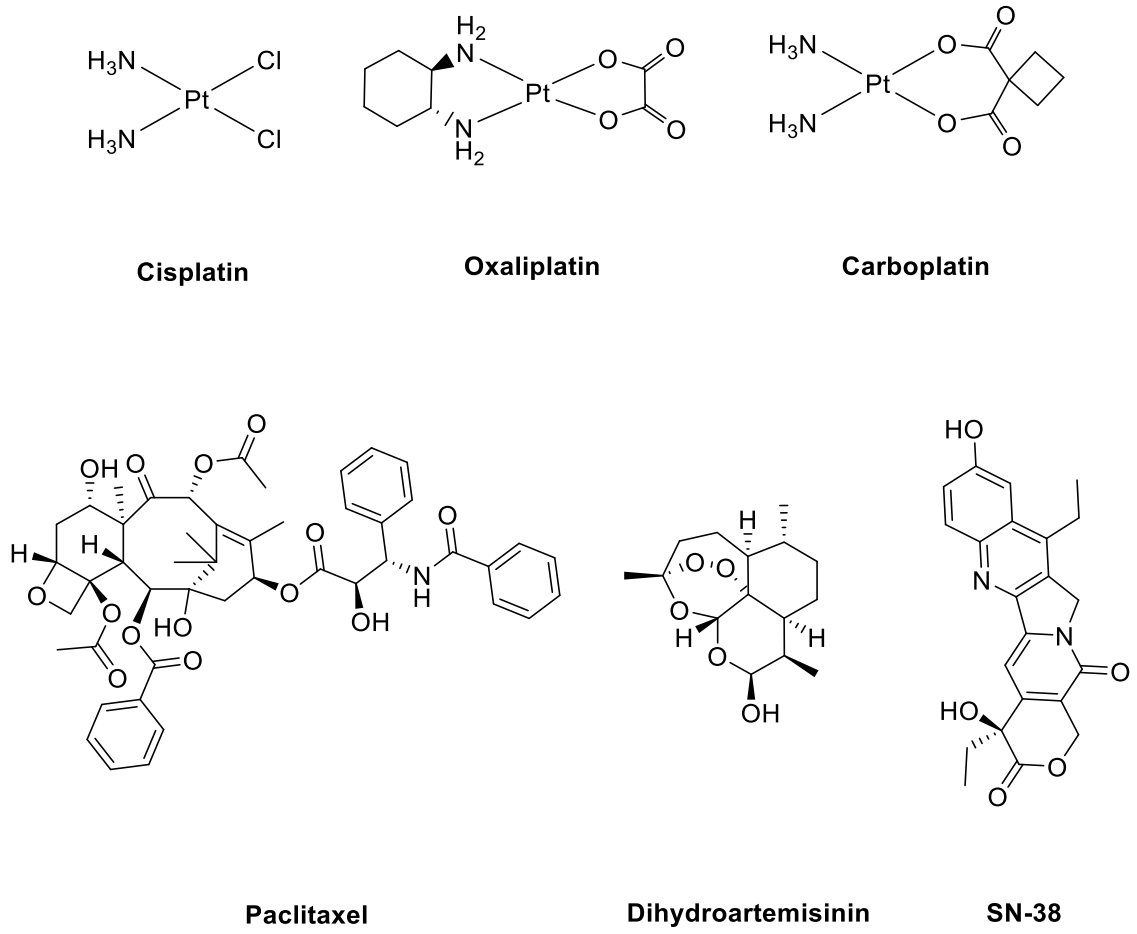

Figure 1-1. Structures of select molecules that show anticancer activities.

In clinical practice, patients are usually treated with two or three types of anticancer drugs simultaneously to overcome resistance to one single drug or to achieve synergetic effect.[4]

This practice brings additional challenges as these drugs do not share the same physicochemical properties and behave differently inside the body. To solve these problems, researchers have made many attempts to increase bioavailability or to alter adverse effect profiles to increase the therapeutic indices of conventional chemotherapies. Among these approaches, nanoparticle delivery and prodrug design have been shown to be successful for some chemotherapies.

1.2 Nanoparticles for drug delivery

Nanoparticles (NPs) are sub-micrometer sized materials. Their small size and high surface area provided unique properties comparing with traditional bulk materials and homogeneous solutions.[28] In clinical applications, NPs are mainly used for improving solubility and bioavailability or reduce systemic toxicity.

Among all FDA approved nanoparticle-based drugs, liposomal NPs like Onivyde®[29] and Doxil®[30] have already shown great success in cancer treatment.[31] Although they have different components and synthesis strategies, liposomal NPs share some common features that make them suitable for clinical applications. They usually have drugs loaded inside the particles with bio-mimicking lipid bilayers on their surface.[29, 32] In some cases, they are further coated by hydrophilic compounds like sucrose octasulfate or polyethylene glycol (PEG) that can trap an aqueous layer surrounding the particle.[32] These surface properties can not only stabilize particles in aqueous solution but also prevent the adsorption of plasma proteins, thus making it difficult for recognition and clearance by the mononuclear phagocyte system (MPS). By avoiding the major clearance pathway, these NPs can have prolonged circulation times in blood and improve drug exposure.[33, 34] Since the bio-

mimicking lipid bilayers of those NPs are usually made of natural phospholipids and cholesterol, the toxicity of these vehicles is minimal.[29]

The enhanced permeability and retention (EPR) effect is also believed to be one of the unique properties of NPs that can benefit cancer treatment. Due to rapid growth of tumors and high demand of nutrients and oxygen by cancer cells, freshly formed blood vessels in tumors usually contain poorly aligned or defective endothelial cells, making them leaky to small particles of a certain size (<200 nm).[35, 36] Small NPs can penetrate through these leaky structures and accumulate in tumors at higher concentrations than in normal tissues, making them passively targeted to tumor sites hence improving efficacy and reducing systemic toxicity (**Figure 1-2**).[35]

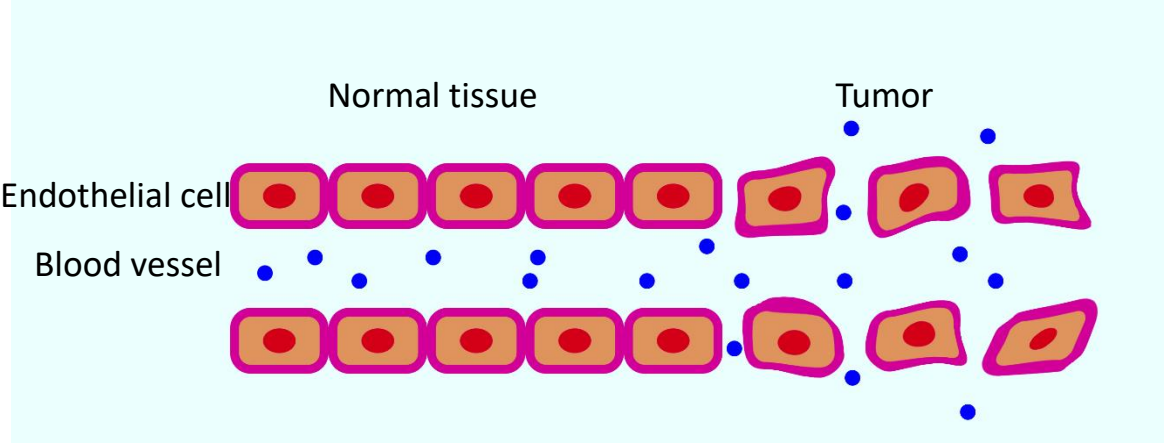

Figure 1-2. Illustration of the EPR effect.

1.3 Prodrugs for cancer drug delivery

Many of organic cancer drugs originated from screening of natural products against a panel of cancer cell lines. The identified hits (such as SN38 and podophyllotoxin) tend to have

poor water solubility and bioavailability. Extensive efforts have been made to design prodrugs of these hits to increase the therapeutic indices. Prodrugs are biodegradable molecules that can release active drugs when cleaved by certain enzymes or via other mechanisms inside the body.[37] By modifying active drugs through biodegradable linkages, prodrugs can overcome issues in circulation, absorption, excretion, etc. caused by unfavorable physiochemical properties of the original active drugs. The prodrug strategy is widely used in small molecule drugs and about 10% of marketed drugs can be considered as prodrugs.[37] It is commonly used for improving aqueous solubility, passive permeability and metabolic stability.[38-40] In some cases, by taking advantage of site-specific enzymes, prodrugs can achieve targeted delivery of active drugs.[41, 42] For example, the carbamate linkage of irinotecan can be selectively cleaved in liver and in cancer cells by carboxyesterase to the active SN38, which not only address the poor solubility of SN38 but also enhances its tumor exposure.[43] Etoposide is not strictly a prodrug of podophyllotoxin but a synthetic derivative of podophyllotoxin with enhanced antitumor efficacy and reduced side effects.[44]

Similar concepts have also been widely applied to antibody-drug conjugates (ADCs). Instead of using small molecules or functional groups to shape active drugs, ADCs link drug molecules via biodegradable linkages to long-circulating, targeting antibodies.[45] Since most ADCs require the release of drugs during or after endosomal uptake, the chemical strategies used in ADCs are fewer than that in small molecule prodrugs. Cleavable ADC linkers usually have one or more of the three properties: protease-sensitive, acid-sensitive, and glutathione-sensitive, corresponding to intracellular protease like

cathepsin B, low endosomal/lysosomal pH (pH=4-6), and high intracellular glutathione (GSH) concentration (usually >5 mM in cancer cells) (**Figure 1-3**).[46]

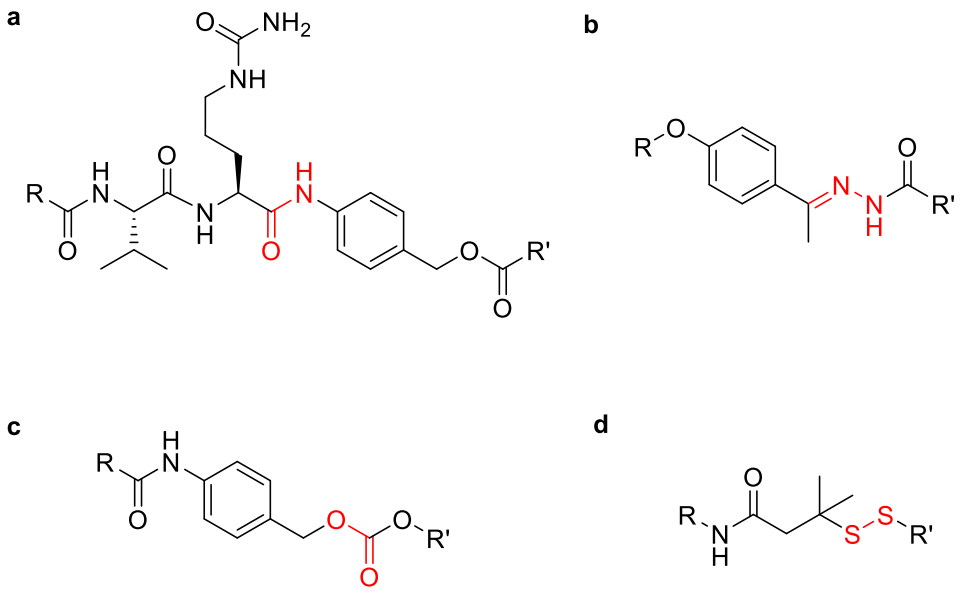

Figure 1-3. Structures of select ADC linkers which are protease-sensitive (a), acid-sensitive (b, c), and GSH-sensitive (d). Functional groups labeled in red can be cleaved under appropriate conditions.

1.4 Nanoscale coordination polymers (NCPs) for drug delivery

The Lin group has developed core-shell nanoscale coordination polymers (NCPs) for cancer therapy.[47-55] Core-shell NCPs take advantage of both nanoparticle delivery and prodrug strategy to enable the co-delivery of important combination chemotherapy regimens. An NCP particle has a solid nontoxic zinc phosphate core and a surrounding lipid bilayer made of cholesterol and natural phospholipids with polyethylene glycol (PEG) (**Figure 1-4**). NCPs share similar size and surface properties with liposomes which make them long-circulating and tumor targeting. The zinc phosphate core allows the entrapment

of hydrophilic cancer drugs such as cisplatin, carboplatin, oxaliplatin, gemcitabine monophosphate, and small interfering RNAs. The space inside the lipid bilayer is hydrophobic enough to trap organic drugs. This unique structure allows for co-delivery of both hydrophilic and hydrophobic drugs within one particle. With multiple drugs of different physicochemical properties on the same particle, the behaviors of different drugs can be relatively well-controlled and studied, allowing for more rational choices of drug combinations and better anticancer efficacy.

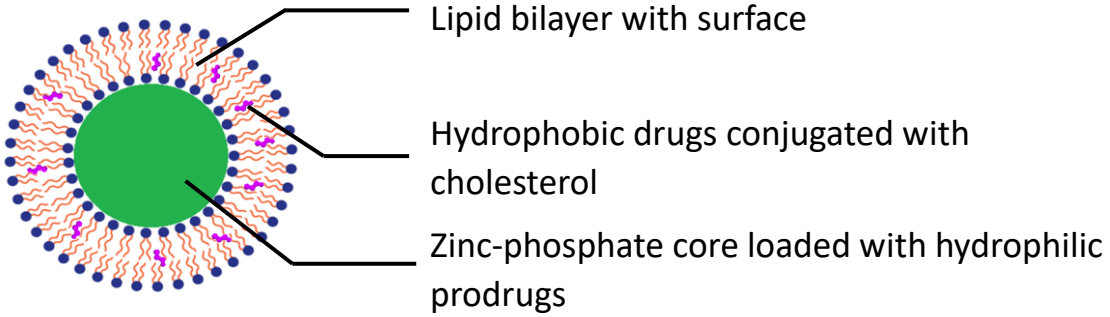

Figure 1-4. Illustration of the structure of a typical NCP particle.

To make use of both the core and shell parts of the NCP particle, both hydrophilic platinum drugs and hydrophobic organic drugs need to be modified using the prodrug strategy. Phosphate groups were installed on platinum drugs to allow for crosslinking by Zn^{2+} ion to form the solid core, while cholesterol molecule was conjugated to organic drugs for hydrophobicity and suitable geometry to fit into the lipid bilayer.

The NCP platform is not limited to the co-delivery of known small molecule anticancer drugs. By similar chemical modifications, other moieties such as photosensitive dyes,

catalysts and even large biomolecules like small interfering RNAs (siRNAs) and microRNAs can be loaded on NCPs and delivered to cancer cells. This prospect allows for the development of entirely new nanomedicines for cancer treatment.

1.5 The scope of this thesis

In the following chapters, hydrophobic and hydrophilic drugs were chemically modified into prodrugs and loaded into nanoparticles based on the NCP technology and a related self-assembly strategy. In chapter 2, a combination of oxaliplatin and dihydroartemisinin on an NCP showed not only improved bioavailability and anticancer efficacy, but also strong immunogenicity and synergy with checkpoint blockade immunotherapy. In chapter 3, iron complexes were loaded together with dihydroartemisinin on an NCP to trigger strong ferroptosis in tumors and induce immunogenic cell death to synergize with α-PD-L1 immunotherapy. Chapter 4 showed the combination of cisplatin and paclitaxel on an NCP further improved the well-established combination therapy and enhanced the tumor-targeting by interacting with lipoproteins. Chapter 5 further explored the design of stable particles via self-assembly of amphiphilic fluorescent dyes and the application of this lysosome-targeted nanoparticle for photodynamic therapy. The works described in this thesis illustrate the robustness and great potential of the NCP platform in cancer therapy and point to the potential of developing other novel nanomaterials via molecular self-assembly for biomedical applications.

1.6 References

1. Siegel, R. L.; Miller, K. D.; Jemal, A., Cancer statistics, 2019. *CA: a cancer journal for clinicians* **2019,** *69* (1), 7-34.

2. Schiller, J. H., Current standards of care in small-cell and non-small-cell lung cancer. *Oncology* **2001,** *61* (Suppl. 1), 3-13.

3. Gouvas, N.; Tan, E.; Windsor, A.; Xynos, E.; Tekkis, P. P., Fast-track vs standard care in colorectal surgery: a meta-analysis update. *International journal of colorectal disease* **2009,** *24* (10), 1119-1131.

4. Allemani, C.; Storm, H.; Voogd, A. C.; Holli, K.; Izarzugaza, I.; Torrella-Ramos, A.; Bielska-Lasota, M.; Aareleid, T.; Ardanaz, E.; Colonna, M., Variation in 'standard care'for breast cancer across Europe: a EUROCARE-3 high resolution study. *European Journal of Cancer* **2010,** *46* (9), 1528-1536.

5. DeVita, V. T.; Chu, E., A history of cancer chemotherapy. *Cancer research* **2008,** *68* (21), 8643-8653.

6. Carter, S. K., Cisplatin—past, present and future. In *Platinum coordination complexes in cancer chemotherapy*, Springer: 1984; pp 359-376.

7. Fuertes, M. A.; Castilla, J.; Alonso, C.; Prez, J. M., Cisplatin biochemical mechanism of action: from cytotoxicity to induction of cell death through interconnections between apoptotic and necrotic pathways. *Current medicinal chemistry* **2003,** *10* (3), 257-266.

8. Reedijk, J.; Lohman, P. H. M., Cisplatin: synthesis, antitumour activity and mechanism of action. *Pharmaceutisch Weekblad* **1985,** *7* (5), 173-180.

9. Raymond, E.; Faivre, S.; Woynarowski, J. M.; Chaney, S. G. In *Oxaliplatin: mechanism of action and antineoplastic activity*, 1998; p 4.

10. Daley-Yates, P. T.; McBrien, D. C. H., The mechanism of renal clearance of cisplatin (cis-dichlorodiammine platinum II) and its modification by furosemide and probenecid. *Biochemical pharmacology* **1982,** *31* (13), 2243-2246.

11. Dentino, M.; Luft, F. C.; Yum, M. N.; Williams, S. D.; Einhorn, L. H., Long term effect of Cis-Diamminedichloride platinum (CDDP) on renal function and structure in man. *Cancer* **1978,** *41* (4), 1274-1281.

12. Adams, M.; Kerby, I. J.; Rocker, I.; Evans, A.; Johansen, K.; Franks, C. R., A comparison of the toxicity and efficacy of cisplatin and carboplatin in advanced ovarian cancer. *Acta Oncologica* **1989,** *28* (1), 57-60.

13. Jodrell, D. I.; Egorin, M. J.; Canetta, R. M.; Langenberg, P.; Goldbloom, E. P.; Burroughs, J. N.; Goodlow, J. L.; Tan, S.; Wiltshaw, E., Relationships between carboplatin

exposure and tumor response and toxicity in patients with ovarian cancer. *Journal of clinical oncology* **1992,** *10* (4), 520-528.

14. Sharif, S.; O'Connell, M. J.; Yothers, G.; Lopa, S.; Wolmark, N., FOLFOX and FLOX regimens for the adjuvant treatment of resected stage II and III colon cancer. *Cancer investigation* **2008,** *26* (9), 956-963.

15. Cersosimo, R. J., Oxaliplatin-associated neuropathy: a review. *Annals of Pharmacotherapy* **2005,** *39* (1), 128-135.

16. Saif, M. W.; Reardon, J., Management of oxaliplatin-induced peripheral neuropathy. *Therapeutics and clinical risk management* **2005,** *1* (4), 249.

17. Horwitz, S. B., Taxol (paclitaxel): mechanisms of action. *Annals of oncology: official journal of the European Society for Medical Oncology* **1994,** *5*, S3-6.

18. Chabot, G. G., Clinical pharmacokinetics of irinotecan. *Clinical pharmacokinetics* **1997,** *33* (4), 245-259.

19. Kunimoto, T.; Nitta, K.; Tanaka, T.; Uehara, N.; Baba, H.; Takeuchi, M.; Yokokura, T.; Sawada, S.; Miyasaka, T.; Mutai, M., Antitumor activity of 7-ethyl-10-[4-(1-piperidino)-1-piperidino] carbonyloxycamptothecin, a novel water-soluble derivative of camptothecin, against murine tumors. *Cancer research* **1987,** *47* (22), 5944-5947.

20. Gelderblom, H.; Verweij, J.; Nooter, K.; Sparreboom, A., Cremophor EL: the drawbacks and advantages of vehicle selection for drug formulation. *European journal of cancer* **2001,** *37* (13), 1590-1598.

21. Rowinsky, E. K.; Eisenhauer, E. A.; Chaudhry, V.; Arbuck, S. G.; Donehower, R. C. In *Clinical toxicities encountered with paclitaxel (Taxol®)*, 1993; WB Saunders Ltd: pp 1-15.

22. Kweekel, D.; Guchelaar, H.-J.; Gelderblom, H., Clinical and pharmacogenetic factors associated with irinotecan toxicity. *Cancer treatment reviews* **2008,** *34* (7), 656-669.

23. Marsh, S.; McLeod, H. L., Pharmacogenetics of irinotecan toxicity. *Pharmacogenomics* **2004,** *5* (7), 835-843.

24. Woerdenbag, H. J.; Moskal, T. A.; Pras, N.; Malingré, T. M.; El-Feraly, F. S.; Kampinga, H. H.; Konings, A. W. T., Cytotoxicity of artemisinin-related endoperoxides to Ehrlich ascites tumor cells. *Journal of Natural Products* **1993,** *56* (6), 849-856.

25. Robert, A.; Benoit-Vical, F.; Meunier, B., The key role of heme to trigger the antimalarial activity of trioxanes. *Coordination chemistry reviews* **2005,** *249* (17-18), 1927-1936.

26. Stella, V.; Borchardt, R.; Hageman, M.; Oliyai, R.; Maag, H.; Tilley, J., *Prodrugs: challenges and rewards*. Springer Science & Business Media: 2007.

27. Dorr, R. T., Pharmacology and toxicology of Cremophor EL diluent. *Annals of Pharmacotherapy* **1994,** *28* (5_suppl), S11-S14.

28. Nel, A. E.; Mädler, L.; Velegol, D.; Xia, T.; Hoek, E. M. V.; Somasundaran, P.; Klaessig, F.; Castranova, V.; Thompson, M., Understanding biophysicochemical interactions at the nano–bio interface. *Nature materials* **2009,** *8* (7), 543-557.

29. Zhang, H., Onivyde for the therapy of multiple solid tumors. *OncoTargets and therapy* **2016,** *9*, 3001.

30. Barenholz, Y. C., Doxil®—the first FDA-approved nano-drug: lessons learned. *Journal of controlled release* **2012,** *160* (2), 117-134.

31. Bobo, D.; Robinson, K. J.; Islam, J.; Thurecht, K. J.; Corrie, S. R., Nanoparticle-based medicines: a review of FDA-approved materials and clinical trials to date. *Pharmaceutical research* **2016,** *33* (10), 2373-2387.

32. Drummond, D. C.; Noble, C. O.; Guo, Z.; Hong, K.; Park, J. W.; Kirpotin, D. B., Development of a highly active nanoliposomal irinotecan using a novel intraliposomal stabilization strategy. *Cancer research* **2006,** *66* (6), 3271-3277.

33. Papahadjopoulos, D.; Allen, T. M.; Gabizon, A.; Mayhew, E.; Matthay, K.; Huang, S. K.; Lee, K. D.; Woodle, M. C.; Lasic, D. D.; Redemann, C., Sterically stabilized liposomes: improvements in pharmacokinetics and antitumor therapeutic efficacy. *Proceedings of the National Academy of Sciences* **1991,** *88* (24), 11460-11464.

34. Immordino, M. L.; Dosio, F.; Cattel, L., Stealth liposomes: review of the basic science, rationale, and clinical applications, existing and potential. *International journal of nanomedicine* **2006,** *1* (3), 297.

35. Greish, K., Enhanced permeability and retention (EPR) effect for anticancer nanomedicine drug targeting. In *Cancer nanotechnology*, Springer: 2010; pp 25-37.

36. Matsumura, Y.; Maeda, H., A new concept for macromolecular therapeutics in cancer chemotherapy: mechanism of tumoritropic accumulation of proteins and the antitumor agent smancs. *Cancer research* **1986,** *46* (12 Part 1), 6387-6392.

37. Rautio, J.; Meanwell, N. A.; Di, L.; Hageman, M. J., The expanding role of prodrugs in contemporary drug design and development. *Nature Reviews Drug Discovery* **2018,** *17* (8), 559-587.

38. Burke, J. T.; Wargin, W. A.; Sherertz, R. J.; Sanders, K. L.; Blum, M. R.; Sarubbi, F. A., Pharmacokinetics of intravenous chloramphenicol sodium succinate in adult patients with normal renal and hepatic function. *Journal of pharmacokinetics and biopharmaceutics* **1982,** *10* (6), 601-614.

39. Derendorf, H.; Möllmann, H.; Rohdewald, P.; Rehder, J.; Schmidt, E. W., Kinetics of methylprednisolone and its hemisuccinate ester. *Clinical Pharmacology & Therapeutics* **1985,** *37* (5), 502-507.

40. Jc, M.; Cyr, S., Comparative studies on absorption and metabolic disposal of water-soluble corticosteroid esters. *Metabolism: Clinical and Experimental* **1961,** *10*, 75-82.

41. Erion, M. D.; Bullough, D. A.; Lin, C.-C.; Hong, Z., HepDirect prodrugs for targeting nucleotide-based antiviral drugs to the liver. *Current opinion in investigational drugs (London, England: 2000)* **2006,** *7* (2), 109-117.

42. Rooseboom, M.; Commandeur, J. N. M.; Vermeulen, N. P. E., Enzyme-catalyzed activation of anticancer prodrugs. *Pharmacological reviews* **2004,** *56* (1), 53-102.

43. Xu, G.; Zhang, W.; Ma, M. K.; McLeod, H. L., Human carboxylesterase 2 is commonly expressed in tumor tissue and is correlated with activation of irinotecan. *Clinical Cancer Research* **2002,** *8* (8), 2605-2611.

44. Schacter, L. In *Etoposide phosphate: what, why, where, and how?*, 1996; pp 1-7.

45. McCombs, J. R.; Owen, S. C., Antibody drug conjugates: design and selection of linker, payload and conjugation chemistry. *The AAPS journal* **2015,** *17* (2), 339-351.

46. Jain, N.; Smith, S. W.; Ghone, S.; Tomczuk, B., Current ADC linker chemistry. *Pharmaceutical research* **2015,** *32* (11), 3526-3540.

47. He, C.; Liu, D.; Lin, W., Self-assembled core–shell nanoparticles for combined chemotherapy and photodynamic therapy of resistant head and neck cancers. *ACS nano* **2015,** *9* (1), 991-1003.

48. He, C.; Duan, X.; Guo, N.; Chan, C.; Poon, C.; Weichselbaum, R. R.; Lin, W., Core-shell nanoscale coordination polymers combine chemotherapy and photodynamic therapy to potentiate checkpoint blockade cancer immunotherapy. *Nature communications* **2016,** *7* (1), 1-12.

49. Poon, C.; He, C.; Liu, D.; Lu, K.; Lin, W., Self-assembled nanoscale coordination polymers carrying oxaliplatin and gemcitabine for synergistic combination therapy of pancreatic cancer. *Journal of Controlled Release* **2015,** *201*, 90-99.

50. He, C.; Liu, D.; Lin, W., Self-assembled nanoscale coordination polymers carrying siRNAs and cisplatin for effective treatment of resistant ovarian cancer. *Biomaterials* **2015,** *36*, 124-133.

51. Huxford, R. C.; deKrafft, K. E.; Boyle, W. S.; Liu, D.; Lin, W., Lipid-coated nanoscale coordination polymers for targeted delivery of antifolates to cancer cells. *Chemical science* **2012,** *3* (1), 198-204.

52. He, C.; Poon, C.; Chan, C.; Yamada, S. D.; Lin, W., Nanoscale coordination polymers codeliver chemotherapeutics and siRNAs to eradicate tumors of cisplatin-resistant ovarian cancer. *Journal of the American Chemical Society* **2016,** *138* (18), 6010-6019.

53. Liu, D.; He, C.; Poon, C.; Lin, W., Theranostic nanoscale coordination polymers for magnetic resonance imaging and bisphosphonate delivery. *Journal of Materials Chemistry B* **2014,** *2* (46), 8249-8255.

54. Duan, X.; Chan, C.; Han, W.; Guo, N.; Weichselbaum, R. R.; Lin, W., Immunostimulatory nanomedicines synergize with checkpoint blockade immunotherapy to eradicate colorectal tumors. *Nature communications* **2019,** *10* (1), 1899.

55. Poon, C.; Duan, X.; Chan, C.; Han, W.; Lin, W., Nanoscale coordination polymers codeliver carboplatin and gemcitabine for highly effective treatment of platinum-resistant ovarian cancer. *Molecular pharmaceutics* **2016,** *13* (11), 3665-3675.

Chapter 2. Nanoscale Coordination Polymer Co-delivers Oxaliplatin and Dihydroarteminisin for Chemoimmunotherapy of Colorectal Cancer

2.1 Introduction

Colorectal cancer (CRC) is the second leading cause of cancer-related deaths in the United States, accounting for approximately 9% of cancer-related deaths.[1] Although localized CRC has a 5-year survival rate of ~89%, more than half of CRC patients have distant or regional metastasis at the time of diagnosis. Those with metastases to other organs have a 5-year survival rate of only ~12%. There is an urgent need for novel therapeutics to effectively treat metastatic CRC.

Conventional treatments of localized CRC include surgery and adjuvant chemotherapies, but side effects and drug resistance can limit the effectiveness of treatment.[2-5] In recent years, immunotherapy has been a promising approach to treat some subsets of CRC,[6-9] particularly after the Food and Drug Administration (FDA) approval of the antibodies against programmed cell death protein 1 (PD-1), pembrolizumab[10, 11] and nivolumab[12, 13] in 2014. However, only a small percentage of CRC patients benefit from checkpoint blockade therapy, including about 15% of all patients and less than 5% advanced stage patients who have tumors with overexpression of PD-1 and inherently high $CD8^+$ T cell infiltration.[14] Methods to improve tumor immunogenicity or $CD8^+$ T cell infiltration may improve the response rate among CRC patients.

Oxaliplatin (OxPt) is one of the key components used in the standard chemotherapy of CRC.[15-17] Although most anticancer drugs are not considered to be immunogenic, evidence has shown that oxaliplatin is one of a small number of anticancer drugs that can induce immunogenic cell death (ICD).[18-20] Another known inducer of ICD is reactive oxygen

species (ROSs) generated by photodynamic therapy (PDT),[18, 21, 22] which requires light irradiation and is thus limited by light penetration in human tissue.[23] An alternative way of generating ROS and induce ICD is using chemically unstable peroxide compounds that can be triggered to release ROS. Dihydroartemisinin (DHA), the active metabolite of the antimalarial drug artemisinin, is an effective ROS producer due to the peroxide bridge within the molecule.[24] Upon reacting with ferrous iron, DHA decomposes to generate ROS and other free radicals.[25, 26] Moreover, iron metabolism in malignant cells is altered so that the labile iron pool is increased, allowing for the enhanced therapeutic effect of DHA in tumor.[27-29] Despite the great potential of DNA in inducing ICD, a significant drawback is the instability of DHA in water, which can lead to low bioavailability when dosed to patients.[30, 31]

As NCPs offer a unique platform for co-delivering both hydrophobic and hydrophilic drugs, water-soluble oxaliplatin and hydrophobic DHA can be loaded into an NCP after modifications using the prodrug approach to form OxPt/DHA nanoparticles. Phosphates were installed on oxaliplatin to form a zinc-crosslinked core and DHA was conjugated to cholesterol so that it can be protected from water in the hydrophobic part of the lipid bilayer. Systemic dosing of the OxPt/DHA particle showed accumulation in tumor and elicited strong antitumor immunity. Combination of OxPt/DHA and α-PD-L1 antibody not only eradicated CRC tumors in mouse models but also prevented the formation of the same type of tumor after via a long-term tumor-specific immune memory response.

2.2 Results and discussion

2.2.1 Preparation of particles

Both OxPt and DHA were converted into their respective prodrug forms as shown in **Figure 2-1**. Two phosphate groups were linked with OxPt via the carbamate linkage, allowing for coordination with Zn^{2+}. A cholesterol molecule was installed on the hydroxyl group of DHA using disulfide linkage to form a chol-DHA prodrug. We hypothesized that this linkage could be cleaved by free thiols inside cells to release DHA.

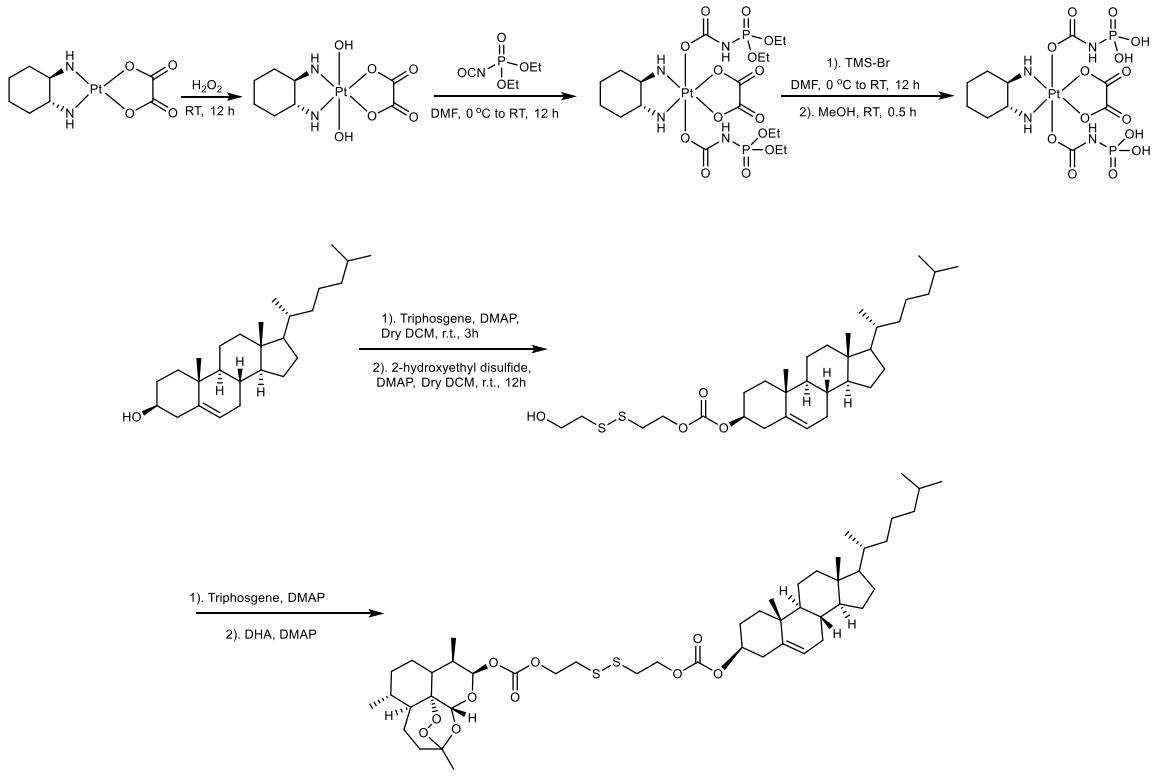

Figure 2-1. Synthesis of OxPt prodrug and DHA prodrug.

OxPt/DHA particles were synthesized in a two-stage process (**Figure 2-2** a). The particle core containing the OxPt prodrug was first synthesized in an organic solvent. Microemulsions of $Zn(NO_3)_2$ and OxPt prodrug was mixed in organic solvents with

surfactants under vigorous stirring, monosodium salt of 1,2-dioleoyl-sn-glycero-3-phosphate (DOPA) was used to stop the reaction by capping on the surface of freshly formed Zn-phosphate coordination polymer. By controlling the time and amount of DOPA, a spherical, monodispersed solid particle core was formed with a Z-average diameter of 78.3 ± 0.2 nm and polydispersity index (PDI) of 0.16 ± 0.01 by dynamic light scattering (DLS) (**Figure 2-2** b and c).

The solid particle core containing OxPt was subsequently coated with a mixture of 1,2-dioleyl-sn-glycero-3-phosphocholine (DOPC), cholesterol, 1,2-diastearoyl-sn-glycero-3-phosphoethanolamine-N-[amino(polyethylene glycol)2000] (DSPE-PEG2k), and chol-DHA in 3:1.5:1.5:1 molar ratio in 30% ethanol. After evaporation of all organic solvents, the spherical OxPt/DHA particles formed in aqueous environment with an OxPt:DHA molar ratio of 1:0.5. The particle showed a Z-average diameter of 103.4 ± 1.1 nm, a low PDI of 0.12 ± 0.01, and a negative surface charge of -20.8 ± 1.25 mV in water (**Figure 2-2** d and e). Dextrose was further dissolved in the particle solution to make a 5% dextrose solution for biological studies. The coated particles were small enough to penetrate into tumor by leveraging the EPR effect, while large enough to avoid renal filtration. PEG coating ensured the formation of a hydrated layer to prevent protein binding and recognition, minimizing the mononuclear phagocyte system (MPS) uptake after systemic injection.[32-35] OxPt/DHA showed no significant change in size and PDI when stored at 4^{o}C for a year or incubated at 37^{o}C with 5mg/mL bovine serum albumin (BSA) for 24h, indicating that the particle is stable in both long-term storage and blood circulation (**Figure 2-3**).

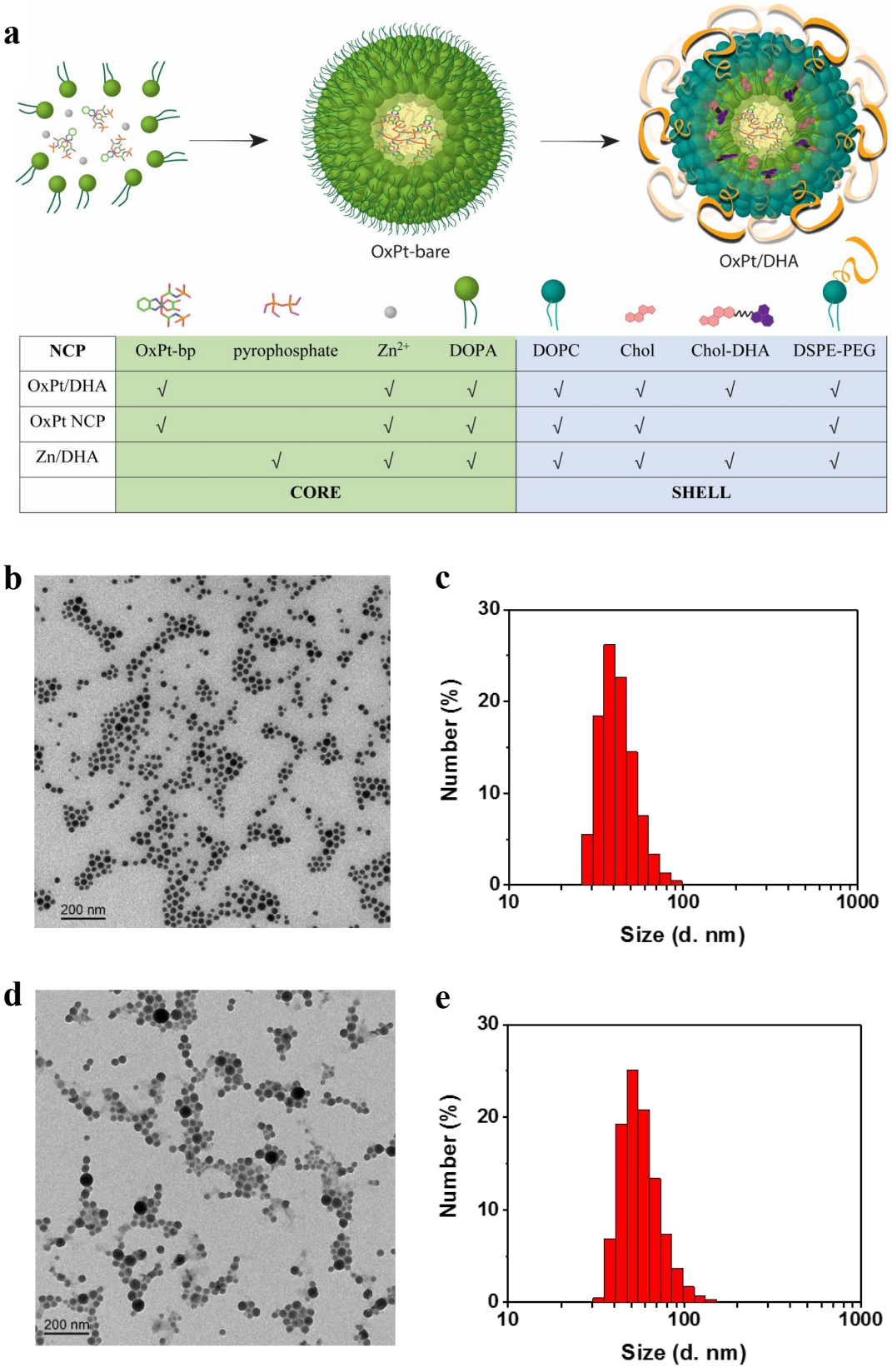

NCP	OxPt-bp	pyrophosphate	Zn^{2+}	DOPA	DOPC	Chol	Chol-DHA	DSPE-PEG
OxPt/DHA	√		√	√	√	√	√	√
OxPt NCP	√		√	√	√	√		√
Zn/DHA		√	√	√	√	√	√	√
	CORE				**SHELL**			

Figure 2-2. Schematic illustration and characterization of OxPt/DHA.

Figure 2-2 (continued). (a) Schematic illustration showing layer-by-layer construction of the hybrid core-shell structure of OxPt/DHA. The OxPt/DHA consists of an OxPt prodrug coordinated to Zn^{2+} ions in the core and chol-DHA in the lipid shell. Compositions of the three NCPs investigated are also shown. (b) TEM image of OxPt particle core. (c) Number-average diameter of OxPt particle core characterized by DLS. (d) TEM image of OxPt/DHA. (e) Number-average diameter of OxPt/DHA characterized by DLS.

Several control particles were also synthesized. Particles used in OxPt monotherapy control was prepared using the same process in the absence of chol-DHA. ZnP particle core without OxPt was prepared by replacing OxPt prodrug with equal molar of sodium pyrophosphate and further coated with lipid and chol-DHA as DHA monotherapy control (**Table 2-1**). Fluorescently labeled particle core was prepared by dissolving xylenol orange in a microemulsion of $Zn(NO_3)_2$. The shell-labeled particle was prepared by loading FITC-DSPE and pyropheophytin a-labeled cholesterol when doing the coating step.

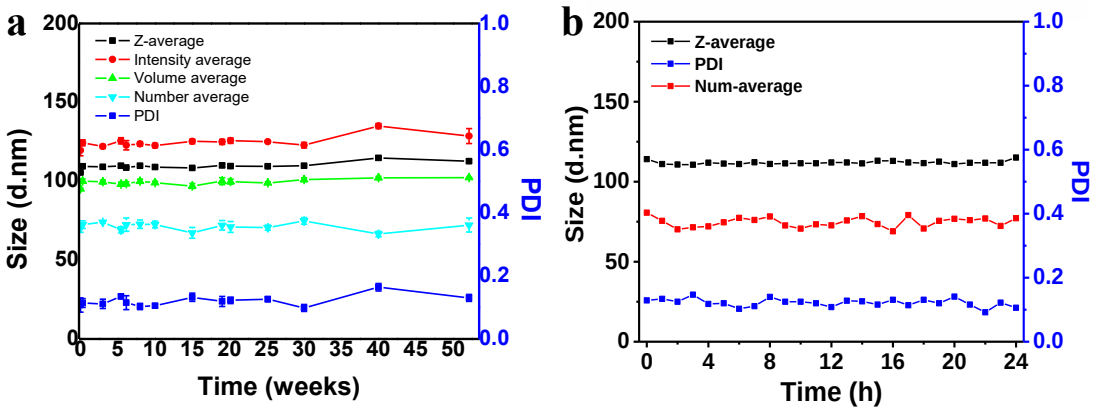

Figure 2-3. Stability test of OxPt/DHA at (a) 4 °C or (b) 37 °C with 5 mg/mL BSA.

Table 2-1. Characterization of nanoparticles

	Z-Average (d. nm)	PDI	Number Average (d. nm)	ζ-potential (mV)
OxPt-bare	78.27 ± 0.18	0.159 ± 0.01	40.40 ± 3.08	
OxPt NCP	89.21 ± 1.17	0.136 ± 0.01	55.37 ± 2.28	-17.90 ± 0.46
OxPt/DHA	73.80 ± 0.36	0.174 ± 0.01	41.00 ± 0.62	-20.83 ± 1.25
Zn/DHA	98.60 ± 0.75	0.140 ± 0.01	63.50 ± 6.76	-23.85 ± 3.75

2.2.2 In Vitro Drug Release

Although originally proposed to have a reductive release mechanism of both drugs like other prodrugs with reducible linkages,[36-40] the actual releasing mechanisms of OxPt/DHA nanoparticles were proved to be more complicated.

While Chol-DHA was originally designed based on the GSH reduction mechanism, there exists a faster pathway by hydrolysis of a carbonate group in the linker. In aprotic solvents, the chol-DHA conjugate is stable at physiological 37 ^{o}C for at least 24 h. Introduction of a protic solvent rapidly decomposes chol-DHA. Specifically, chol-DHA showed 100% retention in THF compared to 20% in methanol after incubation for 5 h at 37^{o}C. The release process further accelerated in the presence of acids, with nearly 100% degradation of chol-DHA when 1 mM HCl was added to methanol (**Figure 2-4** a). Importantly, the decomposition product of chol-DHA had a methyl group capped on the hydroxyl group of DHA (**Figure 2-5** a), indicating the solvent might be involved in the decomposition process. However, incorporation of chol-DHA into the lipid bilayer shell of OxPt/DHA can shield

the prodrug from premature drug release by limiting exposure to the aqueous solvent. No significant loss of chol-DHA content in OxPt/DHA was observed at 37 ^{o}C for 24 h, whereas disruption of the lipid bilayer by Triton X-100 led to 90% degradation of chol-DHA within 5 h.

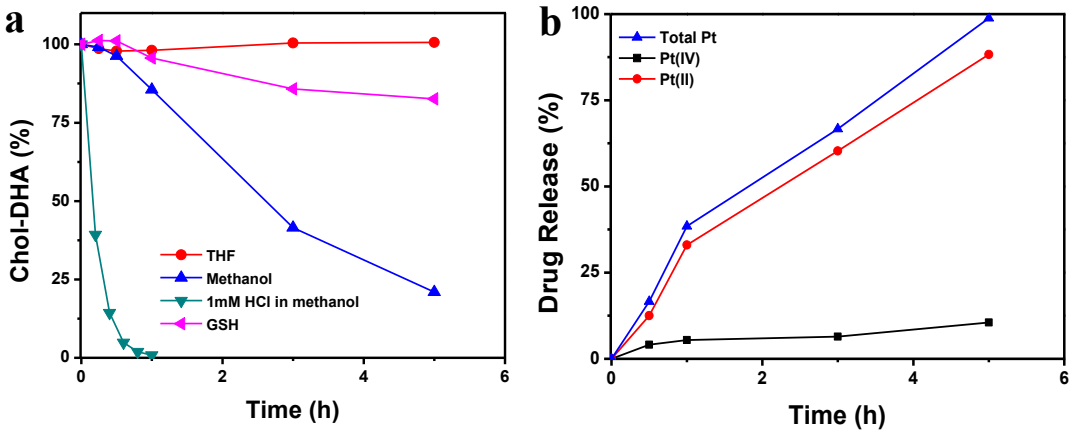

Figure 2-4. Release kinetics of two drugs. (a) Decomposition of chol-DHA in different conditions. (b) Release and reduction of OxPt prodrug.

Taken together, we propose a proton-catalyzed solvolysis mechanism for DHA release from its prodrug, chol-DHA. A proton binds with a chol-DHA molecule and leads to a reversible C-O bond breaking to form a DHA cation stabilized by the nearby oxygen and a carbonate monoester. The carbonate monoester is unstable and readily undergoes an irreversible reaction to release CO_2 hence drive the reaction forward. The DHA cation reacts with a molecule of solvent to form DHA or analogous compounds. To further confirm this mechanism, we synthesized a cholesterol-DHA conjugate with a carboxylate ester in the place of the carbonate ester.

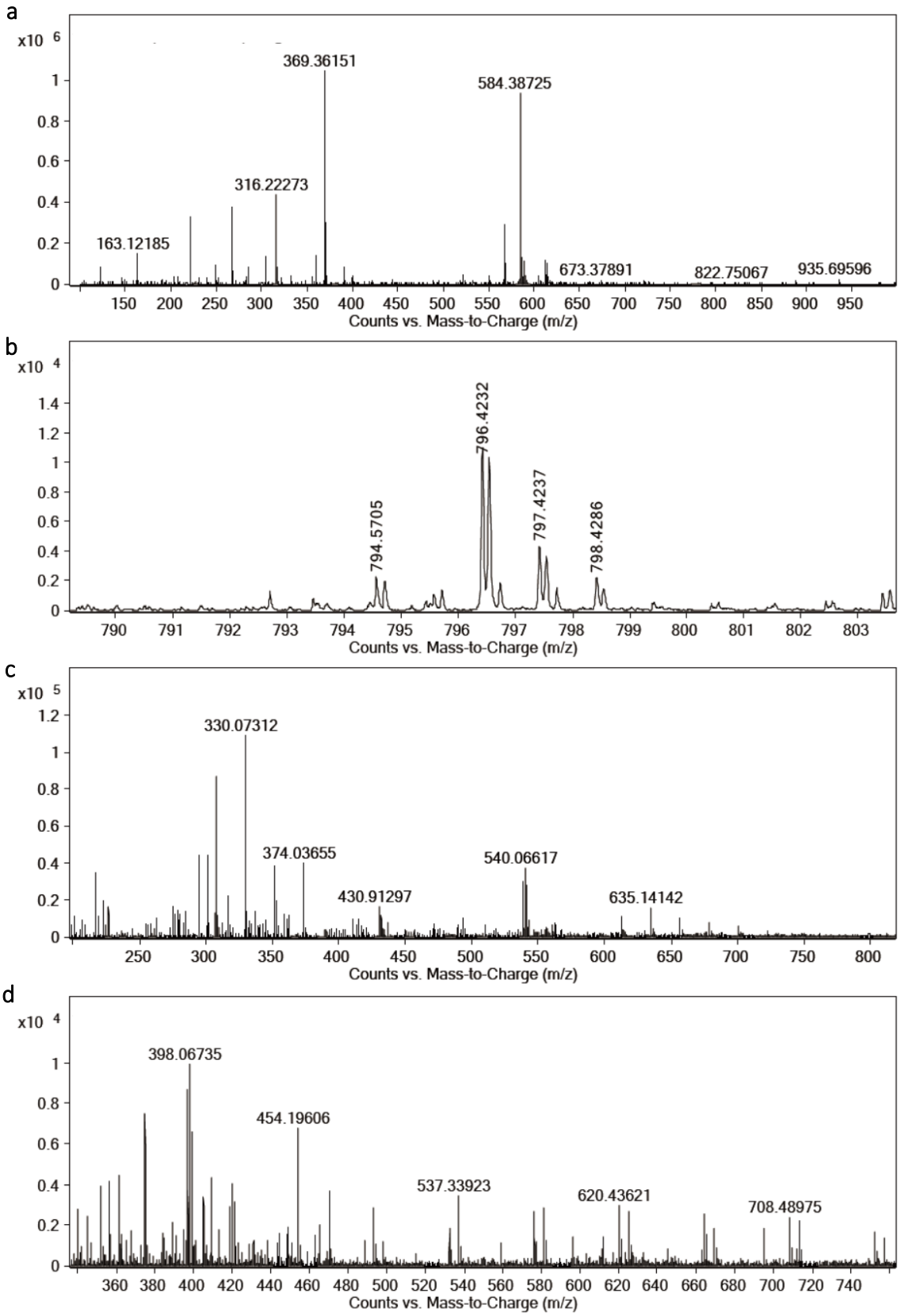

Figure 2-5. HR-MS showing the release mechanisms of drug release.

Figure 2-5 (continued)**.** HR-MS showing the release mechanisms of DHA and OxPt. (a) Chol-DHA decomposition product in methanol. 584.38725: Chol-S-S-OH; 369.36151: Chol-S-S-OH fragment; 316.22723: artemether. (b) Chol-DHA disulfide exchange product with GSH. 796.4232: Chol-S-GSH. (c) Hydrolysis product released from particle core (540.06617). (d) Reduction product (free oxaliplatin) of particle core by ascorbate (398.06735).

Carboxylate esters cannot release CO_2, eliminating the irreversible driving force. As expected, the carboxylate ester version of DHA-cholesterol conjugate chol-AS no longer showed DHA release in protic solvents.

The triggered release of OxPt from OxPt/DHA was rigorously investigated. Upon entering cells, the Pt^{IV} prodrug of OxPt could be efficiently released from the core. The released Pt^{IV} compound is stable in the presence of GSH, which deactivates the parent OxPt by coordination with Pt, but can be efficiently reduced by ascorbate which exists abundantly in plasma and can easily penetrate into cancer cells[41, 42] to generate OxPt. OxPt prodrug can also be converted into free OxPt through a single-step reduction of ascorbate (but not GSH). In the presence of ascorbate, the release of free oxaliplatin was observed and the rate of release is faster than hydrolysis, indicating contributions of both mechanisms (**Figure 2-4** b). Unlike OxPt, the released Pt^{IV} compound is not deactivated by GSH and thiol-containing proteins that are abundantly present inside cells. The released Pt^{IV} compound can thus serve as a reservoir for OxPt to increase the ability to form Pt-DNA adducts in cell nuclei to exert cytotoxic effects (**Figure 2-5** c and d).

These data support the stability of our lipid bilayer to prevent the penetration of solvents or reducing molecules to preserve the integrity of our chol-DHA and OxPt prodrugs in

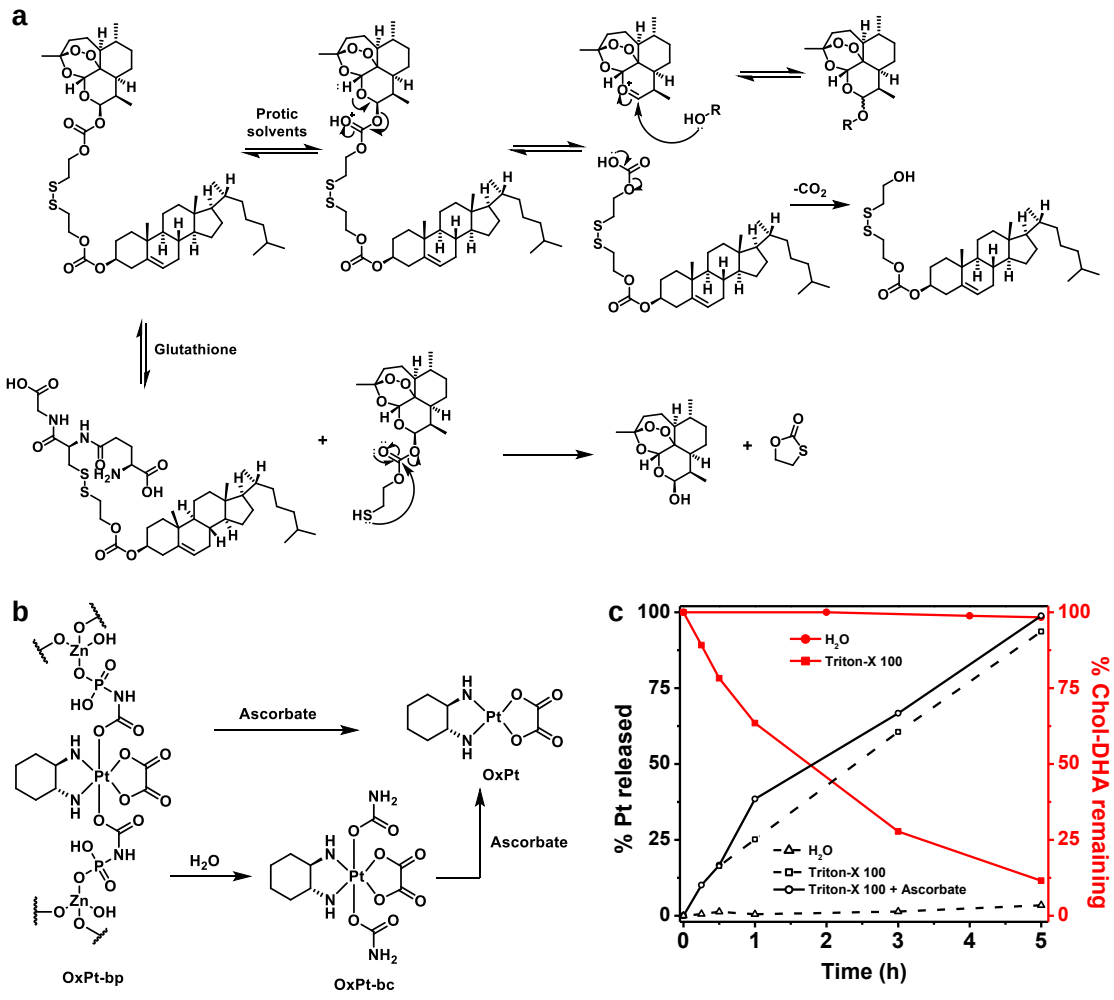

Figure 2-6. Release of DHA and OxPt from OxPt/DHA. **(**a) Proposed two-pathway mechanism of DHA release. (b) Proposed two-pathway mechanism of OxPt release. (c) Total Pt release from and chol-DHA remaining in OxPt/DHA particle when incubated in water at 37 °C with or without 0.5% Triton X-100 and 5 mM ascorbate.

circulation. Upon disruption of the lipid bilayer during and after endocytosis, both prodrugs are exposed to reducing agents and a lower pH in late endosomes/lysosomes. DHA can be released intracellularly with an intact endoperoxide moiety via both GSH reduction and hydrolysis. Then, the core of OxPt/DHA continuously releases a Pt^{IV} OxPt prodrug resistant to GSH coordination, allowing for prolonged drug exposure when reduced to parent OxPt by ascorbate (**Figure 2-6**).

2.2.3 Cellular uptake of NCP particles

To study the internalization and dissociation of NCP particles into cells, we used particles with core, lipid, and cholesterol cargo labeled with xylenol orange (blue), FITC (green), and pyropheophytin a (red). In the first 10 min, white (green, blue, and red merged) surrounding the cell indicated that the particles were already bound to the cell surface. Over time, FITC labeled phospholipids mainly stayed on the cell surface while particle core (blue) and organic cargo on cholesterol (red) gradually showed up inside the cell as magenta (blue and red merged). This observation indicates that the cellular uptake of NCP particle may start with lipid bilayer fusion of NCP and endosome membranes, disrupting the well-protected particle surface and triggering the disassembly of particle and release of cargos, while the phospholipid components of the particle trafficked back to the cell membrane together with recycled endosomes.

More quantitative studies were performed to determine the kinetics of uptake. Flow cytometry results showed an increased percentage of fluorescently labeled cells 1 h after incubation and the uptake continued over time to achieve a much higher cellular concentration at 24 h. Inductively coupled plasma-mass spectrometry (ICP-MS)

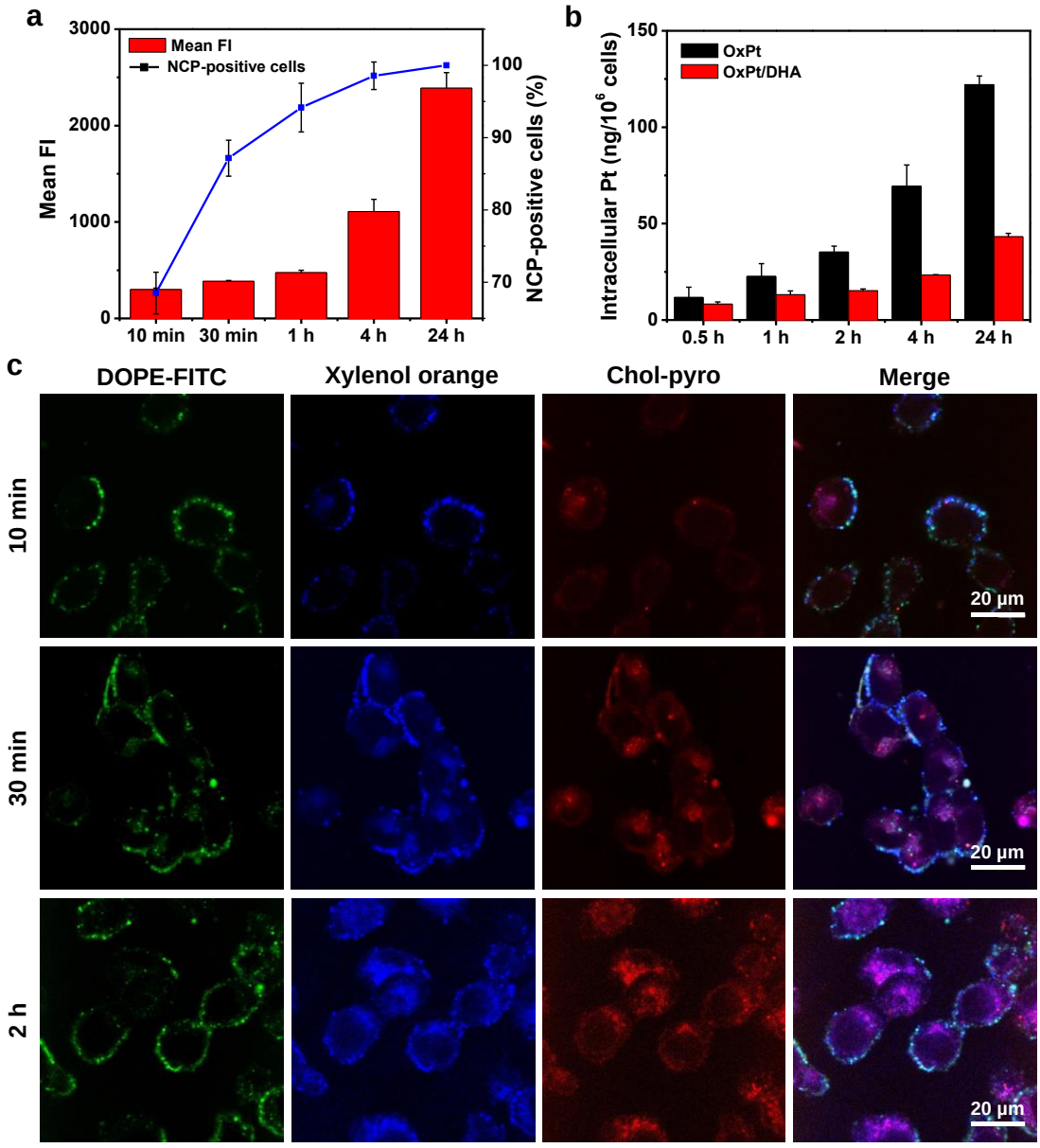

Figure 2-7. (a) Internalization of organic components of OxPt/DHA as labeled by chol-pyro (n = 3). (b) Internalization of Pt determined by ICP-MS (n = 3). (c) Internalization and dissociation of NCP components imaged by confocal laser scanning microscopy (CLSM) using fluorescently labeled particles.

quantification of intracellular Pt also showed time-dependent uptake of both nanoparticles and free OxPt. Possibly due to the surface PEG coating reducing particle-cell interaction, the rate of NCP uptake was slower than that of free drug (**Figure 2-7**).

2.2.4 Cytotoxicity and in vivo efficacy on mouse models

We studied the *in vitro* cytotoxicity of both free drugs and their combination on two murine colorectal cancer cell lines, CT26 and MC38. The two free drugs showed a synergistic effect, the IC_{50} of OxPt on both cell lines decreased by approximately 3 times when combined with 0.5 molar equivalent of DHA (from 10.30 ± 1.62 to 3.62 ± 0.87 μM and 12.8 ± 1.32 to 3.97 ± 0.67 μM on CT26 and MC38 cells, respectively). While in the form of NCP, the IC_{50} value of both drugs did not significantly change, indicating both drugs can be readily released from the particle. The synergy between both drugs on the particle form was still observed as the Pt IC_{50} decreased from 12.98 ± 1.54 to 9.44 ± 1.85 μM and 15.77 ± 1.12 to 8.14 ± 0.39 μM on CT26 and MC38 cells, respectively (**Table 2-2**).

Table 2-2. IC_{50} values of OxPt, DHA and their combination in free drug form and particle form on CT26 and MC38 cell lines

	OxPt	DHA	OxPt + DHA	OxPt NCP	Zn/DHA	OxPt/DHA
CT26	10.3 ± 1.62	7.13 ± 1.74	3.62 ± 0.87 (1.81 ± 0.44)[a]	12.98 ± 1.54	11.37 ± 1.65	9.44 ± 1.85 (4.77 ± 0.93)[a]
MC38	12.8 ± 1.32	6.89 ± 1.31	3.97 ± 0.67 (1.99 ± 0.34)[a]	15.77 ± 1.12	8.89 ± 0.21	8.14 ± 0.39 (4.07 ± 0.20)[a]

[a]The numbers in parentheses refer to DHA IC_{50} values.

The efficacy of particle alone or in combination with immuno checkpoint blockade therapy was evaluated on CT26 and MC38 tumor bearing mouse models. CT26 and MC38 tumors were inoculated subcutaneously on immunocompetent BALB/c and C57BL/6 mice, respectively, and tumors were allowed to reach 80-100 mm^3 approximately 12 days after inoculation to obtain relatively immunosuppressive models.

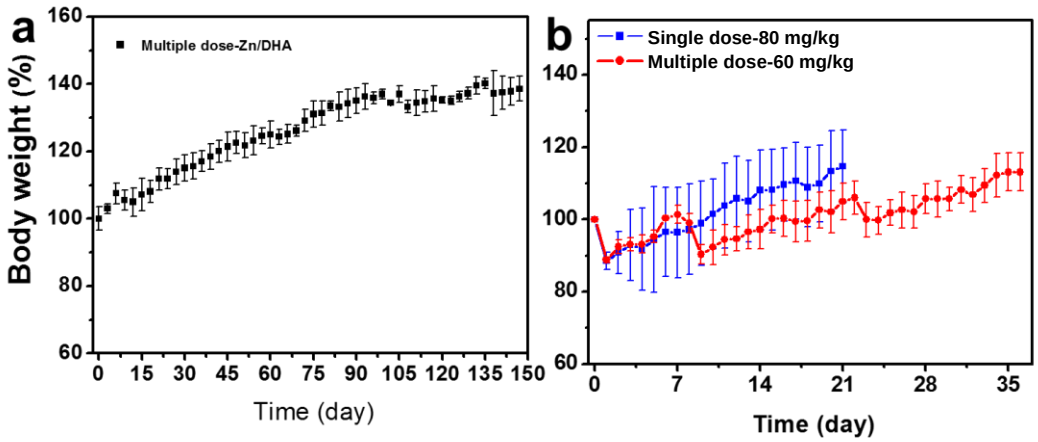

Figure 2-8. Limited toxicity by chemotherapeutic NCPs. (a) Body weight evolution of BALB/c mice after dosing 5 mg DHA/kg once every three days for a total of fifty doses. (b) Body weight evolution of C57BL/6 mice after a single injection of 80 mg OxPt/kg and multiple injections of 60 mg OxPt/kg once every week for a total of four doses of OxPt/DHA. Data are expressed as means ± SD (n = 3).

Then mice were intraperitoneally (i.p.) injected once every three days at equivalent doses of 8 mg OxPt/kg, 2.8 mg DHA/kg, and/or 75 μg anti-PD-L1/mouse, as necessary, for up to 12 total doses The dose is 10 times lower than the MTD allows for long-term metronomic dosing.[43] As there is still significant tumor accumulation 72 h post-administration, this

dosing schedule allows for a dose-dense chemotherapy schedule with a near-continuous amount of chemotherapy in the tumor (**Figure 2-8**).

In CT26 model, anti-PD-L1 showed no significant efficacy, indicating that the tumor model was immunosuppressive. The combination of two free drugs and anti-PD-L1 was only moderately effective (203.27 ± 81.00 mm^3 on day 18 compared to 616.80 ± 46.59 mm^3 for PBS) but very toxic. The relative body weight dropped after the treatment and all mice had to be euthanized for humanitarian reasons after only 3 doses. NCP with OxPt only significantly delayed tumor growth for more than one month from day 22 to day 57. Combining with anti-PD-L1 improved antitumor efficacy at the beginning of the treatment but eventually resulted in a similar tumor growth rate comparing to OxPt NCP alone. Interestingly, although Zn/DHA did not substantially change the efficacy of anti-PD-L1 and only moderately delayed the tumor growth for about 12 days comparing with OxPt NCP, the combination of OxPt/DHA and anti-PD-L1 showed significant efficacy which completely eradicated the tumor around days 40-50 (**Figure 2-9**). Moreover, after confirming the tumor eradication by observing until 3 months after the tumor disappeared, CT26 cells were inoculated again on those mice to perform a rechallenge experiment and no tumor formed on those mice. While rechallenging with 4T1 cells resulted in tumor formation and growth. This result showed that OxPt/DHA plus anti-PD-L1 generated long-lasting antitumor immunity and it was specific to CT26 tumors. Antitumor efficacy experiments on MC38 model showed similar results. The low dose, low toxicity and high efficacy provide OxPt/DHA and anti-PD-L1 a wide therapeutic window, making it optimal for further clinical development.

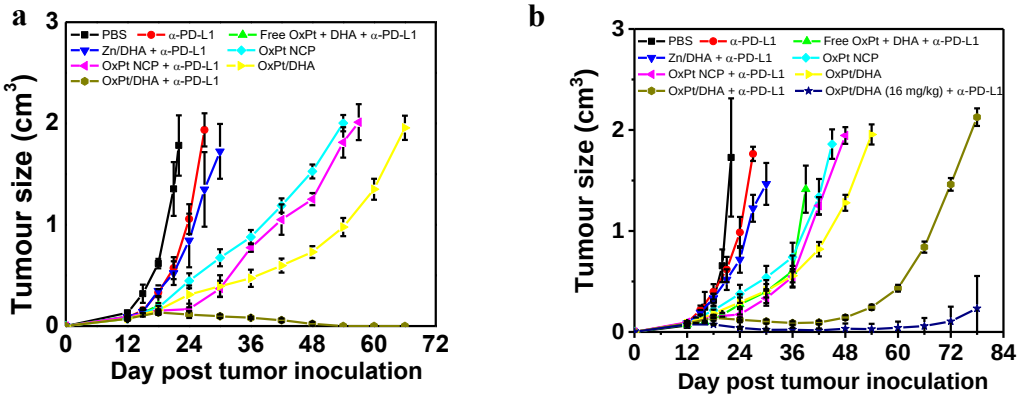

Figure 2-9. CT26 (a) and MC38 (b) tumor growth curve after treated with various formulations

2.2.5 Pharmacokinetics and biodistribution

As NCP was designed to be long-circulating due to its surface property and tumor targeting due to the EPR effect, the pharmacokinetics and biodistribution were studied. OxPt/DHA showed a long Pt circulation half-life of 20.70 ± 4.50 h in rats, while the DHA part (in the form of chol-DHA) showed a 7.01 ± 1.13 h half-life. The shorter half-life can be explained by the intrinsic instability of DHA and some loss during circulation because chol-DHA locates closer to the surface of the particle. Long circulation resulted in significantly improved drug exposure as the AUC of Pt increased 14 folds and that of DHA increased about 100 folds, which made it possible for the two drugs available in plasma at a relatively high concentration simultaneously and achieve a synergistic effect (**Table 2-3** and **Figure 2-10**).

Table 2-3. Pharmacokinetic information of OxPt and DHA

Parameter	$t_{1/2}$ alpha	$t_{1/2}$ beta	AUC $_{0\text{-inf}}$	AUMC	MRT
Unit	h	h	ID%/mL*h	ID%/mL*h^2	h
Free OxPt	0.18 ± 0.02	14.67 ± 3.04	5.77 ± 2.65	122.5 ± 77.5	20.1 ± 4.4
Free DHA[a]	(0.22 ± 0.04) [b]		(0.03 ± 0.01) [b]	(0.59 ± 0.16) [b]	(0.31 ± 0.06) [b]
OxPt/DHA	0.27 ± 0.30 (0.39 ± 0.38) [b]	20.70 ± 4.50 (7.01 ± 1.13) [b]	80.9 ± 11.2 (33.6 ± 5.8) [b]	2431.5 ± 809.7 (330.2 ± 79.8) [b]	29.51 ± 6.27 (9.79 ± 1.41) [b]

[a]This was fitted to a one-compartment model.

[b]The numbers in parentheses refer to DHA values.

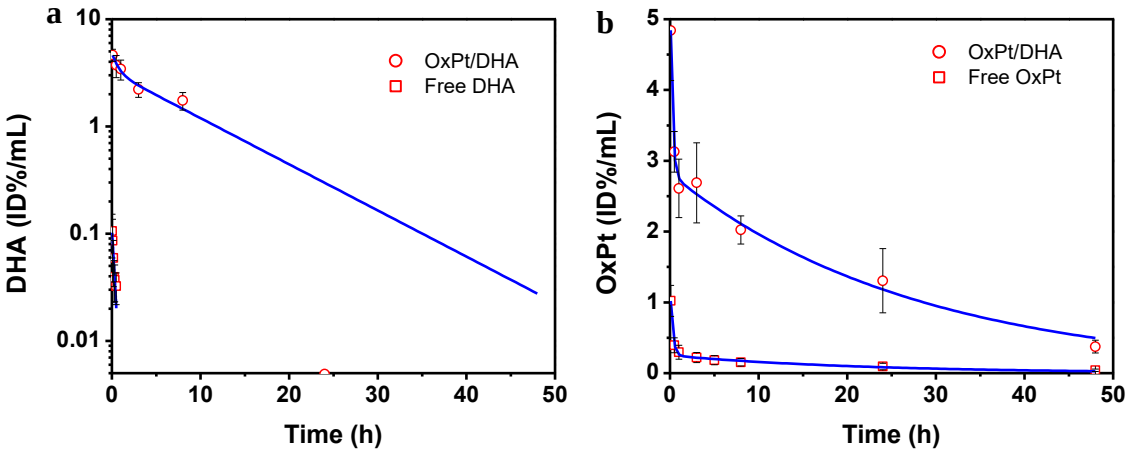

Figure 2-10. Time-dependent DHA (a) and OxPt (b) concentrations in the bloodstream from 0-48 h after i.v. injection of DHA, OxPt, or OxPt/DHA to SD/CD rats.

The biodistribution profile of OxPt/DHA NCP in CT26 tumor-bearing mice showed <5 %ID Pt/g accumulation in major organs like liver, spleen, and kidney, indicating the MPS uptake of OxPt/DHA was insignificantly and may explain the reason for low systemic toxicity compared with the free drug combination. Furthermore, the low accumulation (<3% ID Pt/g) of Pt suggested OxPt/DHA does not aggregate in circulation. As a result of high drug exposure, low MPS uptake, and EPR effect, the accumulation in tumor reached a maximum of 12.3 ± 2.8 %ID/g at 48 h post administration, which is 21 times higher than free OxPt (0.56 ± 2.8 %ID/g) (**Figure 2-11**).

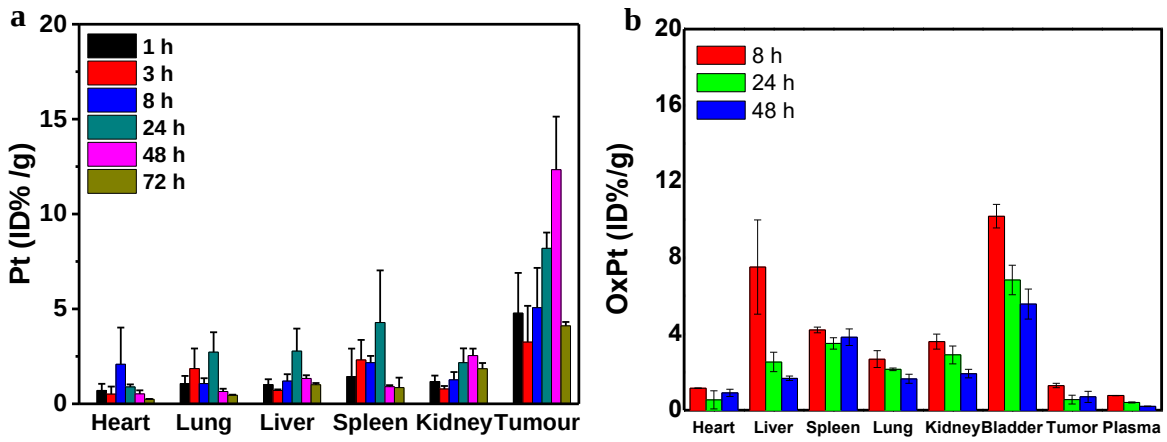

Figure 2-11. Time-dependent Pt biodistribution of OxPt/DHA (a) and free OxPt (b) after i.p. injected to CT26-bearing mice.

2.3 Conclusion

This study presents a new approach to initiate and stimulate immune-mediated eradication of syngeneic tumors by delivering two immunogenic anticancer drugs using the NCP platform. By encapsulation of prodrugs inside the particle, OxPt/DHA can efficiently prevent decomposition and degradation. OxPt/DHA not only acted as a simple combination of two cytotoxic drugs but also converted poorly immunogenic tumors into an *in situ* vaccine and significantly potentiated checkpoint blockade immunotherapy. When further combined with anti-PD-L1, OxPt/DHA was able to irradicate tumors in animal models and immunize cured mice against challenged live tumor cells by generating long-term antitumor immunity.

2.4 Experimental

2.4.1 Synthesis of prodrugs

Synthesis of OxPt prodrug

3.0 g oxaliplatin and 30 mL deionized water were charged to a 50 mL round bottom flask with a stir bar. The mixture was stirred and cooled over an ice bath to 0 ^{o}C. 5.45 mL 30% hydrogen peroxide was slowly added to the mixture in 15 minutes. The reaction mixture was stirred in the dark overnight at room temperature. The mixture was carefully concentrated to approximately 5 mL on a rotary evaporator, then added 25 mL ethanol and cooled at -20 ^{o}C for 3 hours. The white solid was collected by vacuum filtration followed by washing with cold water (2 x 20 mL) and cold ethanol (2 x 20 mL) to give a quantitative

yield (3.25 g). ^{1}H-NMR (500MHz, D_2O): 1.16 (t, 2H), 1.47 (d, 2H), 1.53 (d, 2H), 2.17 (d, 2H), 2.74 (d, 2H).

3.0g OxPt-$(OH)_2$ was charged to an oven-dried 50 mL round bottom flask with a stir bar. 10 mL anhydrous DMF was added to the flask and the flask was purged with N_2 for 30 min. The mixture was cooled over an ice bath for 15 min and then diethoxyphosphinyl isocyanate (2.2 mL, 2.55 g, 2.05 eq.) was added dropwisely through a syringe. Then the mixture was slowly warmed up to room temperature and stirred in dark overnight. The resulting mixture was directly loaded on a silica column packed with hexanes and DMF was removed by flushing the column using a 1:1 DCM/hexanes mixture. Then the product was collected by flushing the column with 10% methanol in DCM. Yield: 4.56g, 83%. ^{1}H-NMR (500MHz, DMSO-d_6): 1.12 (t, 2H), 1.26 (t, 12H), 1.50 (d, 2H), 1.60 (d, 2H), 2.15 (d, 2H), 2.73 (m, 2H), 4.00 (m, 8H), 7.96 (s, 2H), 8.41 (d, 2H), 8.75 (d, 2H).

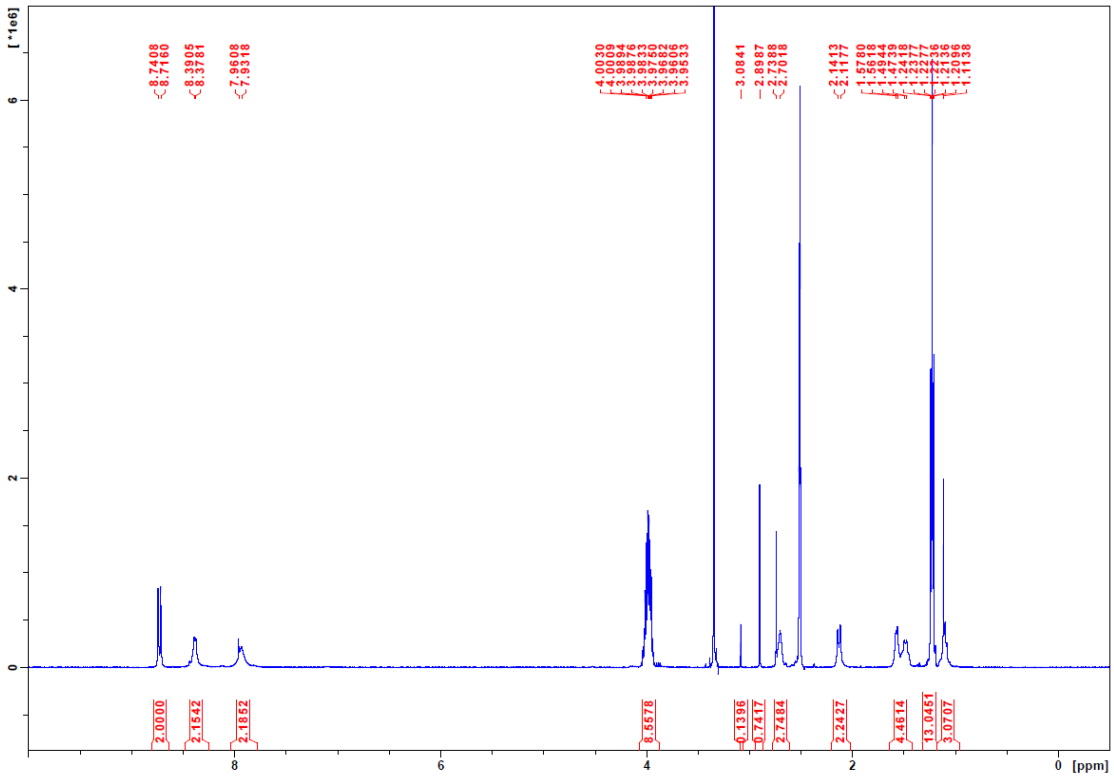

Figure 2-12. ^{1}H-NMR spectrum of Ox-ester.

1.0 g Ox-ester was charged to an oven dried 50mL round bottom flask with and stir bar. 20 mL anhydrous DCM was added and the flask was purged with N_2 for 30 min. The flask was cooled over an ice bath for 15 min. 2.5 mL bromotrimethylsilane in 5 mL DCM was added dropwisely through a syringe. The reaction mixture was slowly warmed up to room temperature and stirred at dark overnight. The solvent was then removed by rotary evaporation and further dried under high vacuum for 2 hours. Then 5 mL cold methanol was added to the flask and stirred for 30 minutes at room temperature. The product was crushed out by adding 30 mL DCM to the methanol solution and collected by centrifugation at 13000 rpm for 10 min. Yield: 0.59 g, 69%. ^{1}H-NMR (500MHz, D_2O): 1.19 (t, 2H), 1.51 (s, 4H), 2.19 (d, 2H), 2.90 (d, 2H).

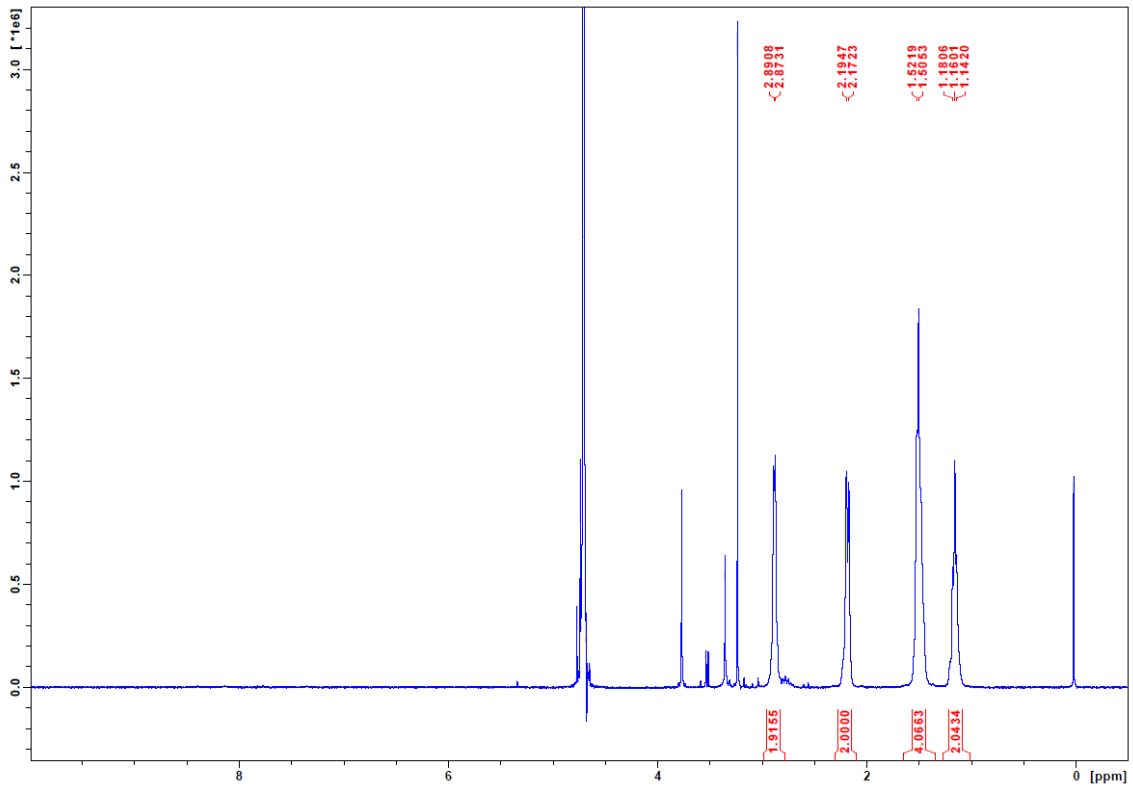

Figure 2-13. ^{1}H-NMR spectrum of OxPt prodrug.

Synthesis of chol-DHA.

To a mixture of Cholesterol (500 mg, 1.3 mmol) and 4-N,N-dimethylaminopyridine (DMAP, 0.32 g, 2.8 mmol) in anhydrous DCM, a solution of triphosgene (128 mg, 0.43 mmol) in anhydrous DCM (2 mL) was added dropwise over an ice bath with stirring. The resultant solution was warmed to room temperature and further stirred for 20 min and then added dropwise to a solution of bis(2- hydroxyethyl) disulfide (440 mg, 2.8 mmol) in anhydrous DCM (5 mL) over an ice bath. The reaction mixture was then warmed to room temperature and stirred for 12 h. After removal of solvent, the residue was purified to afford cholest-5-en-3-ol (3β)-, 3-(2-((2- hydroxyethyl)disulfanyl)ethyl) carbonate (Chol-S-S-OH) by column chromatography on silica gel with ethyl acetate/hexane (1:2, v/v). Yield: 0.44 g (60%). ^{1}H-NMR (500 MHz, $CDCl_3$): 0.65 (s, 3H), 0.83 (d, 3H), 0.84-1.15 (m, 13H), 1.22-1.66 (m, 13H), 1.75-2.02 (m, 5H), 2.37 (m, 2H), 2.85 (m, 3H), 2.92 (t, 2H), 3.83 (t, 2H), 4.34 (t, 2H), 4.44 (m, 1H), 5.37 (d, 1H).

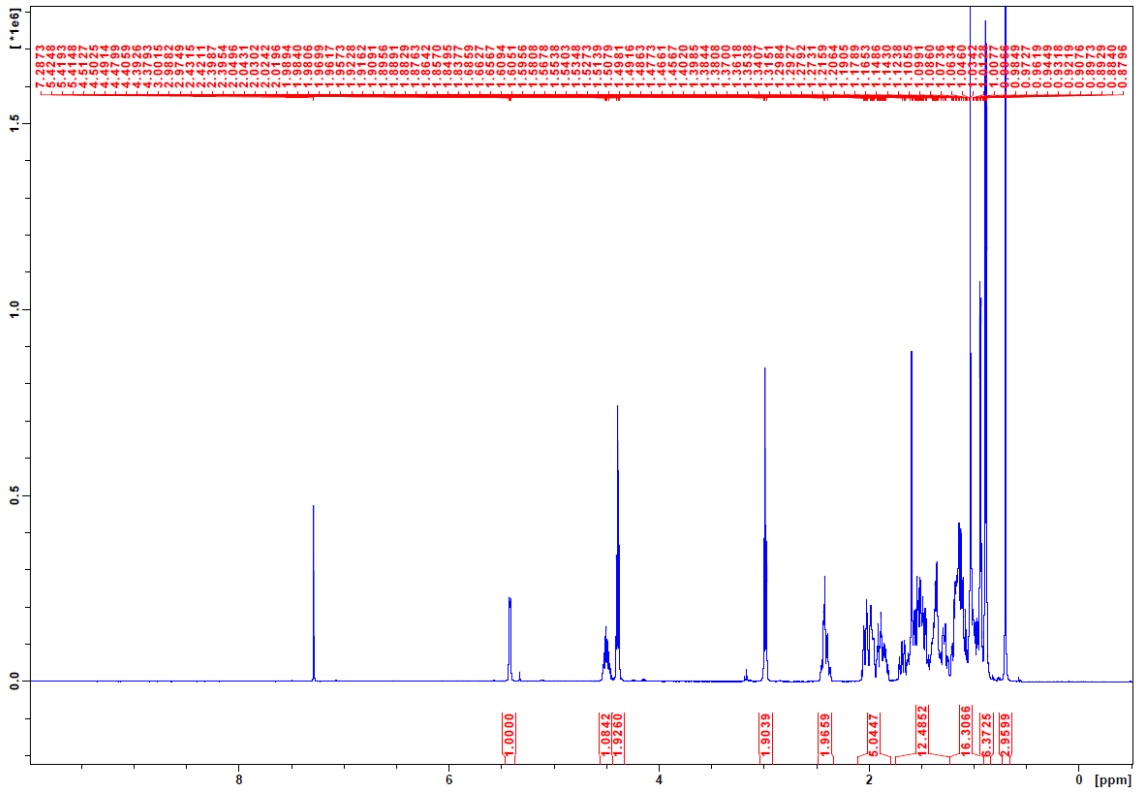

Figure 2-14. ^{1}H-NMR spectrum of Chol-S-S-OH.

To a mixture of Chol-S-S-OH (83.5 mg, 0.15 mmol) and DMAP (54 mg, 0.44 mmol) in anhydrous DCM (2 mL), a solution of triphosgene (15 mg, 0.05 mmol) in anhydrous DCM (1 mL) was added dropwise over an ice bath with stirring. The resultant solution was warmed to room temperature and further stirred for 1 h and then added dropwise to a solution of DHA (50 mg, 0.17 mmol) in anhydrous DCM (5 mL) over an ice bath. The reaction mixture was then warmed to room temperature and stirred for 12 h. After removal of solvent, the residue was purified by column chromatography on silica gel with hexane/ethyl acetate (7:1, v/v) to yield 53 mg of Chol-DHA. ^{1}H-NMR (500 MHz, $CDCl_3$): 0.65 (s, 3H), 0.88-1.20 (m, 29H), 1.30-1.75 (m, 20H), 1.80-2.08 (m, 8H), 2.37 (m, 3H),

2.61 (m, 1H), 3.00 (m, 4H), 4.41 (m, 4H), 4.52 (m, 1H), 5.42 (d, 1H), 5.47 (s, 1H), 5.60 (d, 1H). ESI-MS: m/z=899.5 (expected 899.5 for $[M+Na]^+$).

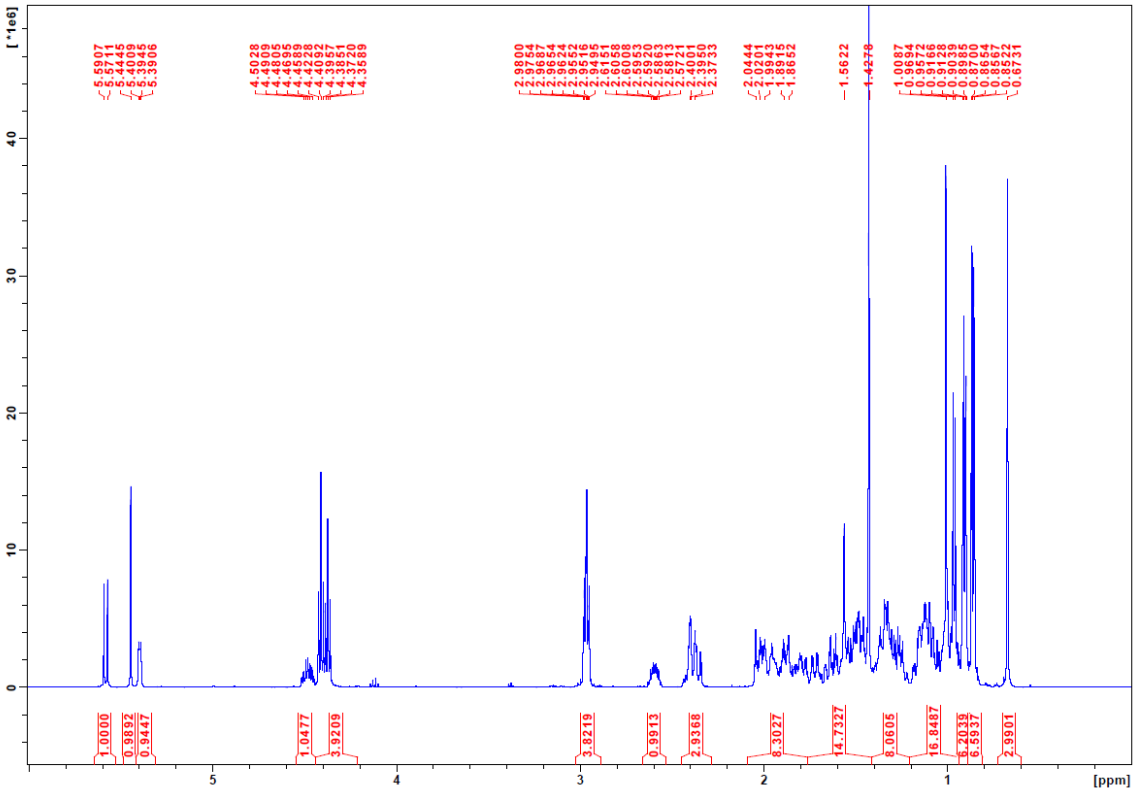

Figure 2-15. ^{1}H-NMR spectrum of chol-DHA.

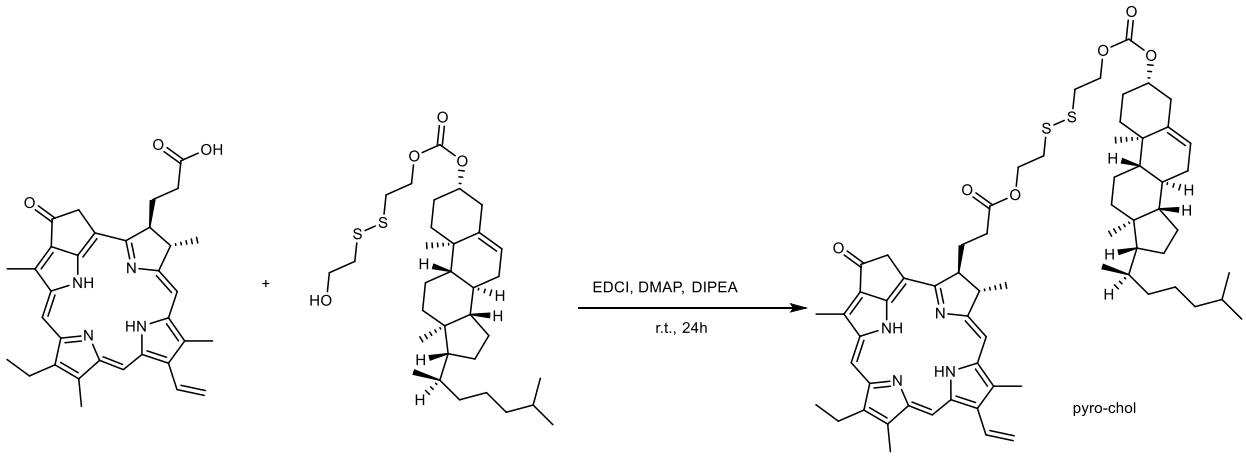

Figure 2-16. Synthesis of chol-pyro

Synthesis of chol-pyro (**Figure 2-16**)

Pyropheophytin a was prepared as previously reported.[44] A mixture of pyropheophytin a (100 mg, 0.187 mmol), Chol-SSOH (210 mg, 0.37 mmol), EDCI (72 mg, 0.37 mmol), DMAP (10 mg, 0.08 mmol) and DIPEA (100 µL) was stirred in anhydrous DCM (5 mL) at room temperature for 24 h. The mixture was loaded directly on a DCM-packed silica gel column and purified with a gradient elution from 5:1 DCM: EtOAc to 3:1 DCM: EtOAc to afford pure chol-pyro. Yield: 162 mg (79.8%). ^{1}H-NMR (500 MHz, $CDCl_3$): -1.33 (s, 2H), 0.59 (s, 3H), 0.81-1.99 (m, 18H), 1.20-1.42 (m, 16H), 1.50-1.95 (m, 12H), 2.25-2.47 (m, 4H), 2.62 (m, 1H), 2.81 (t, 2H), 2.90 (t, 2H), 3.24 (s, 3H), 3.43 (s, 3H), 3.68 (m, 4H), 4.33 (m, 6H), 4.52 (q, 2H), 5.12 (d, 1H), 5.16 (s, 1H), 5.30 (d, 1H), 6.18 (d, 1H), 6.32 (d, 1H), 8.01 (dd, 1H), 8.58 (s, 1H), 9.38 (s, 1H), 9.48 (s, 1H). ESI-MS: m/z=1083.6 (expected 1083.6 for $[M+H]^+$).

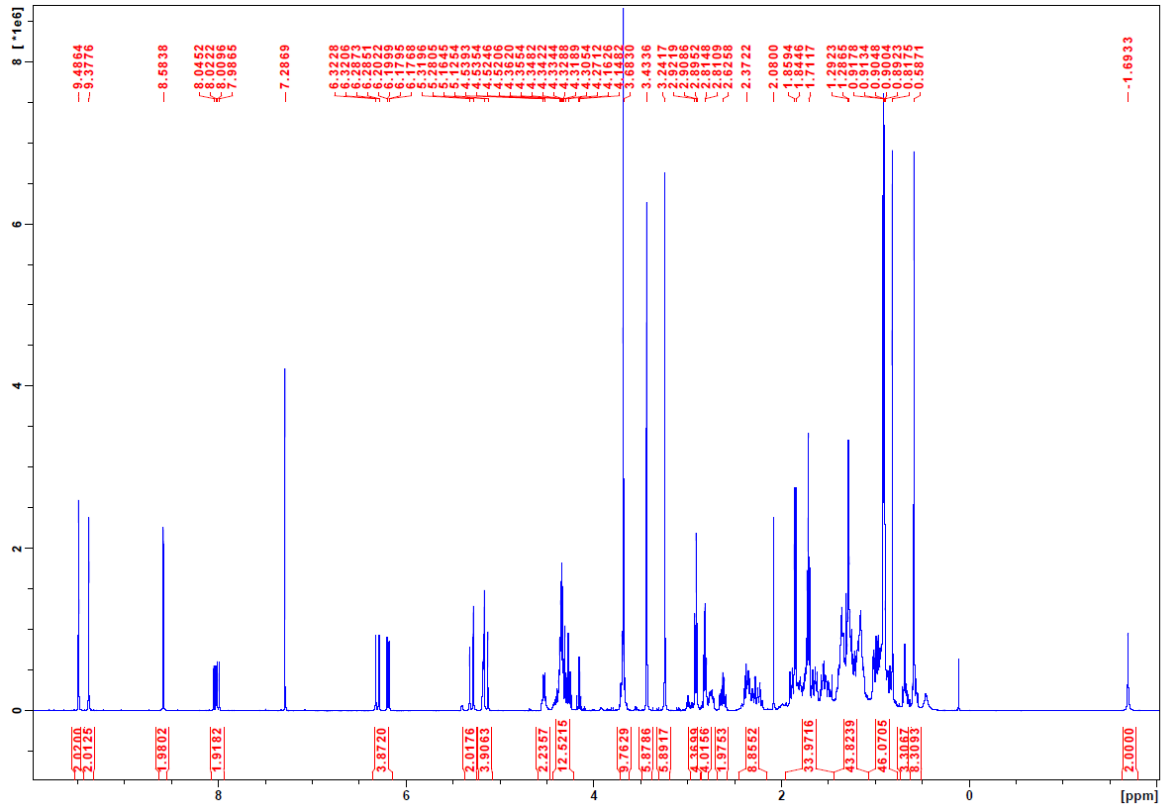

Figure 2-17. ^{1}H-NMR spectrum of chol-pyro

Synthesis of chol-AS (**Figure 2-18**)

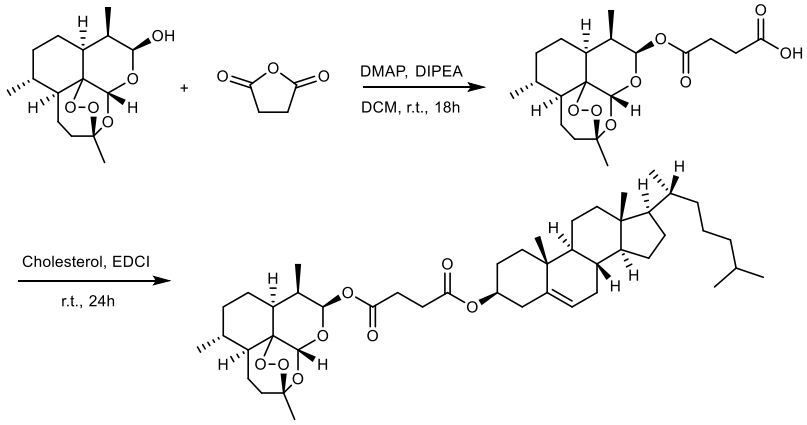

Figure 2-18. Synthesis of chol-AS

To a solution of DHA (1.136 g, 4 mmol), succinic anhydride (400 mg, 4 mmol), DMAP (121 mg, 1 mmol) in dry DCM (20mL), 0.7 ml diisopropylethylamine (DIPEA) was added and the mixture was stirred for 18 h at room temperature under N_2. Cholesterol (1.95 g, 5mmol) and *N*-(3-Dimethylaminopropyl)-*N′*-ethylcarbodiimide hydrochloride (EDCI) were added to the mixture and the solution was further stirred for 24 h at room temperature. The reaction mixture was diluted with 200 mL EtOAc and washed by 200 mL 1 M HCl solution twice and 200 mL saturated NaCl solution once. The organic layer was collected and dried via rotary evaporator to obtain the crude product which was further purified by column chromatography on silica gel with 7:1 DCM: EtOAc to obtain pure chol-AS. Yield: 1.03 g (34%). ^{1}H-NMR (500MHz, $CDCl_3$): 0.69 (s, 3H), 0.88 (m, 9H), 0.92-0.98 (m, 13H), 1.02-1.22 (m, 7H), 1.25-1.43 (m, 7H), 1.45-1.65 (m, 12H), 1.70-1.95 (m, 6H), 2.04 (m, 3H), 2.32 (d, 2H), 2.40 (td, 1H), 2.58 (m, 2H), 2.73 (m, 3H), 4.64 (m, 1H), 5.38 (d, 1H), 5.45 (s, 1H), 5.82 (d, 2H). ESI-MS: m/z=776.1 (expected 776.1 for $[M+Na]^+$).

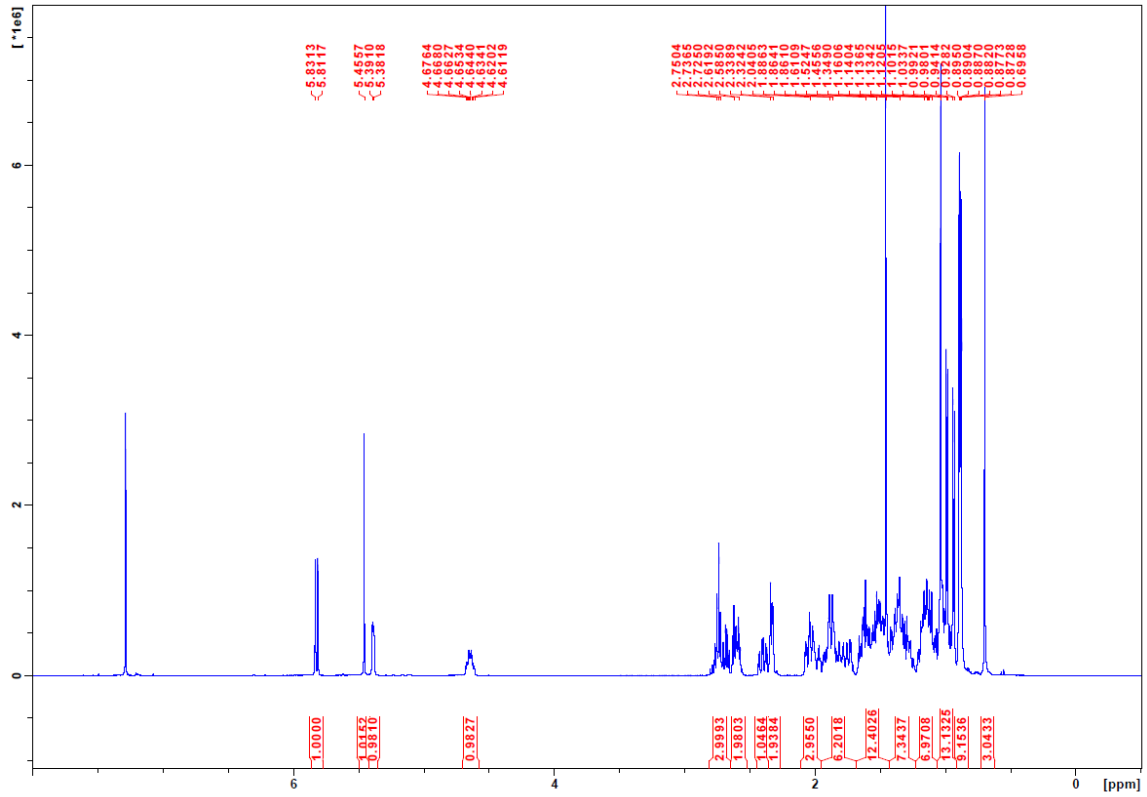

Figure 2-19. ^{1}H-NMR spectrum of chol-AS.

2.4.2 Preparation and characterization of OxPt/DHA

OxPt core was synthesized according to our previously reported method, with minor modifications.[44] The loadings of OxPt in the particles were determined by inductively coupled plasma-mass spectrometry (ICP-MS, Agilent 7700X, Agilent Technologies, USA) after digestion with nitric acid. OxPt/DHA was prepared by adding a THF solution (80 µL) of DOPC, cholesterol, DSPE-PEG2k (2:1:1 in molar ratio), chol-DHA, and OxPt core to 500 µL of 30% (v/v) ethanol/water at 50 °C. The mixture was stirred at 1,700 rpm for 1 min. THF and ethanol were completely evaporated and the solution was allowed to cool down to room temperature. The particle size and zeta potential were determined by

dynamic light scattering (DLS) using a Zetasizer (Nano ZS, Malvern, UK). Transmission electron microscopy (TEM, Tecnai Spirit, FEI, USA) was used to observe the morphology. To determine chol-DHA loading, OxPt/DHA was centrifuged at 13,000 rpm for 30 min, the supernatant was removed and the particles were re-suspended in THF which dissolves the lipid layer to release chol-DHA. The amount of chol-DHA in the nanoparticle suspension was then determined by liquid chromatography-mass spectrometry (LC-MS). The stability of OxPt/DHA was evaluated at 4 ^{o}C in 5% glucose or 37 ^{o}C in phosphate buffered saline (PBS) containing bovine serum albumin (BSA). The chol-DHA content in the nanoparticles was also determined by LC-MS before or after the addition of Triton X-100 to disrupt the lipid bilayer.

2.4.3 Preparation of fluorescently labeled NCP particle

0.5 g OxPt prodrug was mixed with 1.52 mL water and 0.98 mL 3 M NaOH to prepare a neutralized OxPt prodrug stock solution. The solution was added to an excess amount of xylenol orange solid to prepare a saturated solution. The saturated solution was centrifuged at 12000 rpm for 5 min to remove any solid before used to prepare bare NCP particle. The bare particle was prepared according to our previously reported method by changing the prodrug solution to xylenol orange-saturated prodrug solution. The coated fluorescent particle was prepared by the same method as OxPt/DHA particle. 30% of DOPC was changed to DSPE-FITC and all Chol-DHA was changed to chol-pyro.

2.4.4 *In vitro* cytotoxicity

CT26 cells or MC38 cells were seeded in 96-well plates at a density of 2 $\times 10^3$ cells per well and allowed to adhere for 24 h. Cells were then treated with different concentrations of free OxPt, free DHA, free OxPt plus DHA (OxPt+DHA), OxPt NCP, Zn/DHA, or OxPt/DHA at 2:1 molar ratio of OxPt to DHA for another 72 h. Cell viability was detected by MTS (3-(4,5-dimethylthiazol-2-yl)-5-(3-carboxymethoxyphenyl)-2-(4-sulfophenyl)-2H-tetrazo¬lium) assay (Promega, Madison, WI) according to the manufacturer's instructions.

2.4.5 *In vivo* pharmacokinetics and biodistribution analysis on mice

BALB/c mice were subcutaneously injected in the right flank with 1×10^6 CT26 cells. When the tumors reached ~100 mm^3, mice were intraperitoneal (i.p.) administration of OxPt/DHA at an OxPt dose of 8 mg/kg (2.88 mg/kg DHA). The blood was collected at 1 h, 3 h, 5 h, 8 h, 24 h, 48 h, and 72 h post-injection and immediately centrifuged at 3000 rpm for 10 min to harvest plasma samples. 25 μL plasma was digested with concentrated nitric acid for 24 h and analyzed for Pt concentration by ICP-MS. Another 100 μL plasma was extracted by EtOAc. The content of chol-DHA was quantified by LC-MS. The livers, lungs, spleens, kidneys, bladders, and tumors were also harvested, digested with concentrated nitric acid for 24 h, and analyzed for Pt concentration by ICP-MS.

2.4.6 *In vivo* toxicity on mice

C57Bl/6 mice were received a weekly i.p. dose of OxPt/DHA at 60 mg/kg OxPt (21.5 mg/kg DHA) for a total of four doses or a single i.p. dose at 80 mg/kg OxPt (28.7 mg/kg DHA). The activity level and body weights of the mice were monitored for toxicity.

2.4.7 *In vivo* anticancer efficacy

1×10^6 cells CT26 or MC38 cells were subcutaneously injected into the right flank region of 6-week BALB/c or C57Bl/6 mice, respectively. 12 days after tumor inoculation, mice were i.p. dosed with 8 mg/kg OxPt, 2.9 mg/kg DHA, and/or 75 μg PD-L1 antibody once every 3 days for up to 12 doses. Tumor growth was monitored by measurement with a digital caliper, where tumor volumes were calculated as follows: $(\text{width}^2 \times \text{length})/2$.

Tumor-free BALB/c mice were challenged with 5×10^6 CT26 cells on the contralateral flank three months after the tumors disappeared. The mice were monitored for 1 month and then rechallenged with 5×10^4 unrelated 4T1 cells.

2.4.8 LC-MS method for chol-DHA analysis

1 μL 100 ppm chol-AS solution in acetonitrile was spiked into 100 μL sample as internal standard (ISTD), then the sample was further diluted with 5 μL 20% Triton X-100 and 100 μL saturated NaCl. The mixture was extracted by 100 μL EtOAc and centrifuged at 10000 rpm for 10 min. LC-MS was performed on an Agilent 6540 ESI-Q-Tof LC-HRMS using an Agilent Zorbax SB C-18, 2.1 x 50 mm column with 10 mm guard column. Both chol-DHA and ISTD were eluted by a mixture of 95% methanol and 5% water containing 10 mM ammonium acetate and 0.1% formic acid. The integration area of chol-DHA peak

divided by the area of chol-AS peak was used to determine the concentration of chol-DHA in the original sample.

2.5 References

1. Siegel, R. L.; Miller, K. D.; Jemal, A., Cancer statistics, 2019. *CA: a cancer journal for clinicians* **2019,** *69* (1), 7-34.

2. Gouvas, N.; Tan, E.; Windsor, A.; Xynos, E.; Tekkis, P. P., Fast-track vs standard care in colorectal surgery: a meta-analysis update. *International journal of colorectal disease* **2009,** *24* (10), 1119-1131.

3. Gallagher, D. J.; Kemeny, N., Metastatic colorectal cancer: from improved survival to potential cure. *Oncology* **2010,** *78* (3-4), 237-248.

4. Sharif, S.; O'Connell, M. J.; Yothers, G.; Lopa, S.; Wolmark, N., FOLFOX and FLOX regimens for the adjuvant treatment of resected stage II and III colon cancer. *Cancer investigation* **2008,** *26* (9), 956-963.

5. Ciombor, K. K.; Wu, C.; Goldberg, R. M., Recent therapeutic advances in the treatment of colorectal cancer. *Annual review of medicine* **2015,** *66*, 83-95.

6. Ganesh, K.; Stadler, Z. K.; Cercek, A.; Mendelsohn, R. B.; Shia, J.; Segal, N. H.; Diaz, L. A., Immunotherapy in colorectal cancer: rationale, challenges and potential. *Nature Reviews Gastroenterology & Hepatology* **2019,** *16* (6), 361-375.

7. Koido, S.; Ohkusa, T.; Homma, S.; Namiki, Y.; Takakura, K.; Saito, K.; Ito, Z.; Kobayashi, H.; Kajihara, M.; Uchiyama, K., Immunotherapy for colorectal cancer. *World journal of gastroenterology: WJG* **2013,** *19* (46), 8531.

8. Kalyan, A.; Kircher, S.; Shah, H.; Mulcahy, M.; Benson, A., Updates on immunotherapy for colorectal cancer. *Journal of gastrointestinal oncology* **2018,** *9* (1), 160.

9. Yaghoubi, N.; Soltani, A.; Ghazvini, K.; Hassanian, S. M.; Hashemy, S. I., PD-1/PD-L1 blockade as a novel treatment for colorectal cancer. *Biomedicine & Pharmacotherapy* **2019,** *110*, 312-318.

10. Diaz, L. A.; Marabelle, A.; Delord, J.-P.; Shapira-Frommer, R.; Geva, R.; Peled, N.; Kim, T. W.; Andre, T.; Van Cutsem, E.; Guimbaud, R., Pembrolizumab therapy for microsatellite instability high (MSI-H) colorectal cancer (CRC) and non-CRC. American Society of Clinical Oncology: 2017.

11. Marcus, L.; Lemery, S. J.; Keegan, P.; Pazdur, R., FDA approval summary: pembrolizumab for the treatment of microsatellite instability-high solid tumors. *Clinical Cancer Research* **2019,** *25* (13), 3753-3758.

12. Overman, M. J.; McDermott, R.; Leach, J. L.; Lonardi, S.; Lenz, H.-J.; Morse, M. A.; Desai, J.; Hill, A.; Axelson, M.; Moss, R. A., Nivolumab in patients with metastatic DNA mismatch repair-deficient or microsatellite instability-high colorectal cancer (CheckMate 142): an open-label, multicentre, phase 2 study. *The Lancet Oncology* **2017,** *18* (9), 1182-1191.

13. Smith, K. M.; Desai, J., Nivolumab for the treatment of colorectal cancer. *Expert Review of Anticancer Therapy* **2018,** *18* (7), 611-618.

14. Boland, C. R.; Goel, A., Microsatellite instability in colorectal cancer. *Gastroenterology* **2010,** *138* (6), 2073-2087.

15. Comella, P.; Casaretti, R.; Sandomenico, C.; Avallone, A.; Franco, L., Role of oxaliplatin in the treatment of colorectal cancer. *Therapeutics and clinical risk management* **2009,** *5*, 229.

16. De Gramont, A.; Vignoud, J.; Tournigand, C.; Louvet, C.; Andre, T.; Varette, C.; Raymond, E.; Moreau, S.; Le Bail, N.; Krulik, M., Oxaliplatin with high-dose leucovorin and 5-fluorouracil 48-hour continuous infusion in pretreated metastatic colorectal cancer. *European journal of Cancer* **1997,** *33* (2), 214-219.

17. Diaz-Rubio, E.; Sastre, J.; Zaniboni, A.; Labianca, R.; Cortes-Funes, H.; De Braud, F.; Boni, C.; Benavides, M.; Dallavalle, G.; Homerin, M., Oxaliplatin as single agent in previously untreated colorectal carcinoma patients: a phase II multicentric study. *Annals of Oncology* **1998,** *9* (1), 105-108.

18. Kroemer, G.; Galluzzi, L.; Kepp, O.; Zitvogel, L., Immunogenic cell death in cancer therapy. *Annual review of immunology* **2013,** *31*, 51-72.

19. Tesniere, A.; Schlemmer, F.; Boige, V.; Kepp, O.; Martins, I.; Ghiringhelli, F.; Aymeric, L.; Michaud, M.; Apetoh, L.; Barault, L., Immunogenic death of colon cancer cells treated with oxaliplatin. *Oncogene* **2010,** *29* (4), 482-491.

20. Apetoh, L.; Ghiringhelli, F.; Tesniere, A.; Obeid, M.; Ortiz, C.; Criollo, A.; Mignot, G.; Maiuri, M. C.; Ullrich, E.; Saulnier, P., Toll-like receptor 4–dependent contribution of the immune system to anticancer chemotherapy and radiotherapy. *Nature medicine* **2007,** *13* (9), 1050-1059.

21. Garg, A. D.; Krysko, D. V.; Vandenabeele, P.; Agostinis, P., Hypericin-based photodynamic therapy induces surface exposure of damage-associated molecular patterns like HSP70 and calreticulin. *Cancer Immunology, Immunotherapy* **2012,** *61* (2), 215-221.

22. Garg, A. D.; Krysko, D. V.; Verfaillie, T.; Kaczmarek, A.; Ferreira, G. B.; Marysael, T.; Rubio, N.; Firczuk, M.; Mathieu, C.; Roebroek, A. J. M., A novel pathway

combining calreticulin exposure and ATP secretion in immunogenic cancer cell death. *The EMBO journal* **2012,** *31* (5), 1062-1079.

23. Dolmans, D. E.; Fukumura, D.; Jain, R. K., Photodynamic therapy for cancer. *Nature reviews cancer* **2003,** *3* (5), 380-387.

24. Morris, C. A.; Duparc, S.; Borghini-Fuhrer, I.; Jung, D.; Shin, C.-S.; Fleckenstein, L., Review of the clinical pharmacokinetics of artesunate and its active metabolite dihydroartemisinin following intravenous, intramuscular, oral or rectal administration. *Malaria journal* **2011,** *10* (1), 263.

25. Robert, A.; Coppel, Y.; Meunier, B., Alkylation of heme by the antimalarial drug artemisinin. *Chemical communications* **2002,** (5), 414-415.

26. Wang, J.; Huang, L.; Li, J.; Fan, Q.; Long, Y.; Li, Y.; Zhou, B., Artemisinin directly targets malarial mitochondria through its specific mitochondrial activation. *Plos one* **2010,** *5* (3), e9582.

27. Kong, R.; Jia, G.; Cheng, Z.-x.; Wang, Y.-w.; Mu, M.; Wang, S.-j.; Pan, S.-h.; Gao, Y.; Jiang, H.-c.; Dong, D.-l., Dihydroartemisinin enhances Apo2L/TRAIL-mediated apoptosis in pancreatic cancer cells via ROS-mediated up-regulation of death receptor 5. *PLoS One* **2012,** *7* (5), e37222.

28. Wang, Z.; Hu, W.; Zhang, J.-L.; Wu, X.-H.; Zhou, H.-J., Dihydroartemisinin induces autophagy and inhibits the growth of iron-loaded human myeloid leukemia K562 cells via ROS toxicity. *FEBS open bio* **2012,** *2*, 103-112.

29. Singh, N. P.; Lai, H., Selective toxicity of dihydroartemisinin and holotransferrin toward human breast cancer cells. *Life sciences* **2001,** *70* (1), 49-56.

30. McGready, R.; Phyo, A. P.; Rijken, M. J.; Tarning, J.; Lindegardh, N.; Hanpithakpon, W.; Than, H. H.; Hlaing, N.; Zin, N. T.; Singhasivanon, P., Artesunate/dihydroartemisinin pharmacokinetics in acute falciparum malaria in pregnancy: absorption, bioavailability, disposition and disease effects. *British journal of clinical pharmacology* **2012,** *73* (3), 467-477.

31. Li, Q. G.; Peggins, J. O.; Fleckenstein, L. L.; Masonic, K.; Heiffer, M. H.; Brewer, T. G., The pharmacokinetics and bioavailability of dihydroartemisinin, arteether, artemether, artesunic acid and artelinic acid in rats. *Journal of pharmacy and pharmacology* **1998,** *50* (2), 173-182.

32. Petros, R. A.; DeSimone, J. M., Strategies in the design of nanoparticles for therapeutic applications. *Nature reviews Drug discovery* **2010,** *9* (8), 615-627.

33. Choi, H. S.; Liu, W.; Liu, F.; Nasr, K.; Misra, P.; Bawendi, M. G.; Frangioni, J. V., Design considerations for tumour-targeted nanoparticles. *Nature nanotechnology* **2010,** *5* (1), 42-47.

34. Davis, M. E.; Chen, Z.; Shin, D. M., Nanoparticle therapeutics: an emerging treatment modality for cancer. In *Nanoscience and technology: A collection of reviews from nature journals*, World Scientific: 2010; pp 239-250.

35. Allen, T. M.; Cullis, P. R., Drug delivery systems: entering the mainstream. *Science* **2004,** *303* (5665), 1818-1822.

36. Xu, Z.; Wang, D.; Xu, S.; Liu, X.; Zhang, X.; Zhang, H., Preparation of a camptothecin prodrug with glutathione-responsive disulfide linker for anticancer drug delivery. *Chemistry–An Asian Journal* **2014,** *9* (1), 199-205.

37. Wang, Q.; Guan, J.; Wan, J.; Li, Z., Disulfide based prodrugs for cancer therapy. *RSC Advances* **2020,** *10* (41), 24397-24409.

38. Guo, Y.; Zhang, P.; Zhao, Q.; Wang, K.; Luan, Y., Reduction-sensitive polymeric micelles based on docetaxel-polymer conjugates via disulfide linker for efficient cancer therapy. *Macromolecular Bioscience* **2016,** *16* (3), 420-431.

39. Tolbatov, I.; Coletti, C.; Marrone, A.; Re, N., Insight into the electrochemical reduction mechanism of Pt (IV) anticancer complexes. *Inorganic Chemistry* **2018,** *57* (6), 3411-3419.

40. Duong, H. T. T.; Huynh, V. T.; de Souza, P.; Stenzel, M. H., Core-cross-linked micelles synthesized by clicking bifunctional Pt (IV) anticancer drugs to isocyanates. *Biomacromolecules* **2010,** *11* (9), 2290-2299.

41. Hagel, A. F.; Albrecht, H.; Dauth, W.; Hagel, W.; Vitali, F.; Ganzleben, I.; Schultis, H. W.; Konturek, P. C.; Stein, J.; Neurath, M. F., Plasma concentrations of ascorbic acid in a cross section of the German population. *Journal of International Medical Research* **2018,** *46* (1), 168-174.

42. Kuiper, C.; Dachs, G. U.; Currie, M. J.; Vissers, M. C. M., Intracellular ascorbate enhances hypoxia-inducible factor (HIF)-hydroxylase activity and preferentially suppresses the HIF-1 transcriptional response. *Free Radical Biology and Medicine* **2014,** *69*, 308-317.

43. Munzone, E.; Colleoni, M., Clinical overview of metronomic chemotherapy in breast cancer. *Nature reviews Clinical oncology* **2015,** *12* (11), 631.

44. He, C.; Duan, X.; Guo, N.; Chan, C.; Poon, C.; Weichselbaum, R. R.; Lin, W., Core-shell nanoscale coordination polymers combine chemotherapy and photodynamic therapy to potentiate checkpoint blockade cancer immunotherapy. *Nature communications* **2016,** *7* (1), 1-12.

Chapter 3. Co-delivery of Dihydroartemisinin and Pyropheophorbide-Iron Elicits Ferroptosis to Potentiate Cancer Immunotherapy

3.1 Introduction

Ferroptosis is a type of regulated cell death where iron plays an important role and can be inhibited by iron chelators.[1] Discovered in 2012, ferroptosis is a distinctive cell death regulation mechanism from apoptosis.[2] Erastin[3] and RSL3[4], among the earliest ferroptosis inducers discovered, were found to be able to affect signaling to modulate labile iron pool inside cells. Further studies showed that lipophilic reactive oxygen species (ROSs) were involved in ferroptosis since ferroptosis was strongly suppressed by lipophilic antioxidants.[5] The mechanism to trigger ferroptosis became relatively clear in recent years. Catalyzed by labile iron or iron-containing lipoxygenases[6-7], unsaturated lipids, especially polyunsaturated fatty acids (PUFAs) form unstable lipid hydroperoxides which can damage the membrane structure of a cell. With the help of a complex network which is believed to originate from the Great Oxidation Event in the early history of eukaryotes, cells are able to survive by reducing toxic lipid hydroperoxides.[1] Cystine (cysteine disulfide, Cys_2) is imported by the cell surface Cys_2/glutamate antiporter system x_c^- and synthesized to be glutathione (GSH).[8-9] Glutathione peroxidase 4 (GPX4) uses GSH as a reducing agent to detoxify lipid hydroperoxides (**Figure 3-1**).[8, 10-11]Pathways related to selenoprotein synthesis also influence ferroptosis since GPX4 is a selenoprotein.[12] Research showed that inhibiting key points of the detoxification network like x_c^{-}[2, 13] or GPX4[14] successfully triggered ferroptosis. Hence, directly introducing labile Fe^{II} to catalyze the formation of lipid hydroperoxides triggered ferroptosis also showed great potential in killing cancer cells.[15-17]

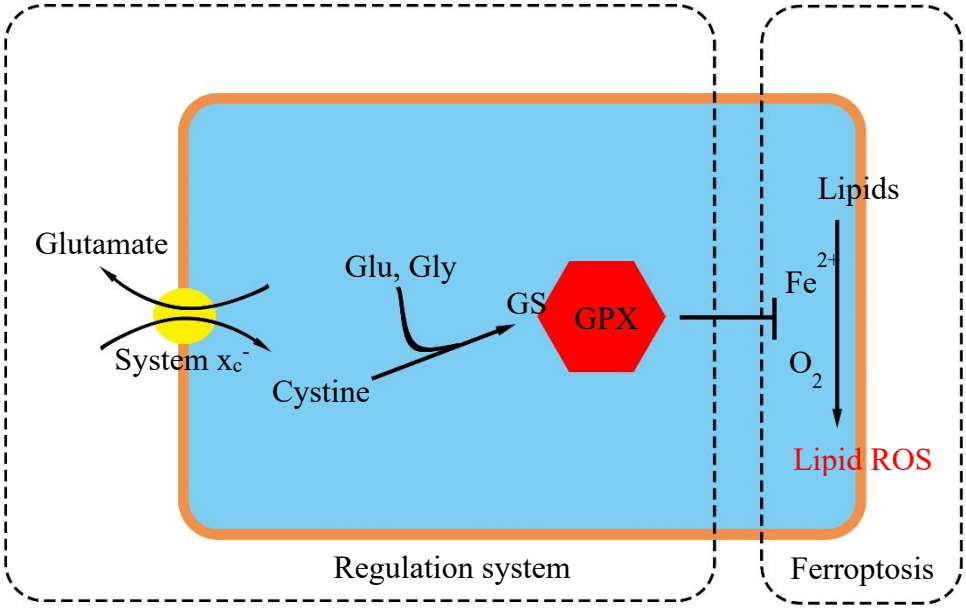

Figure 3-1. Schematic illustration of ferroptosis and its regulation system.

Unlike immunologically silent apoptosis,[18] ferroptosis is considered to be immunogenic.[19-22] Ferroptosis induced in mouse tumor models was reported to cause immune cell infiltration into the tumor sites.[23] This unique feature of ferroptosis makes it a potential approach for cancer immunotherapy. Neutralizing negative immune checkpoints with anti-programmed cell death protein 1 (PD-1) or anti-programmed death ligand 1 (PD-L1) antibodies has been proved to be effective on lung cancer, head and neck cancer, bladder cancer, and so on but they are limited by the immunosuppressive environment in the majority of cancer patients.[24-26] Ferroptosis can cause T-cell infiltration to immunologically "cold" tumors and convert them into "hot" tumors which may have better response to immunotherapy.

Dihydroartemisinin (DHA) is the active metabolite of a widely used antimalarial drug artemisinin.[27] The peroxide bridge in the molecule is believed to be able to decompose when catalyzed by labile Fe^{II} compounds like heme inside the cell and then generate ROS and cause ROS related cell death.[28-31] Studies showed the anticancer activity of DHA due to relatively high labile iron concentration in cancer cells, but DHA has not been used for anticancer activities clinically because of its instability in water and short circulation half-life (<15 min).[32]

As shown in Chapter 2, DHA is an immunogenic cell death (ICD) inducer that can significantly enhance the efficacy of oxaliplatin and anti-PD-L1 antibody. ROS generated by DHA not only reacts with proteins to disrupt proteins,[33-35] but also reacts with lipid in membranes to cause ferroptosis.[36-37] We hypothesize that co-delivery of labile Fe^{II} compounds and DHA could enhance the ferroptosis caused by DHA. By using the NCP platform, we can achieve the co-delivery of both compounds in their prodrug forms where DHA is protected as a relatively stable cholesterol conjugate and labile pyro-Fe^{II} is protected by oxidizing it to pyro-Fe^{III}. Upon entering cancer cells via endocytosis, pyro-Fe^{III} can be reduced to pyro-Fe^{II} and catalyze the decomposition of DHA and chol-DHA, hence triggering ferroptosis and increasing tumor immunogenicity (**Figure 3-2**).

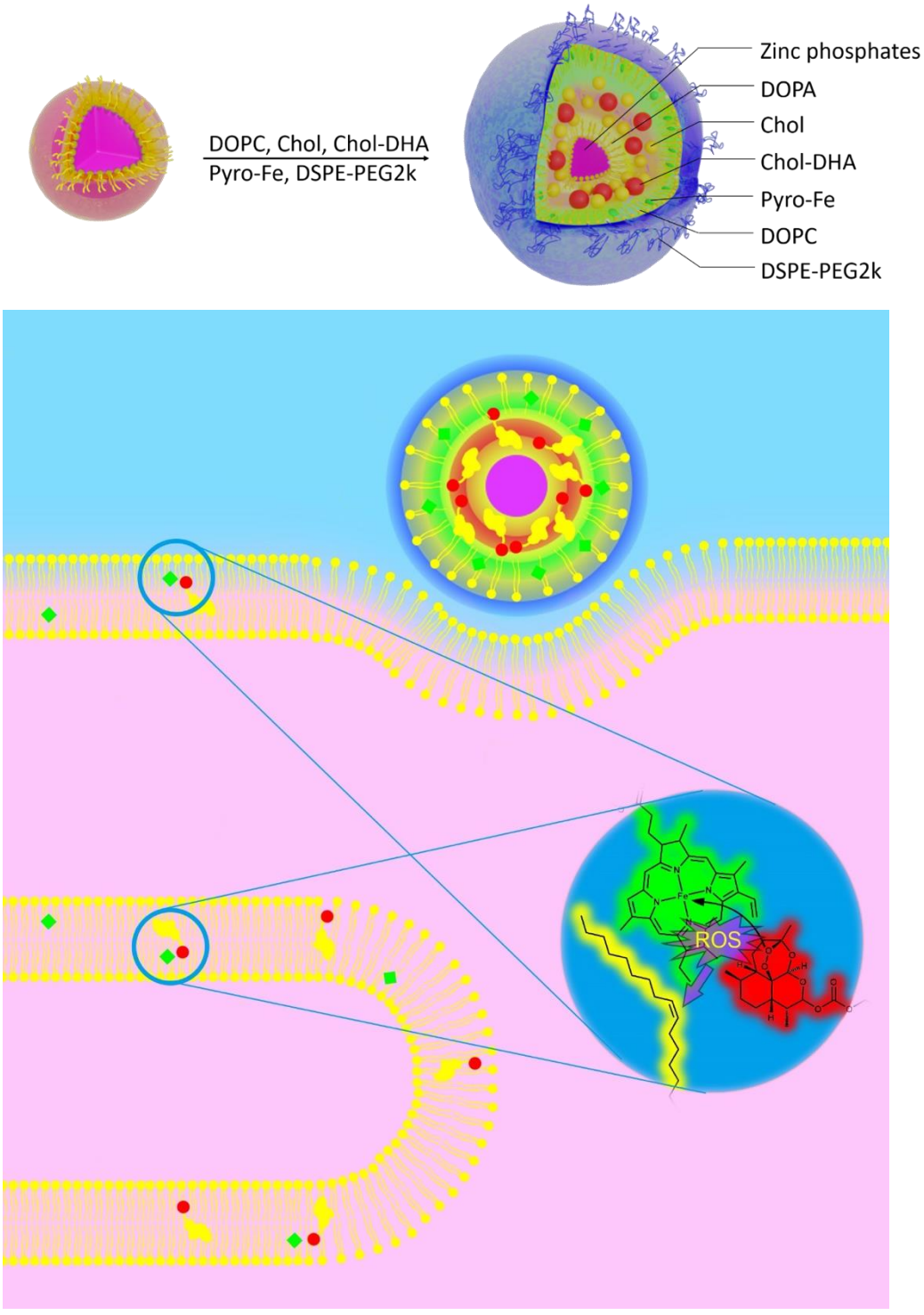

Figure 3-2. Schematic illustration of ZnP@DHA/Pryo-Fe particle and its function inside cells.

3.2 Results and discussion

3.2.1 Preparation of ZnP@DHA, ZnP@Pyro-Fe, and ZnP@DHA/Pyro-Fe

Chol-DHA prodrug was synthesized as previously described in Chapter 2. Pyro-Fe^{III} was synthesized by refluxing pyrolipid with $FeCl_2$ followed by air oxidation.

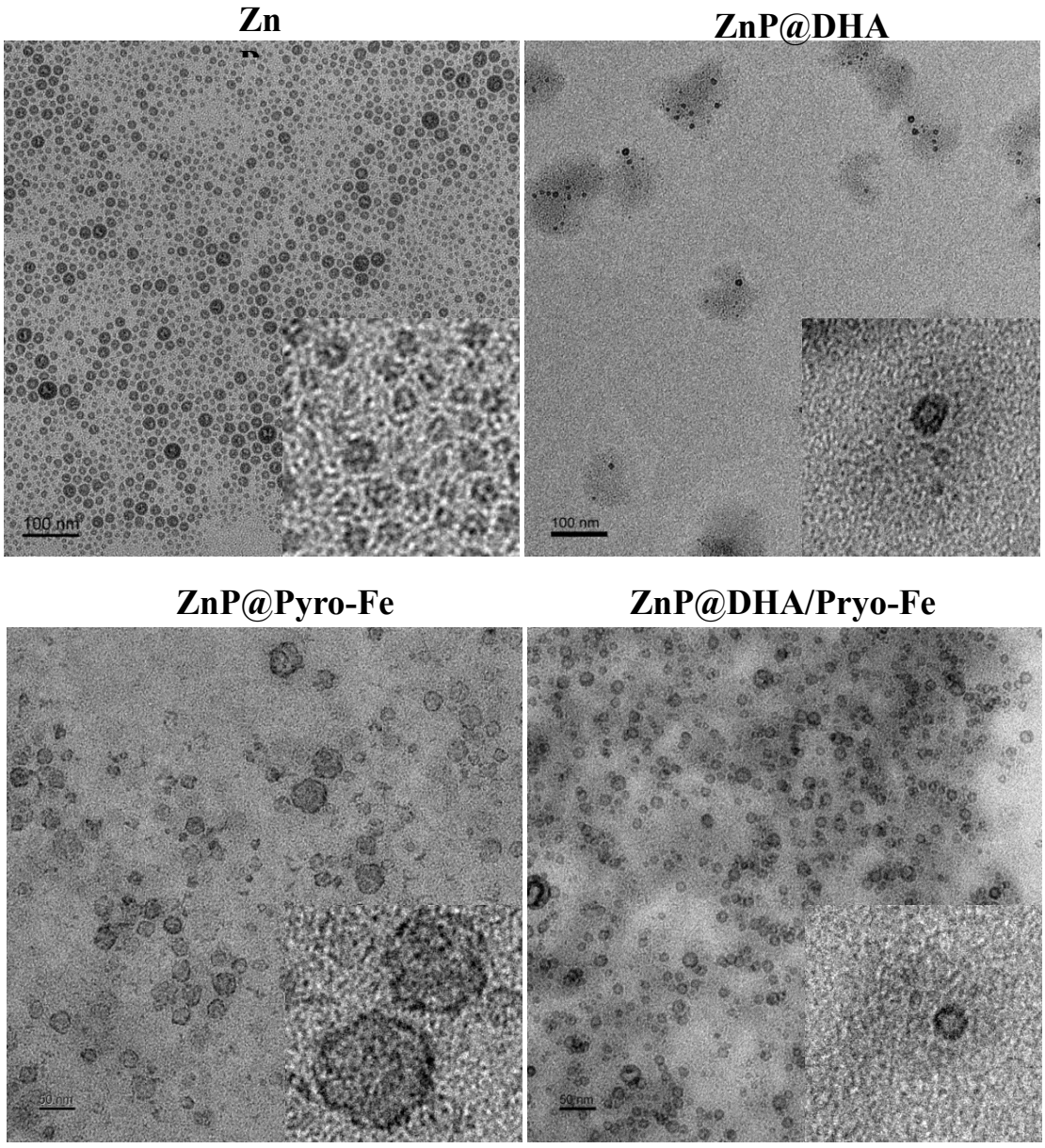

Figure 3-3. TEM images of bare ZnP particle core, ZnP@DHA, ZnP@Pyro-Fe, and ZnP@DHA/Pryo-Fe.

The Zn-pyrophosphate (ZnP) core was first synthesized by mixing a microemulsion containing $Zn(NO_3)_2$ and a microemulsion containing $Na_4P_2O_7$. Zn^{2+} ions and pyrophosphate groups polymerized in the presence of 1,2-dioleoyl-sn-glycero-3-phosphate sodium salt (DOPA) to form ZnP NCP core with a Z-average diameter of 25.10 ± 0.71 nm and a polydispersity index (PDI) of 0.13 ± 0.01 as determined by dynamic light scattering (DLS). The transmission electron microscopy (TEM) image showed that ZnP was generally spherical in shape with good dispersity. ZnP was further coated with a mixture of lipids containing 1,2-dioleyl-sn-glycero-3-phosphocholine (DOPC), cholesterol, and 1,2-diastearoyl-sn-glycero-3-phosphoethanolamine-N-[amino(polyethylene glycol)2000] (DSPE-PEG2k) in the presence of Chol-DHA or/and Pyro-Fe^{III} to afford nanoparticles of ZnP@DHA, ZnP@Pyro-Fe, or ZnP@DHA/Pyro-Fe, respectively. When phospholipid and cholesterol self-assembled around the particle core to form a lipid bilayer, pyro-Fe^{III} was incorporated into the bilayer due to its amphiphilic phospholipid feature and chol-DHA was loaded together with cholesterol in the hydrophobic part of the lipid bilayer. The loadings of chol-DHA and pyro-Fe^{III} were determined by liquid chromatography-mass spectrometry (LC-MS) and inductively coupled plasma-mass spectrometry (ICP-MS) to be 10.6 ± 0.5 and 13.2 ± 0.6%, respectively. ZnP@DHA, ZnP@Pyro-Fe, and ZnP@DHA/Pryo-Fe were observed to be well-dispersed, uniformly spherical nanoparticles by TEM (**Figure 3-3**), and had similar Z-average diameter of ~80 nm which allow them to escape from renal filtration and passively target to tumor via the EPR effect. These nanoparticles exhibited favorable structural stability under physiological

environment, as evidenced by consistent size and PDI when incubated with 5 mg/mL bovine serum albumin (BSA) for up to 24 h (**Figure 3-4**).

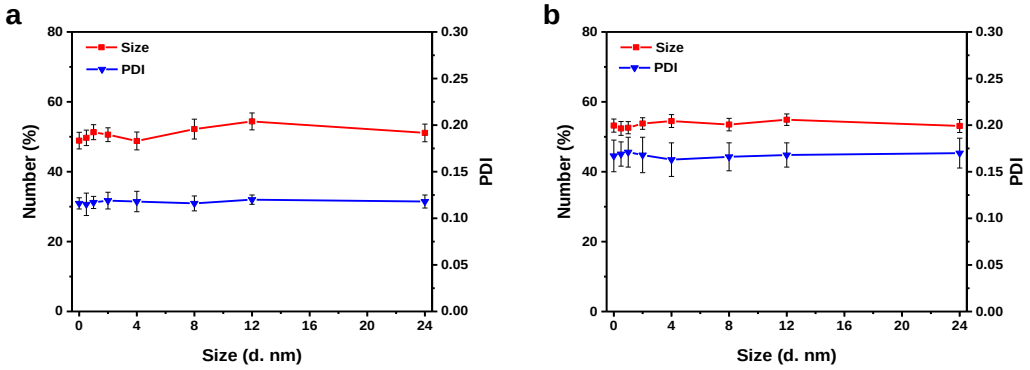

Figure 3-4. Time-dependent particle size and PDI changes of ZnP@DHA (a) and ZnP@Pyro-Fe (b) in PBS containing 5 mg/mL BSA at 37 °C.

3.2.2 Pyro-Fe catalyzes ROS production from DHA

We investigated the catalytic effect of iron in a reductive environment on DHA/chol-DHA reduction by measuring the amount of remaining chol-DHA after incubation of ZnP@Pyro-Fe and/or cysteine in the presence of 0.5% Triton X-100. The surfactant Triton X-100 was used to disrupt the lipid bilayer and release compounds loaded into the particles. Chol-DHA decomposed via the proton catalyzed mechanism as described in Chapter 2 without iron and reducing agents. When cysteine was added to the solution, the rate of chol-DHA decomposition slightly increased due to additional DHA release via the disulfide exchange mechanism. The addition of ZnP@Pyro-Fe showed no effect on chol-DHA degradation, but with cysteine as a reducing agent, the rate of chol-DHA degradation significantly increased. More than half of chol-DHA degraded in the presence of iron and reducing agent within the first half-hour, while reducing environment itself only caused half amount of chol-DHA degradation in 2 hours (**Figure 3-5** a). Pyro-Fe^{III} on ZnP@Pyro-

Fe was not able to catalyze DHA/chol-DHA degradation, while the Fe^{II} species generated in reducing environments could act as a catalyst.

We then tested if Pyro-Fe could enhance ROS production from DHA. When exposed to air, ZnP@Pyro-Fe catalyzed the generation of ROS directly from O_2 in the presence of cysteine acting as a reducing agent, with an approximately 8-fold increase in the ROS amount versus the background level. The addition of ZnP@DHA further increased ROS production to approximately 10-fold. However, in the absence of O_2, ZnP@Pyro-Fe could not generate ROS, while ZnP@DHA/Pyro-Fe increased ROS amount to approximately 6-fold with the help of cysteine (**Figure 3-5** b and c). This result further proves that it is the reduced form of pyro-Fe acting as a catalyst to generate ROS directly from the air or chol-DHA.

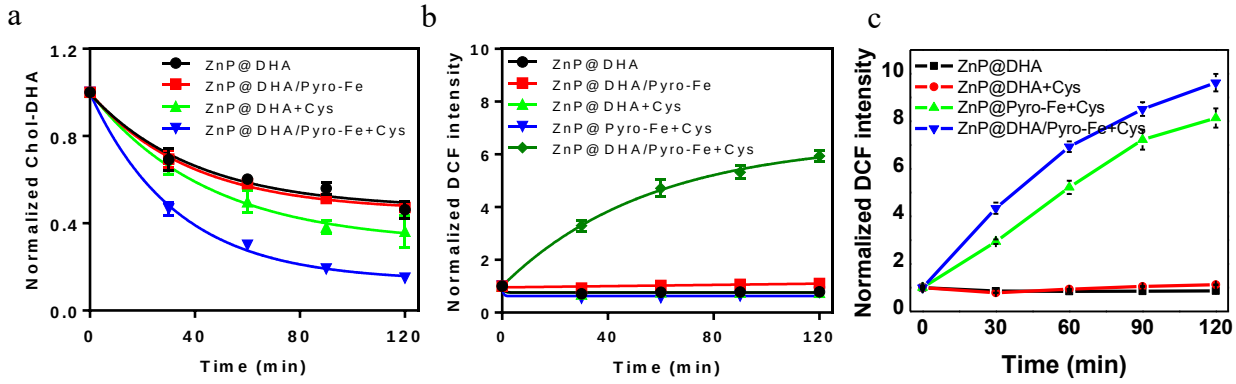

Figure 3-5. Chol-DHA decomposition and ROS generation catalyzed by pyro-Fe. (a) Decomposition of Chol-DHA in ZnP@DHA/Pyro after incubation with cysteine in the presence of 0.5% Triton X-100. (b) ROS generation of chol-DHA in oxygen-free condition when catalyzed by iron. (c) ROS generation of pyro-Fe when exposed to air.

3.2.3 Pyro-Fe enhances the cytotoxicity of DHA

We examined the cellular uptake and cytotoxicity of the particles. ZnP@Pyro-Fe showed a 24.8-fold increase of intracellular iron concentration after 24 h incubation compared to

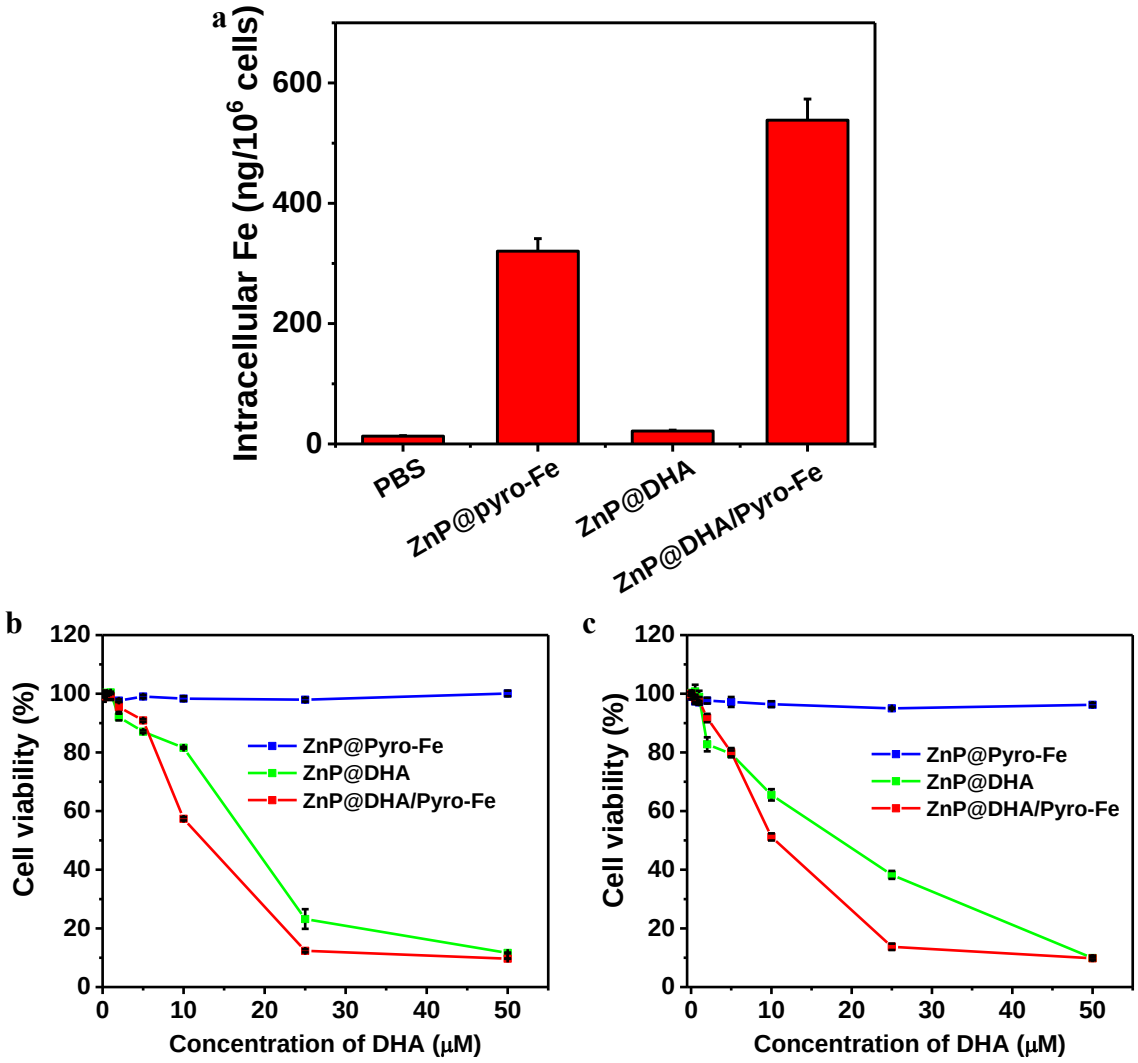

Figure 3-6. (a) Cellular uptake of particles in CT26 cells when treated with ZnP@DHA, ZnP@Pyro-Fe, or ZnP@DHA/Pyro-Fe at the concentration of 10 μM Pyro-Fe or/and 10 μM DHA. (b) Cytotoxicity of particles on CT26 cells. (c) cytotoxicity of particles on MC38 cells.

the PBS control group. Interestingly, incubation with ZnP@DHA/Pyro-Fe increased the intracellular iron content by 41.6-fold, probably due to membrane damage caused by the particle (**Figure 3-6** a).

ZnP@Pyro-Fe showed no cytotoxicity at a concentration of 50 μM on both MC38 and CT26 cells. However, incorporating Pyro-Fe into ZnP@DHA to form ZnP@DHA/Pyro-Fe significantly enhanced the cytotoxicity of ZnP@DHA, decreasing its IC_{50} value from 16.5 ± 1.2 to 8.0 ± 1.2 μM on CT26 cells and 14.8 ± 1.6 to 5.2 ± 0.9 μM on MC38 cells, respectively, as compared to ZnP@DHA (**Figure 3-6** b and c, **Table 3-1**).

Table 3-1. DHA IC_{50} value (μM) in CT26 and MC38 cells treated with various formulations.

	ZnP@Pyro-Fe	**ZnP@DHA**	**ZnP@DHA/Pyro-Fe**
CT26	> 50	16.5 ± 1.2	11.5 ± 0.5
MC38	> 50	14.8 ± 1.6	10.2 ± 0.7

We further evaluated the mechanism of the enhanced cytotoxicity induced by ZnP@DHA/Pyro-Fe. Cell electron microscopy (EM) first confirmed the ferroptosis induced by ZnP@DHA/Pyro-Fe. Cells treated with ZnP@DHA/Pyro-Fe showed smaller, ruptured mitochondria with increased mitochondrial membrane intensities, a typical pathological morphology of mitochondria observed in artemisinin derivative triggered ferroptosis (**Figure 3-7**).[38]

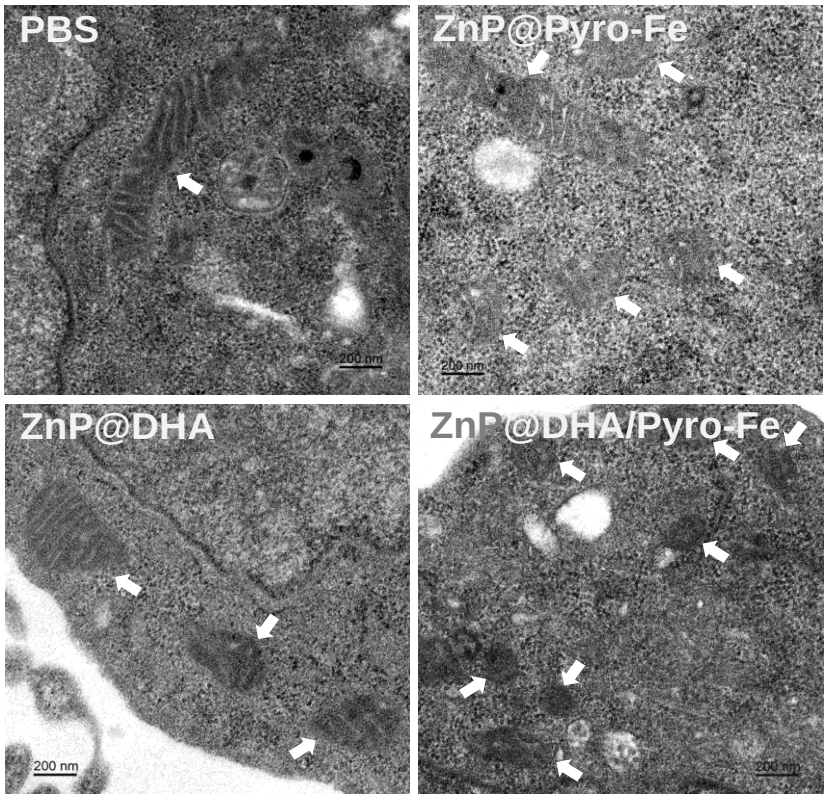

Figure 3-7. EM images of ZnP@DHA/Pyro-Fe treated cells showing smaller, ruptured mitochondria with increased mitochondrial membrane densities caused by ferroptosis.

CT26 cells exposed to 10 μM ZnP@DHA showed a significantly decreased number of cells in the S phase (32.5%) and G_0/G_1 phase (32.2%), and a corresponding increased number of cells in the G_2/M phase (35.4%) when compared to the control group (48.0%, 40.1%, and 11.1%% for S, G_0/G_1, and G_2/M phases, respectively). ZnP@DHA/Pyro-Fe exhibited the most effective induction of the arrest of cell growth in the G_2/M phase (42.9%), directly correlating with the inhibition of cell proliferation (**Figure 3-8**). The enhancement of DHA antitumor activity by iron suggests that simultaneous administration

of artemisinin-like drugs and intracellular iron compounds may present a simple and effective way to treat cancer.

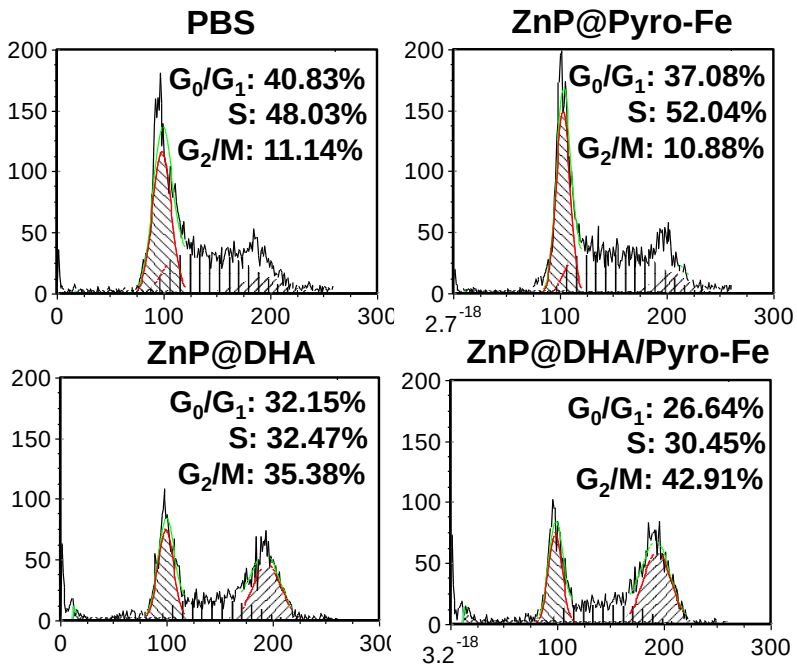

Figure 3-8. Cell cycle of CT26 cells treated with various formulations of particles.

3.2.4 Pyro-Fe facilitates intracellular ROS generation

Knowing that pyro-Fe could induce ROS generation itself or with chol-DHA, we then examined intracellular ROS generation and its relationship with cell death caused by the particle. A cell-permeable fluorogenic 2′,7′-Dichlorodihydrofluorescin diacetate (H_2-DCFDA) probe that can be oxidized by different ROS and converted to a highly fluorescent dye (DCF) was used to determine intracellular ROS levels. Cells treated with ZnP@DHA alone or with ZnP@DHA/Pyro-Fe showed more and stronger DCF staining (**Figure 3-9** a). Quantitative analysis by flow cytometry revealed stronger DCF fluorescence intensity and

more DCF positive cells after incubation with ZnP@DHA/Pyro-Fe (**Figure 3-9** b), which correlates with cell death.

Intracellular ROS have multiple effects as they can cause damage to the lipid membrane, DNAs, proteins, and subcellular organelles by direct oxidation reactions or through secondary products of these reactions. ROS can also mediate numerous physiological processes including the innate immune response and cell signaling.[39 40] DNA double-strand break (DSB), one of the most critical DNA lesions related to cell-death, induces the phosphorylation of the histone, H2AX. This newly phosphorylated protein, γ-H2AX, is the first step in recruiting and localizing DNA repair proteins, thus is an early marker for the identification of DNA DSB.[41] ZnP@DHA significantly increased the number of γ-H2AX foci in CT26 cells, suggesting that DHA damages DNA via oxidation by the generated ROS. Due to the enhancement of the ROS production, Pyro-Fe further enhanced the DNA damage effect of DHA, as evidenced by the increased formation of γ-H2AX foci (**Figure 3-9** c).

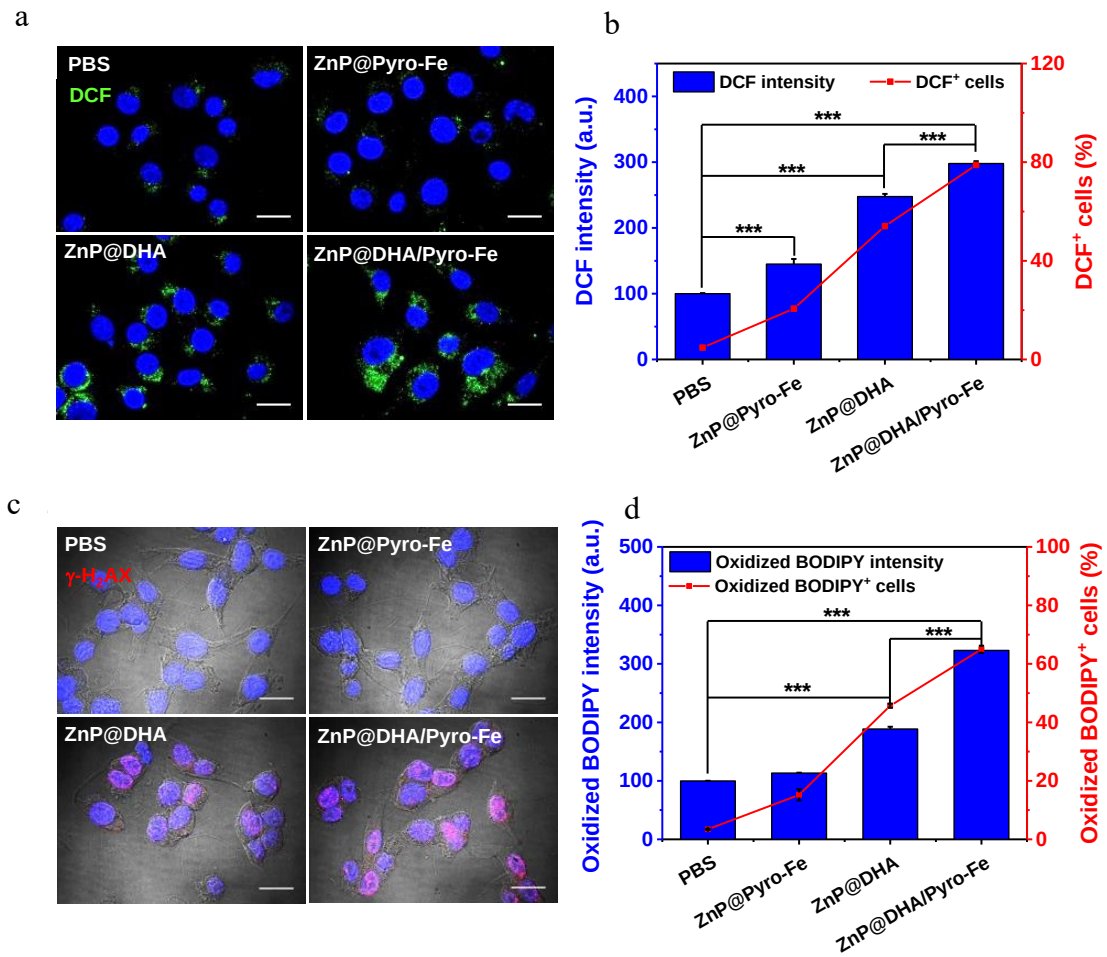

Figure 3-9. (a) Pyro-Fe enhances intracellular ROS generation as stained by H_2-DCFDA. (b) Quantitative analysis of DCF staining. (n = 3) (c) DNA double-strand breaks shown by increased level of γ-H2AX. (d) Lipid peroxidation stained by BODIPY C11. (n = 3). * $p < 0.05$, ** $p < 0.01$, *** $p < 0.001$. Scale bar=20 μm.

The effect of DHA on lipid peroxidation was investigated using BODIPY C11 (581/591), a specific sensor for intracellular lipid peroxidation by shifting the fluorescence emission from red to green. Quantitative analysis revealed the increase in the intensity of oxidized BODIPY C11 (581/591) (188.7 ± 3.8 vs 99.8 ± 0.3 in control) and the number of oxidized

BODIPY C11 (581/591) positive cells (45.7 ± 0.7%) in response to ZnP@DHA, indicating increased lipid peroxidation. ZnP@DHA/Pyro-Fe led to a more pronounced increase in the number of cells with lipid peroxidation (65.0 % ± 1.2%) and the intensity of oxidized BODIPY C11 (581/591) (323.0 ± 3.6), confirming the enhancement of DHA-based ROS generation by Pyro-Fe (**Figure 3-9** d). DNA damage and lipid peroxidation results indicate that DHA treatment causes a multitude of subcellular changes to cause cancer cell death.

3.2.5 Pyro-Fe enhances DHA-induced ferroptosis

Iron-dependent ROS generation and lipid peroxidation have been described as the driving forces for ferroptosis, although their underlying molecular mechanism remains unclear.[2 42] As both pyro-Fe and chol-DHA are very hydrophobic, we hypothesized that they would be localized to lipid-rich intracellular areas after cell internalization to cause strong lipid oxidation and ferroptosis. Furthermore, as the iron ion is chelated to the tetradentate pyropheophorbide ring, the catalytic effect of pyro-Fe should not be affected by iron chelators. We tested whether lipid ROS scavenger, ferrostatin 1 (Fer-1), or iron chelator, deferoxamine (DFO) could block cell death via scavenging the Fe pool. Co-addition of Fer-1 (20 μM) or DFO (0.1 μM) reduced but did not fully block the cytotoxicity of ZnP@DHA and rescued the viability of CT26 cells to approximately 75% from 48% for the ZnP@DHA treatment only, indicating that labile Fe is partially responsible for DHA-induced cell death through ferroptosis. The total ROS accumulation and lipid peroxidation induced by ZnP@DHA were also suppressed by co-treatment with Fer-1 or DFO, as indicated by decreased DCF signal and BODIPY C11 (581/591) oxidation. As expected, the addition of DFO to the ZnP@DHA/Pyro-Fe treatment did not rescue CT26 cells from cell death, ROS accumulation, and lipid peroxidation since labile iron is already protected

in pyro-Fe, indicating significant enhancement of DHA-induced ferroptosis by co-delivered Pyro-Fe. (**Figure 3-10**)

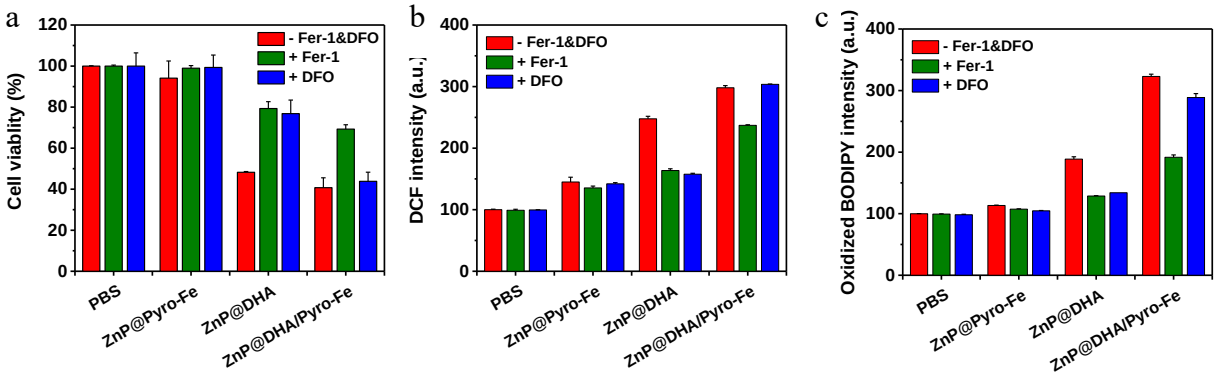

Figure 3-10. (a) Cytotoxicity of various formulations of particles with or without ROS scavenger Fer-1 or iron chelator DFO. (b) Intracellular ROS generation caused by particles with or without Fer-1 or DFO, as stained by DCF. (c) Lipid oxidation caused by particles with or without Fer-1 or DFO, as stained by BODIPY C11.

3.2.6 Pyro-Fe enhances the antitumor efficacy of DHA

Pharmacokinetic and biodistribution studies were carried out on SD rats and CT26-tumor bearing mice with ZnP@DHA/Pyro-Fe with 20 mol% pyro-Fe replaced by fluorescent pyrolipid. Fluorescence intensities of plasma or homogenized organ samples were used to determine the concentration of the particle. The particle showed a prolonged blood circulation with a half-life of 3.5 h and an accumulation of 5% ID/g in tumors 24 h post injection (**Figure 3-11** and **table 3-2**), indicating that the particle escapes from MPS uptake and enriches in tumors through the EPR effect.

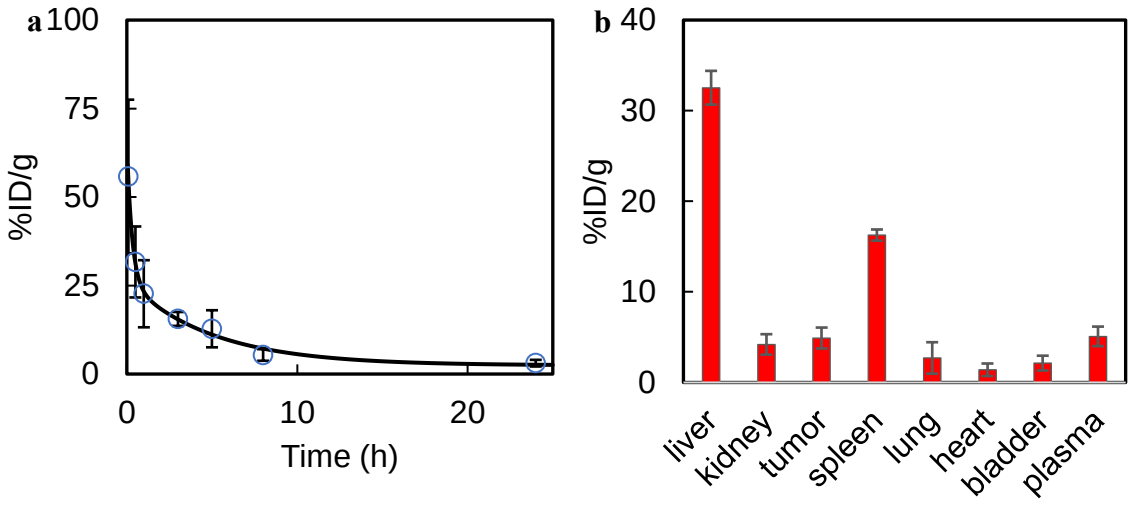

Figure 3-11. (a) plasma concentration of ZnP@DHA/Pyro-Fe measured by pyrolipid. (b) biodistribution of ZnP@DHA/Pyro-Fe. n = 3.

Table 3-2. PK parameters of ZnP@DHA/Pyro-Fe

Parameter	**Unit**	**Value**
$t_{1/2\alpha}$	h	0.21
$t_{/2\beta}$	h	3.5
C_0	μg/ml	261.24
$AUC_{0\text{-}inf}$	μg/ml·h	749.932
AUMC	μg/ml·h^2	5058.63
MRT	h	6.74

We next examined if Pyro-Fe could enhance the antitumor activity of DHA on CT26 and MC38 colorectal tumor models established subcutaneous injection of cancer cells into the right flank regions of BALB/c and C57BL/6 mice, respectively. When the tumors reached ~100 mm^3, mice were intraperitoneally (i.p.) injected with ZnP@DHA, ZnP@Pyro-Fe, or ZnP@DHA/Pyro-Fe at a DHA dose of 10 mg/kg and/or Fe dose of 2 mg/kg every 3 days. Compared to the rapidly increasing tumor volumes in the PBS group, ZnP@DHA moderately inhibited CT26 tumor growth, resulting in a tumor growth inhibition index (TGI, defined as [1-(mean volume of treated tumors/mean volume of control tumors)] ×100%) of 28.8%. In contrast, the treatment of ZnP@DHA/Pyro-Fe significantly inhibited tumor growth to afford a TGI of 57.9% (**Figure 3-12** a), indicating the enhancement of DHA antitumor activity by Pyro-Fe. The average tumor weights were also reduced significantly, with 65.1% and 32.5 % reduction in tumor weights over the PBS control for ZnP@DHA/Pyro-Fe and ZnP@DHA groups, respectively. (**Figure 3-12** b)

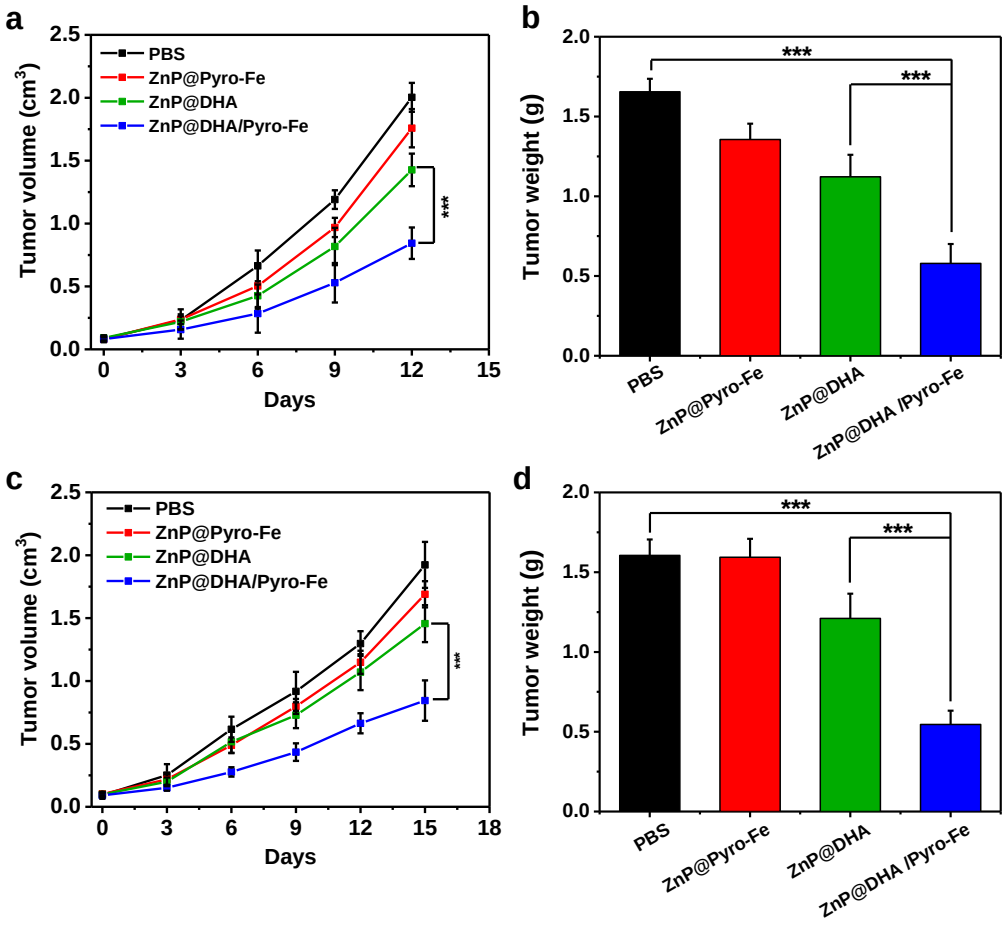

Figure 3-12. Tumor growth curve (a, c) and final tumor weight (b, d) of CT26 (a,b) and MC38 (c,d) tumors treated with various formulation of particles (n = 6). * $p < 0.05$, ** $p < 0.01$, *** $p < 0.001$

We also observed a similar tumor growth inhibitory effect on the MC38 tumor model with TGI values of 56.1% and 24.3% for ZnP@DHA/Pyro-Fe and ZnP@DHA groups, respectively (**Figure 3-12**c). The weights of tumors treated with PBS, ZnP@/Pyro-Fe, ZnP@DHA, and ZnP@DHA/Pyro-Fe were 1.61 ± 0.10 g, 1.59 ± 0.12 g, 1.21 ± 0.16 g, and 0.55 ± 0.09 g, respectively (**Figure 3-12**d). These results confirmed the ability of Pyro-

Fe to enhance the antitumor efficacy of DHA. To ascertain ZnP@DHA/Pyro-induced ferroptosis as the major mechanism for antitumor efficacy, we immunostained tumor slides after treatments to probe SLC7A11, a glutamate-cystine exchanger, as one of the negative regulators for ferroptosis. The ZnP@DHA group showed some moderate green fluorescence, indicating moderate ferroptotic cell death. In comparison, ZnP@DHA/Pyro-Fe treatment showed completely depleted SLC7A11 with no green fluorescence signals, suggesting stronger ROS generation abrogated the negative regulator for ferroptosis (**Figure 3-13**).[43] The down-regulation of SLC7A11 might be mediated by the p53 pathway, which was activated by ROS to reduce the expression of SLC7A11.[44-45] Furthermore, no obvious body weight loss and abnormal histopathology were observed in major organs for all treated groups (**Figure 3-14** and **figure 3-15**) suggesting the lack of general toxicity for these treatments.

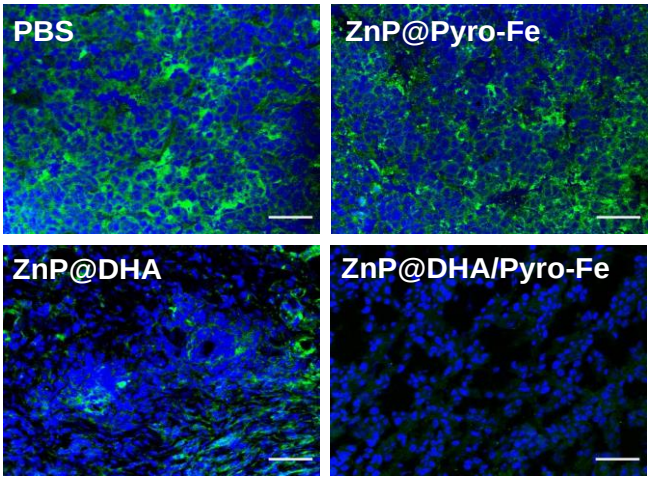

Figure 3-13. Immunofluorescence image of tumors after different treatments showing the down-regulation of SLC7A11. The nuclei were stained with DAPI (blue). Scale bar = 50 μm.

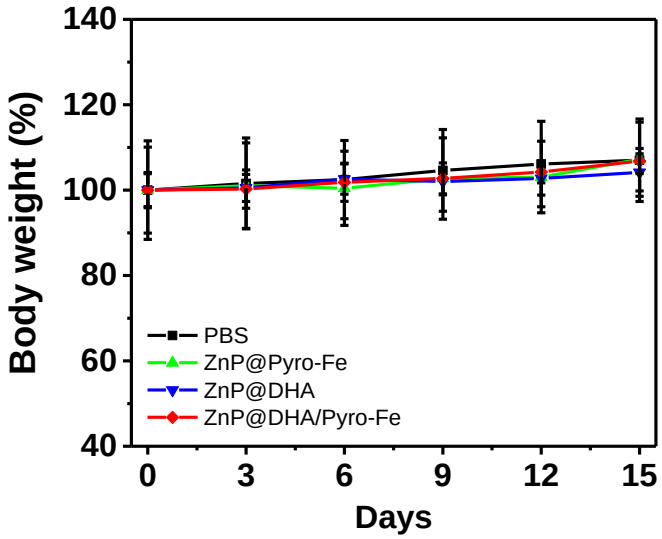

Figure 3-14. Body weight changes of MC38-bearing C57BL/6 mice after treatment with ZnP@DHA, ZnP@Pyro-Fe, or ZnP@DHA/Pyro-Fe.

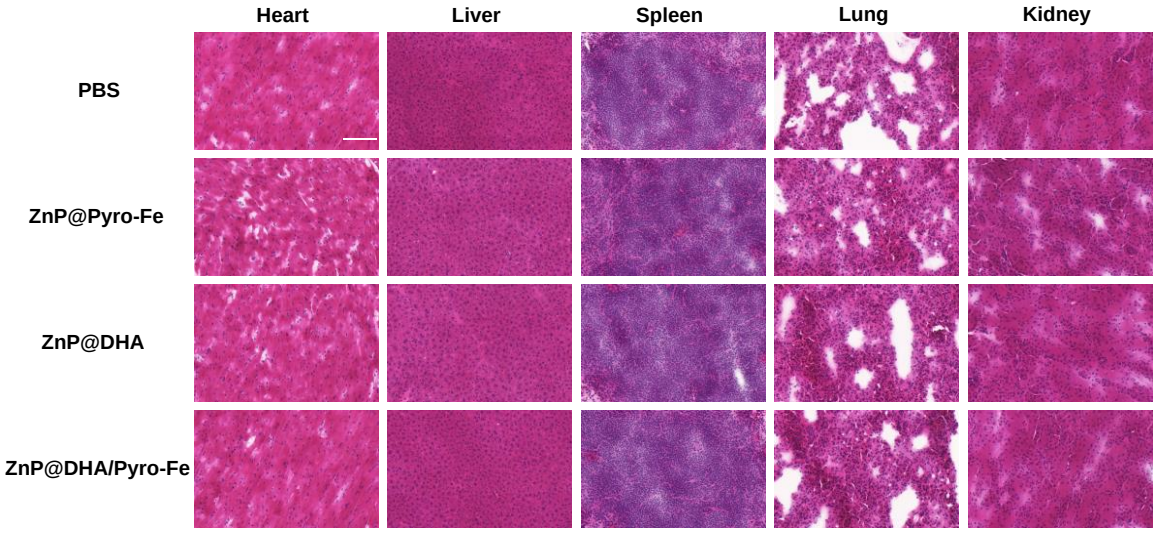

Figure 3-15. Major organ histologies of MC38-bearing C57BL/6 mice after treatment with ZnP@DHA, ZnP@Pyro-Fe or ZnP@DHA/Pyro-Fe. Scale bar = 100 μm.

3.2.7 Pyro-Fe potentiates immunostimulatory effects of DHA

Endoplasmic reticulum (ER) stress and ROS production are two essential components of the intracellular pathways that govern immunogenic cell death (ICD).[46-47] When occurring in parallel, they activate danger signaling pathways that traffic damage-associated molecular patterns (DAMPs) to the extracellular space. ICD releases tumor-associated antigens, DAMPs, and pro-inflammatory cytokines to facilitate the presentation of antigens to naïve T cells for an antigen-specific immune response against solid tumors.[48] Calreticulin (CRT), a chaperone protein abundant in the ER, is transported to the cell surface in response to ER stress as an indicator of ICD. Once on the cell surface, CRT serves as an "eat-me" signal, stimulating the engulfment of dying tumor cells and their apoptotic debris by macrophages and immature dendritic cells (DCs).[49-50] We demonstrated that DHA effectively induced immunogenic phenotypes of tumor cells, as evidenced by CRT exposure on the surface (**Figure 3-16** a). The translocation of CRT biomarker to tumor cell surface was confirmed by CLSM imaging (**Figure 3-16** b). In the presence of Pyro-Fe, CRT exposure was further enhanced as shown by the increases in CRT fluorescence intensity and CRT-positive cells.

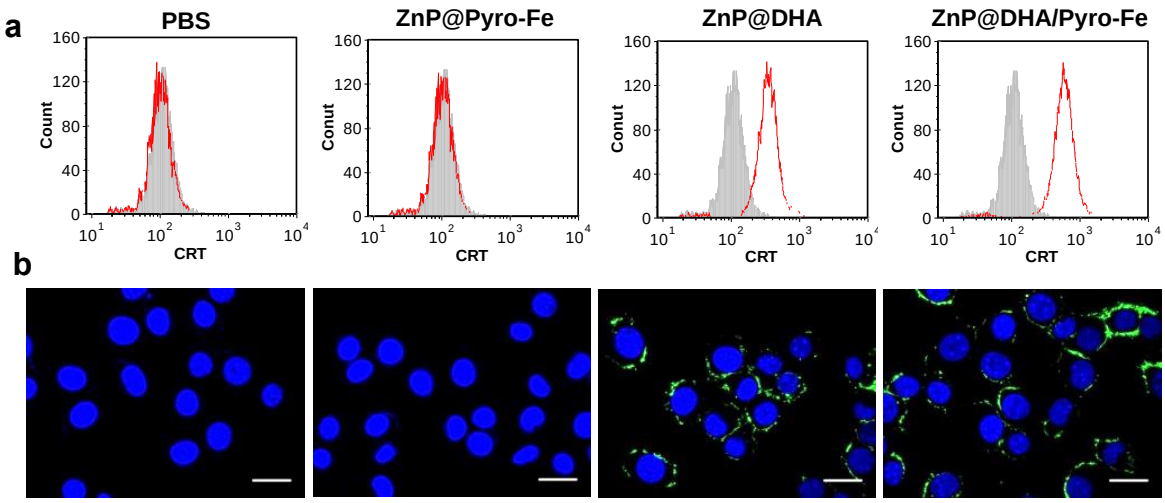

Figure 3-16. CRT exposure on the cell surface of CT26 cells after treatment, assessed by flow cytometry (a, red curve) and CLSM (b)

3.2.8 ZnP@DHA/Pyro-Fe sensitizes tumors to checkpoint blockade immunotherapy

In order to determine whether the antitumor immunity triggered by ZnP@DHA/Pyro-Fe could be harnessed for sensitizing tumors to checkpoint blockade therapy, we investigated the antitumor activity of the ZnP@DHA/Pyro-Fe plus anti-PD-L1 (α-PD-L1, Clone: 10F.9G2, Catalog No. BE0101, BioXCell) on both CT26 and MC38 colorectal cancers. Anti-PD-L1 showed a slight inhibitory effect on CT26 tumors at a dose of 75 μg/mouse, but no effect on MC38 tumors. Combination treatment with ZnP@DHA/Pyro-Fe and anti-PD-L1 significantly retarded the growth on both CT26 and MC38 tumors, leading to TGI values of 85% and 82.3%, respectively (**Figure 3-17** a-d).

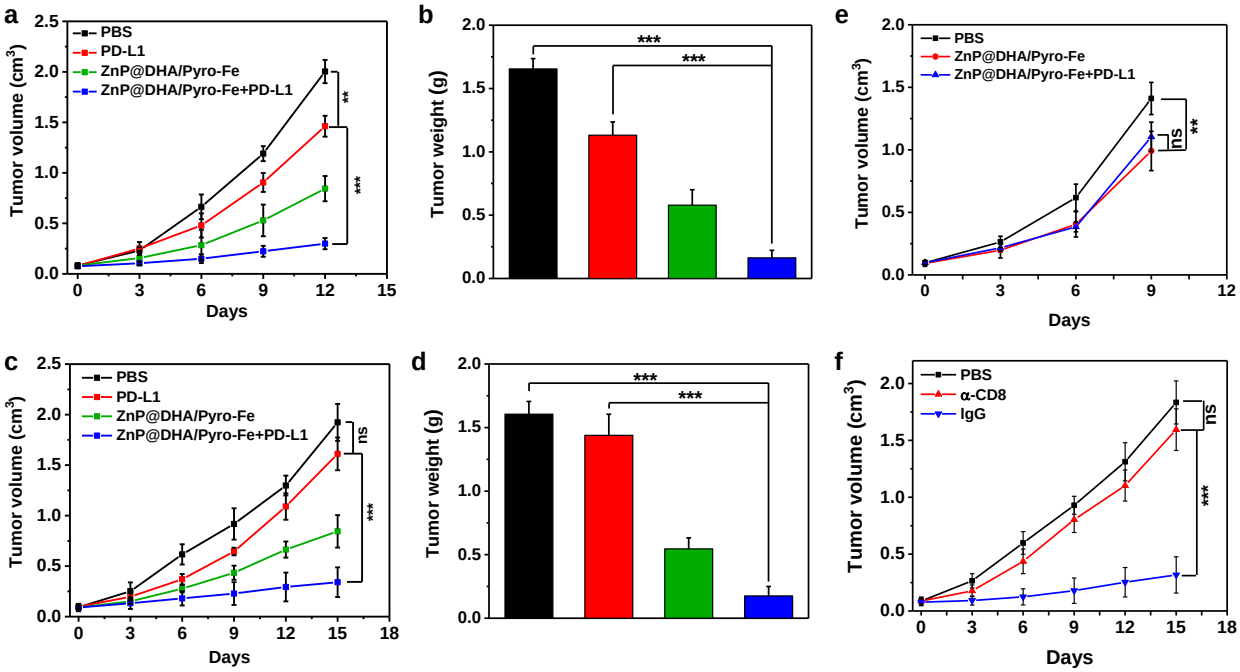

Figure 3-17. ZnP@DHA/Pyro-Fe treatment sensitizes tumors to α-PD-L1. (a-d) Growth curves (a,c) and final weights (b,d) of CT26 (a,b) and MC38 (c,d) tumors treated with ZnP@DHA/Pyro-Fe with or without α-PD-L1 (n = 6). (e,f) Therapeutic effect of the combination with α-PD-L1 on $Rag^{2-/-}$ mice (e) and on $CD8^{+}$ T cells depleted C57BL/6 mice (f) (n = 5).

To investigate the contribution of the immune response to anticancer efficacy, we evaluated the therapeutic effect of ZnP@DHA/Pyro-Fe plus α-PD-L1 on MC38 tumors implanted in immunodeficient $Rag^{2-/-}$ mice that lack mature lymphocytes, including both T and B cells. As expected, the effect of α-PD-L1 in the combination therapy was completely abrogated on $Rag^{2-/-}$ mice with ZnP@DHA/Pyro-Fe plus α-PD-L1 treatment showing similar antitumor efficacy as ZnP@DHA/Pyro-Fe treatment (**Figure 3-17** e). It is worth noting that the therapeutic effect of ZnP@DHA/Pyro-Fe against MC38 tumors in

immunodeficient $Rag^{2-/-}$ mice was inferior to that against MC38 tumors in immunocompetent C57BL/6 mice, underscoring the important role of the immune system on the therapeutic response. To further determine whether the antitumor effect depends on the host $CD8^+$ T cells, we depleted $CD8^+$ T cells on MC38 tumor-bearing mice *via* i.p. administration of an anti-CD8 monoclonal antibody. The therapeutic effect of ZnP@DHA/Pyro-Fe plus anti-PD-L1was significantly weakened with the depletion of $CD8^+$ T cells (**Figure 3-17** f). Taken together, these findings support our hypothesis that the involvement of the immune system is crucial to the therapeutic responses mediated by ZnP@DHA/Pyro-Fe.

3.3 Conclusion

We developed Zn-pyrophosphate core-shell nanoparticles for the co-delivery of chol-DHA and pyro-Fe to colorectal tumors in mouse models. Reduced pyro-Fe catalyzed the decomposition of DHA to produce ROS in an O_2-independent manner, causing apoptosis and ferroptosis of cancer cells. ZnP@DHA/pyro-Fe particles prolonged circulation half-lives of Chol-DHA and Pyro-Fe to increase their tumor uptake. The significant tumor accumulation of chol-DHA and pyro-Fe induced more ROS production and elicits significant tumor inhibition *in vivo*. Importantly, reduced pyro-Fe enhances the immunostimulatory effect of DHA. The combination of DHA and Pyro-Fe enhances intratumoral $CD8^+$ T cell infiltration and potentiates anti-PD-L1 immune checkpoint blockade in non-immunogenic colorectal tumors. With enhanced efficacy, low toxicity, and high selectivity, Zn@DHA/Pyro-Fe is a promising candidate for cancer treatment and combination therapy with immune checkpoint inhibitors.

3.4 Experimental

3.4.1 Synthesis of Pyro-Fe.

Pyro-lipid (a phospholipid conjugate of pyropheophorbide-a) was synthesized as previously described.[51] 50 mg pf pyro-lipid was dissolved in 10 mL THF and heated at 50^{o}C without nitrogen protection. $FeCl_2 \cdot (H_2O)_4$ (50 mg) was added to the solution in 3 batches in 1 hour. After the reaction turned green, the mixture was further heated for one additional hour. Solid impurities were removed by centrifugation and the solution was directly loaded onto an alumina column. The green product was eluted by 20% methanol in DCM. Yield: 38 mg (70%). ESI-MS: m/z=1089.5 ($[M+H]^+$). NMR spectra could not be obtained due to the paramagnetic nature of pyro-Fe. The oxidation state of Fe was characterized by UV-Vis spectrum (**Figure 3-18**).

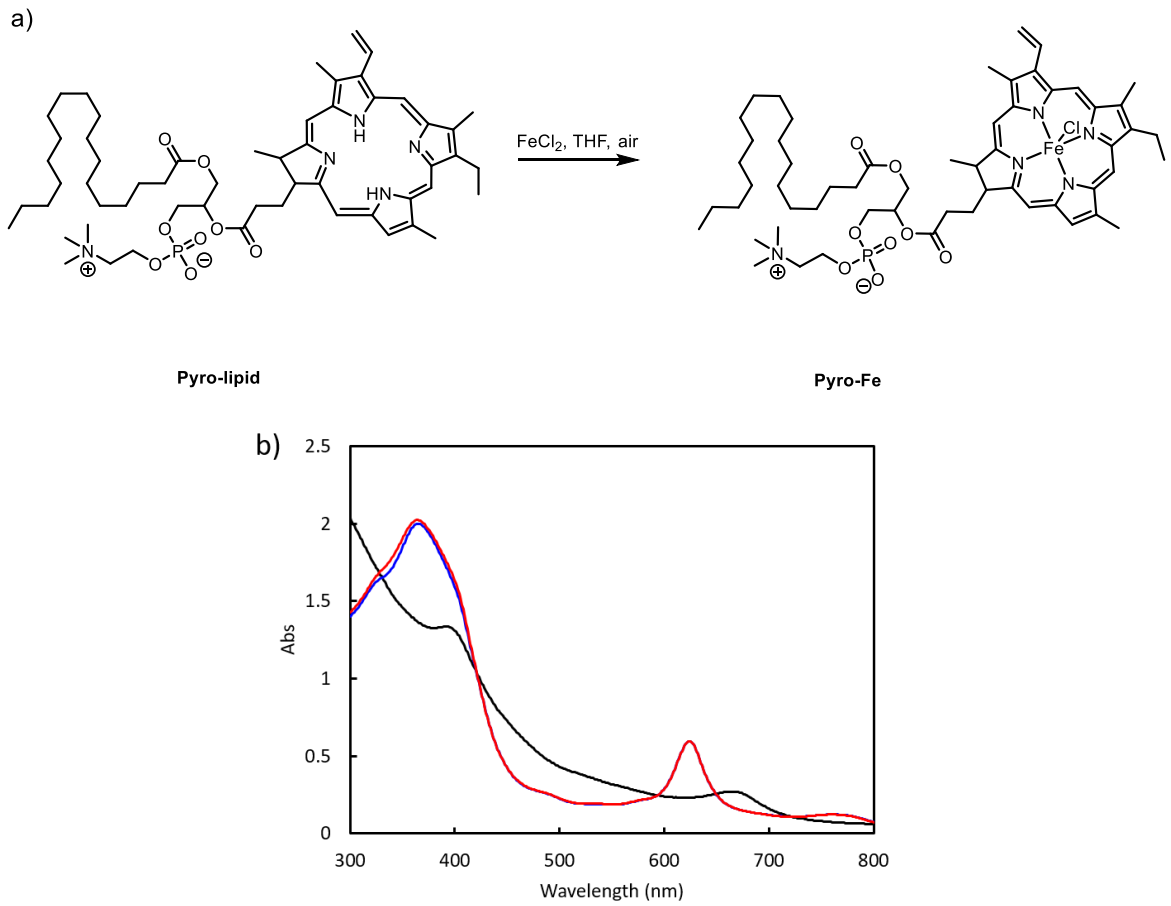

Figure 3-18. (a) Synthesis of Pyro-Fe. (b) UV-Vis spectra of as-synthesized Pyro-Fe (red), Pyro-Fe reduced by $NaBH_4$ (black), and air-oxidized Pyro-Fe (blue), indicating that as-synthesized Pyro-Fe has Fe^{III} oxidation state while $NaBH_4$-reduced Pyro-Fe has Fe^{II} oxidation state.

3.4.2 Synthesis of Zn-pyrophosphate (ZnP) Particles.

Two microemulsions were prepared by the addition of 0.2 mL $Na_4P_2O_7 \cdot 10H_2O$ (25 mg/mL in water) or 0.2 mL $Zn(NO_3)_2 \cdot 6H_2O$ (100 mg/mL in water) to 5 mL of cyclohexane containing 0.3 M TritonX-100 and 1.5 M hexanol. The microemulsions were stirred vigorously for 15 min at room temperature. 40 µL of the DOPA solution (200 mg/mL in

$CHCl_3$) was added to the $Na_4P_2O_7$ microemulsion, and the mixture was stirred 15 min to form a clear solution. Then, the $Zn(NO_3)_2$·microemulsion was added slowly to the $Na_4P_2O_7$ microemulsion with stirring, and the combined solution was allowed to react for 30 min at room temperature. Particles were precipitated by adding 20 mL of ethanol and centrifuging at 14000 g for 30 min. The resulting pellet was washed once with 50% EtOH/cyclohexane and twice with 50% EtOH/THF, then redispersed in THF. Particles were filtered through a 200 nm syringe filter.

3.4.3 Synthesis and characterization of ZnP@DHA, ZnP@Pyro-Fe and ZnP@DHA/Pyro-Fe.

ZnP@DHA, ZnP@Pyro-Fe, and ZnP@DHA/Pyro-Fe were prepared by adding a THF solution (80 μL) of DOPC, cholesterol, DSPE-PEG2k (2:1:1:1 in molar ratio), and ZnP particles to 500 μL of 30% (v/v) ethanol/water at 20 °C in the presence of Chol-DHA and/or Pyro-Fe, respectively. The mixture was stirred at 1,700 rpm for 1 min. THF and ethanol were completely evaporated, and the solution was allowed to cool to room temperature. The particle size and zeta potential were determined by dynamic light scattering (DLS) using a Zetasizer (Nano ZS, Malvern, UK). Transmission electron microscopy (Tecnai Spirit, FEI, USA) was used to observe the morphology of nanoparticles. To determine drug loading, nanoparticles were centrifuged at 13,000 rpm for 30 min, the supernatant was removed, and the nanoparticles were resuspended in THF, which dissolves the lipid layer to release Chol-DHA and Pyro-Fe. The amounts of Chol-DHA and Pryo-Fe in the nanoparticle suspension were then determined by liquid chromatography-mass spectrometry (6540 Q-Tof MS-MS, Agilent, USA) and inductively

coupled plasma-mass spectrometry (Masshunter 7700, Agilent, USA), respectively. To test colloidal stability, nanoparticles diluted in phosphate buffered saline containing 5 mg/mL BSA were incubated at 37 ºC, and the changes in particle size and PDI over time were determined by DLS.

3.4.4 ROS generation in solution.

ZnP@DHA, ZnP@Pyro-Fe, or ZnP@DHA/Pyro-Fe with or without 5 mM cysteine was dispersed in 0.5% Triton X-100 that contains 10 μM H_2-DCFDA (Thermo Fisher Scientific, USA). The ROS generation in the presence or absence of O_2 was investigated by determining the change of DCF fluorescence over time.

3.4.5 Cell EM.

CT26 cells were treated with ZnP@DHA, ZnP@Pyro-Fe or ZnP@DHA/Pyro-Fe at a dose of 10 μM Pyro-Fe or/and 10 μM DHA for 24 h. Cells were then collected and fixed with OsO_4 staining solution for observation under Tecnai Spirit TEM.

3.4.6 Cell cycle assay.

For cell cycle assay, treated CT26 cells as described above were collected, washed twice with ice-cold PBS, fixed with 70% ethanol at 4 ºC overnight and treated with RNase A for 45 min, followed by PI staining for 30 min. The alteration of cell cycle was analyzed by flow cytometry.

3.4.7 Intracellular iron uptake.

CT26 cells seeded in 6-well plates (5×10^4 cells/well) were treated with ZnP@Pyro-Fe, ZnP@DHA, or ZnP@DHA/Pyro-Fe at a concentration of 10 μM Pyro-Fe or/and 10 μM DHA for 24 h, then harvested, washed twice with ice-cold PBS, dried, and digested with concentrated nitrate acid. The Fe content was determined by ICP-MS.

3.4.8 *In vitro* cytotoxicity.

CT26 cells or MC38 cells were seeded in 96-well plates at a density of 2×10^3 cells per well and allowed to adhere for 24 h. Cells were then treated with different concentrations of ZnP@Pyro-Fe, ZnP@DHA, or ZnP@DHA/Pyro-Fe at 1:1 molar ratio of DHA to Pyro-Fe for another 72 h. Cell viability was detected by MTS assay (Promega, USA) according to the manufacturer's instructions.

3.4.9 Intracellular ROS generation.

CT26 cells were treated with ZnP@Pyro-Fe, ZnP@DHA, or ZnP@DHA/Pyro-Fe at a concentration of 10 μM Pyro-Fe or/and 10 μM DHA for 24 h, then incubated with 10 μM H_2-DCFDA (Thermo Fisher) for another 1 h. The cells were collected, washed twice with ice-cold PBS, and analyzed by flow cytometry.

3.4.10 DNA double-strand break.

After treatment with ZnP@Pyro-Fe, ZnP@DHA, or ZnP@DHA/Pyro-Fe at a concentration of 10 μM Pyro-Fe or/and 10 μM DHA for 24 h, CT26 cells were fixed with 4% paraformaldehyde at room temperature for 10 min, permeabilized with 0.1% Triton X-100 at room temperature for 10 min, blocked with 2% BSA at room temperature for 1 h, and stained with FCS DNA damage kit (Invitrogen) for the oxidative DNA damage detection by γ-H2AX foci. After staining with DAPI for another 10 min, the cells were washed twice with PBS and observed under CLSM (Olympus, FV1000).

3.4.11 CRT exposure analysis.

CT26 cells seeded in 6 well plates (2×10^5 cells/well) were cultured with ZnP@Pyro-Fe, ZnP@DHA, or ZnP@DHA/Pyro-Fe at a dose of 10 μM Pyro-Fe and/or 10 μM DHA for 24 h. The treated cells were collected, incubated with Alexa Fluor 488-CRT antibody (Enzo Life Sciences, USA) for 2 h, stained with PI, and analyzed by flow cytometer to determine CRT exposure. The fluorescence intensity of stained cells was gated on PI^- cells. For surface detection of CRT, CT26 cells were seeded on 10 mm^2 glass coverslips placed in 6-well plates at a density of 2×10^5 cells per well. After treatment, cells were washed with PBS three times, incubated with Alexa Fluor 488-CRT antibody for 2 h, stained with DAPI, and observed under CLSM using 405 nm and 488 nm lasers for nuclei and CRT expression, respectively, on the cell membrane.

3.4.12 Pharmacokinetic (PK) and biodistribution (BD) analysis.

ZnP@DHA/Pyro-Fe doped with 20% pyrolipid were used for analysis. Particles were dosed intravenously to rats for pK and to CT26 bearing mice for BD. Blood samples were collected at 5 min, 0.5 h, 1 h, 3 h, 5 h, 8 h, and 24 h from rat and organ samples were collected 24 h post injection form mice. Blood samples were centrifuged at 5000 rpm for 5 min to obtain plasma and then measured by UV-Vis. Organ samples were homogenized with 0.5% Triton X-100 and then measured by IVIS for its fluorescence.

3.4.13 *In vivo* antitumor efficacy.

1×10^6 cells CT26 cells were subcutaneously injected into the right flank region of 6-week old BALB/c mice. 1×10^6 cells MC38 cells were subcutaneously injected into the right flank region of 6-week old C57Bl/6 wild-type or $Rag^{2-/-}$ mice. 12 days later, mice were intraperitoneally (i.p.) injected with ZnP@DHA/Pyro-Fe particles or controls with equivalent doses of 10 mg/kg DHA, 1.96 mg/kg Fe, and/or 75 μg PD-L1 antibody once every 3 days for 3 doses for CT26 tumors and 4 doses for MC38 tumors. To evaluate the therapeutic efficacy, tumor growth and body weight evolution were monitored. Tumor size was measured with a digital caliper every day. Tumor volumes were calculated as follows: $(\text{width}^2 \times \text{length})/2$. All mice were euthanized when the tumor size of the control group exceeded 2 cm^3 and the excised tumors were photographed and weighed. The tumors were embedded in optimal cutting temperature medium, sectioned at 5 mm thickness and subjected to haematoxylin and eosin (H&E) stain for histopathological analysis, SLC7A11 (Cell Signaling, USA) for ferroptosis, and TUNEL (Invitrogen, USA) assay for apoptosis. Hearts, livers, lungs, spleens, and kidneys were also excised and sectioned at 5 mm

thickness, stained with H&E, and observed under a light microscope (Pannoramic Scan Whole Slide Scanner, Perkin Elmer, USA).

3.5 References

1. Yang, W. S.; Stockwell, B. R., Ferroptosis: death by lipid peroxidation. *Trends in cell biology* **2016,** *26* (3), 165-176.

2. Dixon, S. J.; Lemberg, K. M.; Lamprecht, M. R.; Skouta, R.; Zaitsev, E. M.; Gleason, C. E.; Patel, D. N.; Bauer, A. J.; Cantley, A. M.; Yang, W. S., Ferroptosis: an iron-dependent form of nonapoptotic cell death. *Cell* **2012,** *149* (5), 1060-1072.

3. Dolma, S.; Lessnick, S. L.; Hahn, W. C.; Stockwell, B. R., Identification of genotype-selective antitumor agents using synthetic lethal chemical screening in engineered human tumor cells. *Cancer cell* **2003,** *3* (3), 285-296.

4. Yang, W. S.; Stockwell, B. R., Synthetic lethal screening identifies compounds activating iron-dependent, nonapoptotic cell death in oncogenic-RAS-harboring cancer cells. *Chemistry & biology* **2008,** *15* (3), 234-245.

5. Yagoda, N.; von Rechenberg, M.; Zaganjor, E.; Bauer, A. J.; Yang, W. S.; Fridman, D. J.; Wolpaw, A. J.; Smukste, I.; Peltier, J. M.; Boniface, J. J., RAS–RAF–MEK-dependent oxidative cell death involving voltage-dependent anion channels. *Nature* **2007,** *447* (7146), 865-869.

6. Yang, W. S.; Kim, K. J.; Gaschler, M. M.; Patel, M.; Shchepinov, M. S.; Stockwell, B. R., Peroxidation of polyunsaturated fatty acids by lipoxygenases drives ferroptosis. *Proceedings of the National Academy of Sciences* **2016,** *113* (34), E4966-E4975.

7. Kagan, V. E.; Mao, G.; Qu, F.; Angeli, J. P. F.; Doll, S.; St Croix, C.; Dar, H. H.; Liu, B.; Tyurin, V. A.; Ritov, V. B., Oxidized arachidonic and adrenic PEs navigate cells to ferroptosis. *Nature chemical biology* **2017,** *13* (1), 81-90.

8. Bannai, S.; Tsukeda, H.; Okumura, H., Effect of antioxidants on cultured human diploid fibroblasts exposed to cystine-free medium. *Biochemical and Biophysical Research Communications* **1977,** *74* (4), 1582-1588.

9. Sato, H.; Tamba, M.; Ishii, T.; Bannai, S., Cloning and expression of a plasma membrane cystine/glutamate exchange transporter composed of two distinct proteins. *Journal of Biological Chemistry* **1999,** *274* (17), 11455-11458.

10. Ursini, F.; Maiorino, M.; Gregolin, C., The selenoenzyme phospholipid hydroperoxide glutathione peroxidase. *Biochimica et Biophysica Acta (BBA)-General Subjects* **1985,** *839* (1), 62-70.

11. Seiler, A.; Schneider, M.; Förster, H.; Roth, S.; Wirth, E. K.; Culmsee, C.; Plesnila, N.; Kremmer, E.; Rådmark, O.; Wurst, W., Glutathione peroxidase 4 senses and translates oxidative stress into 12/15-lipoxygenase dependent-and AIF-mediated cell death. *Cell metabolism* **2008,** *8* (3), 237-248.

12. Warner, G. J.; Berry, M. J.; Moustafa, M. E.; Carlson, B. A.; Hatfield, D. L.; Faust, J. R., Inhibition of selenoprotein synthesis by selenocysteine tRNA [Ser] Sec lacking isopentenyladenosine. *Journal of Biological Chemistry* **2000,** *275* (36), 28110-28119.

13. Dixon, S. J.; Patel, D. N.; Welsch, M.; Skouta, R.; Lee, E. D.; Hayano, M.; Thomas, A. G.; Gleason, C. E.; Tatonetti, N. P.; Slusher, B. S., Pharmacological inhibition of cystine–glutamate exchange induces endoplasmic reticulum stress and ferroptosis. *Elife* **2014,** *3*, e02523.

14. Yang, W. S.; SriRamaratnam, R.; Welsch, M. E.; Shimada, K.; Skouta, R.; Viswanathan, V. S.; Cheah, J. H.; Clemons, P. A.; Shamji, A. F.; Clish, C. B., Regulation of ferroptotic cancer cell death by GPX4. *Cell* **2014,** *156* (1-2), 317-331.

15. Liu, M.; Liu, B.; Liu, Q.; Du, K.; Wang, Z.; He, N., Nanomaterial-induced ferroptosis for cancer specific therapy. *Coordination Chemistry Reviews* **2019,** *382*, 160-180.

16. Shen, Z.; Song, J.; Yung, B. C.; Zhou, Z.; Wu, A.; Chen, X., Emerging strategies of cancer therapy based on ferroptosis. *Advanced Materials* **2018,** *30* (12), 1704007.

17. Shen, Z.; Liu, T.; Li, Y.; Lau, J.; Yang, Z.; Fan, W.; Zhou, Z.; Shi, C.; Ke, C.; Bregadze, V. I., Fenton-reaction-acceleratable magnetic nanoparticles for ferroptosis therapy of orthotopic brain tumors. *ACS nano* **2018,** *12* (11), 11355-11365.

18. Kono, H.; Rock, K. L., How dying cells alert the immune system to danger. *Nature Reviews Immunology* **2008,** *8* (4), 279-289.

19. Linkermann, A.; Skouta, R.; Himmerkus, N.; Mulay, S. R.; Dewitz, C.; De Zen, F.; Prokai, A.; Zuchtriegel, G.; Krombach, F.; Welz, P.-S., Synchronized renal tubular cell death involves ferroptosis. *Proceedings of the National Academy of Sciences* **2014,** *111* (47), 16836-16841.

20. Tang, R.; Xu, J.; Zhang, B.; Liu, J.; Liang, C.; Hua, J.; Meng, Q.; Yu, X.; Shi, S., Ferroptosis, necroptosis, and pyroptosis in anticancer immunity. *Journal of Hematology & Oncology* **2020,** *13* (1), 1-18.

21. Wang, W.; Green, M.; Choi, J. E.; Gijón, M.; Kennedy, P. D.; Johnson, J. K.; Liao, P.; Lang, X.; Kryczek, I.; Sell, A., CD8+ T cells regulate tumour ferroptosis during cancer immunotherapy. *Nature* **2019,** *569* (7755), 270-274.

22. Wen, Q.; Liu, J.; Kang, R.; Zhou, B.; Tang, D., The release and activity of HMGB1 in ferroptosis. *Biochemical and biophysical research communications* **2019,** *510* (2), 278-283.

23. Kim, S. E.; Zhang, L.; Ma, K.; Riegman, M.; Chen, F.; Ingold, I.; Conrad, M.; Turker, M. Z.; Gao, M.; Jiang, X., Ultrasmall nanoparticles induce ferroptosis in nutrient-deprived cancer cells and suppress tumour growth. *Nature nanotechnology* **2016,** *11* (11), 977.

24. Yaghoubi, N.; Soltani, A.; Ghazvini, K.; Hassanian, S. M.; Hashemy, S. I., PD-1/PD-L1 blockade as a novel treatment for colorectal cancer. *Biomedicine & Pharmacotherapy* **2019,** *110*, 312-318.

25. Zou, W.; Wolchok, J. D.; Chen, L., PD-L1 (B7-H1) and PD-1 pathway blockade for cancer therapy: Mechanisms, response biomarkers, and combinations. *Science translational medicine* **2016,** *8* (328), 328rv4-328rv4.

26. Teng, F.; Meng, X.; Kong, L.; Yu, J., Progress and challenges of predictive biomarkers of anti PD-1/PD-L1 immunotherapy: a systematic review. *Cancer letters* **2018,** *414*, 166-173.

27. Robert, A.; Coppel, Y.; Meunier, B., Alkylation of heme by the antimalarial drug artemisinin. *Chemical communications* **2002,** (5), 414-415.

28. Hong, Y.-L.; Yang, Y.-Z.; Meshnick, S. R., The interaction of artemisinin with malarial hemozoin. *Molecular and biochemical parasitology* **1994,** *63* (1), 121-128.

29. Elhassanny, A. E. M.; Soliman, E.; Marie, M.; McGuire, P.; Gul, W.; ElSohly, M.; Van Dross, R., Heme-dependent ER stress apoptosis: A mechanism for the selective toxicity of the dihydroartemisinin, NSC735847, in colorectal cancer cells. *Frontiers in oncology* **2020,** *10*, 965.

30. Zhang, S.; Gerhard, G. S., Heme mediates cytotoxicity from artemisinin and serves as a general anti-proliferation target. *PloS one* **2009,** *4* (10), e7472.

31. Haynes, R. K.; Chan, W. C.; Lung, C. M.; Uhlemann, A. C.; Eckstein, U.; Taramelli, D.; Parapini, S.; Monti, D.; Krishna, S., The Fe2+-mediated decomposition, PfATP6 binding, and antimalarial activities of artemisone and other artemisinins: the unlikelihood of C-centered radicals as bioactive intermediates. *ChemMedChem: Chemistry Enabling Drug Discovery* **2007,** *2* (10), 1480-1497.

32. Morris, C. A.; Duparc, S.; Borghini-Fuhrer, I.; Jung, D.; Shin, C.-S.; Fleckenstein, L., Review of the clinical pharmacokinetics of artesunate and its active metabolite dihydroartemisinin following intravenous, intramuscular, oral or rectal administration. *Malaria journal* **2011,** *10* (1), 263.

33. Fujita, T.; Felix, K.; Pinkaew, D.; Hutadilok-Towatana, N.; Liu, Z.; Fujise, K., Human fortilin is a molecular target of dihydroartemisinin. *FEBS letters* **2008,** *582* (7), 1055-1060.

34. Ying-Zi, Y.; Little, B.; Meshnick, S. R., Alkylation of proteins by artemisinin: effects of heme, pH, and drug structure. *Biochemical pharmacology* **1994,** *48* (3), 569-573.

35. Zhou, Y.; Li, W.; Xiao, Y., Profiling of multiple targets of artemisinin activated by hemin in cancer cell proteome. *ACS chemical biology* **2016,** *11* (4), 882-888.

36. Lin, R.; Zhang, Z.; Chen, L.; Zhou, Y.; Zou, P.; Feng, C.; Wang, L.; Liang, G., Dihydroartemisinin (DHA) induces ferroptosis and causes cell cycle arrest in head and neck carcinoma cells. *Cancer letters* **2016,** *381* (1), 165-175.

37. Chen, G.-Q.; Benthani, F. A.; Wu, J.; Liang, D.; Bian, Z.-X.; Jiang, X., Artemisinin compounds sensitize cancer cells to ferroptosis by regulating iron homeostasis. *Cell Death & Differentiation* **2020,** *27* (1), 242-254.

38. Wang, L.; Zhang, Z.; Li, M.; Wang, F.; Jia, Y.; Zhang, F.; Shao, J.; Chen, A.; Zheng, S., P53-dependent induction of ferroptosis is required for artemether to alleviate carbon tetrachloride-induced liver fibrosis and hepatic stellate cell activation. *IUBMB life* **2019,** *71* (1), 45-56.

39. West, A. P.; Shadel, G. S.; Ghosh, S., Mitochondria in innate immune responses. *Nature Reviews Immunology* **2011,** *11* (6), 389.

40. Yang, Y.; Bazhin, A. V.; Werner, J.; Karakhanova, S., Reactive oxygen species in the immune system. *International reviews of immunology* **2013,** *32* (3), 249-270.

41. Kinner, A.; Wu, W.; Staudt, C.; Iliakis, G., γ-H2AX in recognition and signaling of DNA double-strand breaks in the context of chromatin. *Nucleic acids research* **2008,** *36* (17), 5678-5694.

42. Stockwell, B. R.; Angeli, J. P. F.; Bayir, H.; Bush, A. I.; Conrad, M.; Dixon, S. J.; Fulda, S.; Gascón, S.; Hatzios, S. K.; Kagan, V. E., Ferroptosis: a regulated cell death nexus linking metabolism, redox biology, and disease. *Cell* **2017,** *171* (2), 273-285.

43. Yi, R.; Wang, H.; Deng, C.; Wang, X.; Yao, L.; Niu, W.; Fei, M.; Zhaba, W., Dihydroartemisinin initiates ferroptosis in glioblastoma through GPX4 inhibition. *Bioscience Reports* **2020**.

44. Jiang, L.; Kon, N.; Li, T.; Wang, S.-J.; Su, T.; Hibshoosh, H.; Baer, R.; Gu, W., Ferroptosis as a p53-mediated activity during tumour suppression. *Nature* **2015,** *520* (7545), 57-62.

45. Liu, D. S.; Duong, C. P.; Haupt, S.; Montgomery, K. G.; House, C. M.; Azar, W. J.; Pearson, H. B.; Fisher, O. M.; Read, M.; Guerra, G. R., Inhibiting the system x

C−/glutathione axis selectively targets cancers with mutant-p53 accumulation. *Nature communications* **2017,** *8*, 14844.

46. Krysko, D. V.; Garg, A. D.; Kaczmarek, A.; Krysko, O.; Agostinis, P.; Vandenabeele, P., Immunogenic cell death and DAMPs in cancer therapy. *Nature Reviews Cancer* **2012,** *12* (12), 860-875.

47. Green, D. R.; Ferguson, T.; Zitvogel, L.; Kroemer, G., Immunogenic and tolerogenic cell death. *Nature Reviews Immunology* **2009,** *9* (5), 353-363.

48. Kroemer, G.; Galluzzi, L.; Kepp, O.; Zitvogel, L., Immunogenic cell death in cancer therapy. *Annual review of immunology* **2013,** *31*, 51-72.

49. Obeid, M.; Tesniere, A.; Ghiringhelli, F.; Fimia, G. M.; Apetoh, L.; Perfettini, J.-L.; Castedo, M.; Mignot, G.; Panaretakis, T.; Casares, N., Calreticulin exposure dictates the immunogenicity of cancer cell death. *Nature medicine* **2007,** *13* (1), 54-61.

50. Chao, M. P.; Jaiswal, S.; Weissman-Tsukamoto, R.; Alizadeh, A. A.; Gentles, A. J.; Volkmer, J.; Weiskopf, K.; Willingham, S. B.; Raveh, T.; Park, C. Y., Calreticulin is the dominant pro-phagocytic signal on multiple human cancers and is counterbalanced by CD47. *Science translational medicine* **2010,** *2* (63), 63ra94-63ra94.

51. Duan, X.; Chan, C.; Guo, N.; Han, W.; Weichselbaum, R. R.; Lin, W., Photodynamic therapy mediated by nontoxic core–shell nanoparticles synergizes with immune checkpoint blockade to elicit antitumor immunity and antimetastatic effect on breast cancer. *Journal of the American Chemical Society* **2016,** *138* (51), 16686-16695.

Chapter 4. Nanoscale Coordination Polymer Co-delivers Cisplatin and Paclitaxel for Effective Treatment of Advanced and Metastatic Cancers

4.1 Introduction

Cisplatin (CisPt) alone or in combination with other anticancer drugs is widely used to treat a variety of cancers. Its broad-spectrum and high potency make it a gold standard in treating multiple types of solid tumors, including ovarian cancer, bladder cancer, head and neck cancer, small cell lung cancer, and non-small cell lung cancer.[1] The use of cisplatin is limited by several toxicities such as nephrotoxicity,[2] ototoxicity[3, 4], and neurotoxicity.[5] Acute renal failure developed in about 28-36% patients at 50-100 mg/m^2 dosage level[6] and most patients with renal dysfunction never recover.[7] 7-90% of patients experienced ototoxicity in different studies[8, 9] and hearing loss was frequently irreversible.[10] Neurotoxicity also occurs in some patients when the cumulative dose of cisplatin is over 400 mg/m^2.[11] Moreover, pharmacokinetic properties of free cisplatin are not optimal. In dog studies, platinum accumulated in kidney and liver 1 hour after i.v. administration, while only less than 20% platinum remained in plasma.[12] 60% of injected cisplatin is cleared through urine within 4 hours.[12] Efforts have been made to improve pharmacokinetics, efficacy, and reduce toxicity. Oxaliplatin, carboplatin, nedaplatin, and some other platinum-based compounds were developed; these partially addressed the problems faced by cisplatin, but they caused different toxicity profiles and, in some cases, partially changed the mechanism of action.[1]

Paclitaxel (PTX) is another broad-spectrum anticancer drug commonly used in the treatment of ovarian cancer, breast cancer, lung cancer, and others.[13] Unlike platinum-based drugs, PTX binds with microtubule rather than nucleic acids.[14] PTX promotes

microtubule formation and provides abnormal stability of microtubule, disturbing dynamic reorganization of the microtubule network.[15, 16] The difference in mechanism makes PTX plus cisplatin a frequently used combination clinically to avoid single drug resistance and address other issues like severe toxicity.[17, 18] Other drugs are sometimes added to this combination to further enhance treatment efficacy.[19, 20]

PTX is a highly hydrophobic molecule, which makes it difficult to be infused into patients. Some early efforts to solve this problem include introducing hydrophilic groups like carboxylic acids[21] or PEG[22] to the molecule. These modified compounds showed *in vitro* toxicity but were not used in clinical practice. Three strategies were frequently used in the clinic or tested in clinical trials: solubilizer, micelle/liposome carriers, and albumin carrier. Cremophor is widely used as a solubilizer of hydrophobic drugs and showed the ability to deliver PTX. Other solubilizer systems include ethanol and tween-80 were also used.[23] Most solubilizers are amphiphilic surfactants that can bind with hydrophobic PTX and provide interactions with aqueous environment, stabilizing PTX in water solutions. Solubilizer systems often cause toxicity issues[24] like hypersensitivity reactions, hyperlipidaemia, abnormal lipoprotein patterns, aggregation of erythrocytes, and peripheral neuropathy.[25] Sometimes PTX may precipitate once injected and diluted by the blood during circulation.[26] Micelle[27, 28] and liposome[29, 30] are well-studied nanoparticle platforms in delivering PTX and both strategies showed the ability to encapsulate PTX and avoid vehicle toxicity and drug precipitation, but they still suffer from rapid drug leakage and poor stability in circulation and storage.[27-31] Binding with plasma proteins can help to reduce the risk of precipitation and improve circulation. Albumin-bound PTX is currently marketed under the name Abraxane®.[32] It significantly stabilized PTX in aqueous

environments but showed little improvements in other aspects like circulation half-life.[31, 33]

Biomolecules and some structures that exist in bloodstream showed much better circulation profile: antibody drug pembrolizumab has a circulation half-life of 27-28 days in human bodies,[34] the half-life of low-density lipoprotein (LDL) in human bodies was measured to be around 4 days[35], and human red blood cells have a lifespan of about 115 days[36]. Long-circulating species existing in bloodstream and similar artificial structures were studied as drug carriers to improve pharmacokinetic properties. In the early 1970s, researchers noticed that some lipophilic drugs and hormones showed a better circulation profile by binding with lipoproteins in serum.[37, 38] After detailed research over 20 years, the formation, circulation, and function of lipoproteins became clear.[39] Lipoproteins are circulating in the form of nanoparticles with a size of 5-100 nm. Cholesterols and triglycerides absorbed by intestine are transferred to liver in the form of chylomicrons, then secreted by liver as very low-density lipoprotein (VLDL) which contains cholesterols, cholesterol esters and triglycerides. VLDL particles lose triglycerides in circulation with the help of lipoprotein lipase (LPL) and become cholesterol-rich and dense intermediate-density lipoprotein (IDL). IDL further interacts with high-density lipoprotein (HDL) which is responsible for cholesterol and phospholipid recycling to form 20 nm-sized low-density lipoprotein (LDL) containing a high percentage of cholesterol esters and pure apolipoprotein B-100 (Apo B-100). Finally, LDL can be either recycled by liver or uptaken by other organs scavenger cells to deliver cholesterol.[40-43]

Being a major pathway of cholesterol delivery, LDL is highly demanded in rapidly dividing cancer cells, making it an ideal vehicle for anticancer drugs.[44] Most reports that engineered

LDL as a drug carrier share similar protocols. LDL particles were isolated and purified from serum and extracted with an organic solvent to remove lipids, then lipophilic molecules or cholesterol conjugated compounds together with some extra lipids were loaded to delipidized LDL to reconstitute LDL-like particles.[45-48] Drug loaded LDLs showed improved pharmacokinetic profiles and anticancer efficacies but limited by the source of LDL and complicated protocol.

As a versatile nanoparticle platform, NCP provides a potential solution for co-delivering hydrophilic cisplatin and hydrophobic PTX. Being protected in the lipid bilayer of NCP, PTX can be stabilized in an aqueous solution without precipitation. The proper size of the particle can also avoid fast renal clearance of cisplatin and passively target both drugs to tumors by the EPR effect. Further studies revealed interactions happened between NCP particles and native LDLs during circulation, allowing NCP particles to take advantage of tumor-targeting features of LDL. The NCP will also have different pharmacokinetic profiles for both drugs, which may reduce their systemic toxicity.

4.2 Results

4.2.1 Synthesis and characterization of CisPt/PTX

Prodrugs of CisPt and PTX were synthesized using similar methods as OxPt and DHA in Chapter 2 (**Figure 4-1**). The NCP particles were synthesized in similar two-step protocols. In brief, cisplatin prodrug neutralized by NaOH solution was suspended in a mixture of hexanol and cyclohexane with triton X-100 as a surfactant to stabilize the microemulsion,

$Zn(NO_3)_2$ solution was suspended in a microemulsion form in the same solvent mixture. Two microemulsions were mixed and monosodium salt of 1,2-dioleoyl-

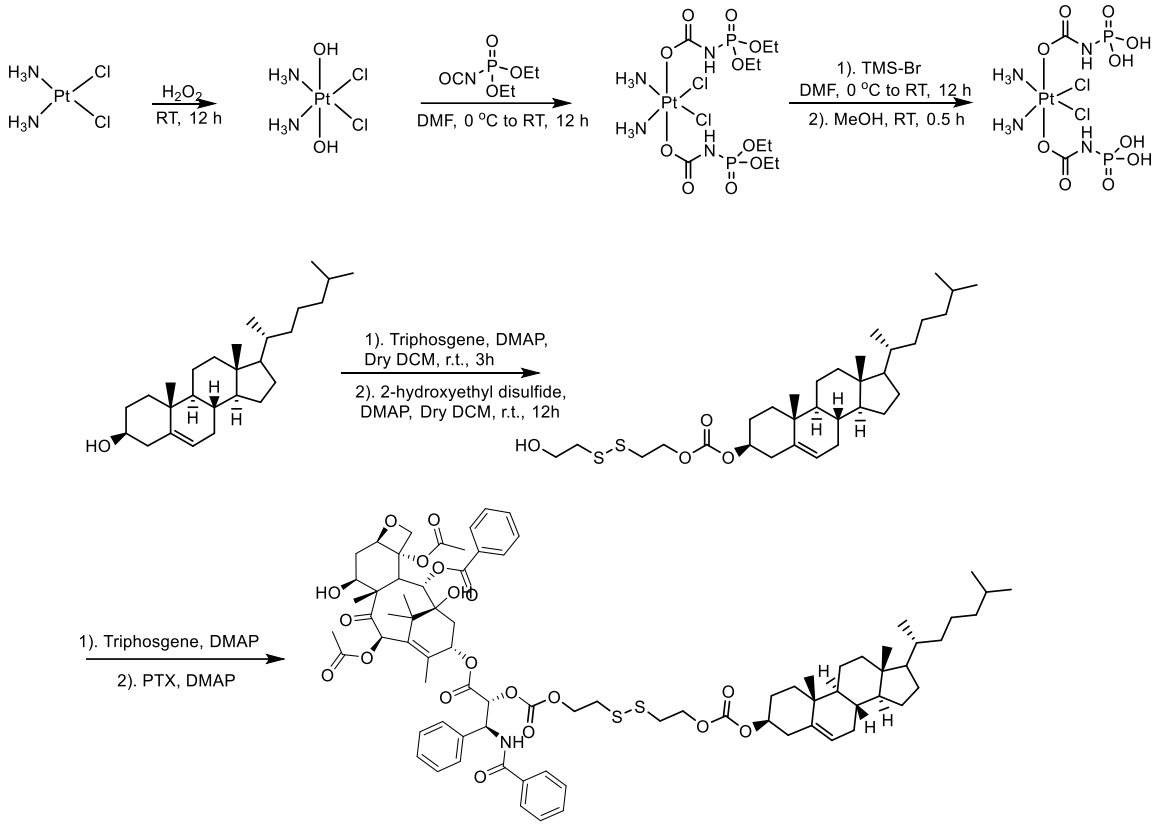

Figure 4-1. Synthesis of CisPt and PTX prodrugs.

sn-glycero-3-phosphate (DOPA) was used to stop aggregation and yield a spherical, monodispersed solid particle core containing Zn^{2+} cross-linked CisPt prodrug capped by DOPA. The DOPA-capped particle was further coated with a mixture of DOPC, cholesterol, DSPE-PEG, and chol-PTX at an 8:8:4:1 molar ratio to afford the core-shell nanoparticles CisPt/PTX (**Figure 4-2** a). Particles with CisPt (CisPtNCP) or chol-PTX (Zn/PTX) only were also prepared as control particles. Fluorescently labeled NCPs with chol-pyro in lipid bilayer described in Chapter 2 was used for mechanistic studies.

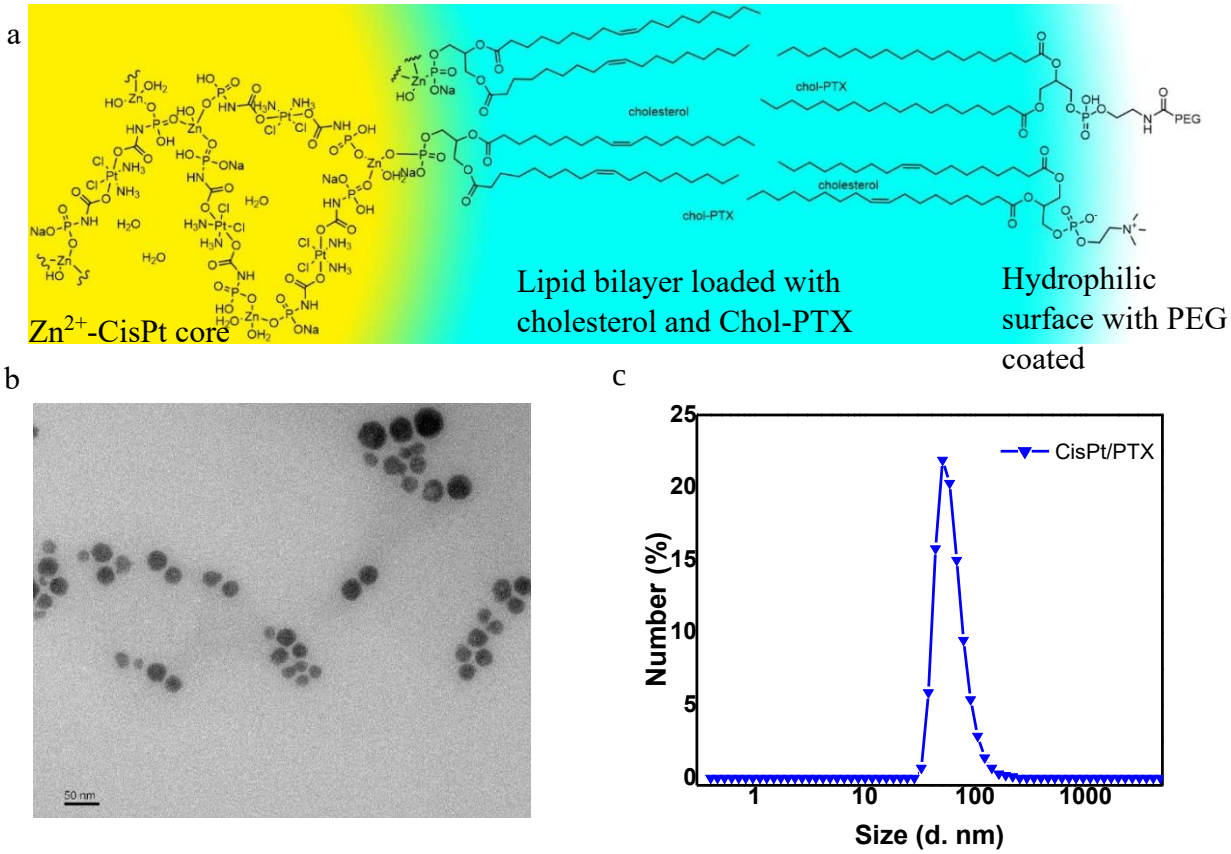

Figure 4-2. Synthesis of CisPt/PTX particle. (a) Schematic illustration of CisPt/PTX and its chemical composition. (b) TEM image of CisPt/PTX. (c) Size distribution of CisPt/PTX measured by DLS.

Under transmission electron microscopy (TEM), the particles showed spherical shape and were monodispersed (**Figure 4-2** b). CisPt/PTX had a Z-average diameter of 92.70 + 0.70 nm and polydispersity index (PDI) of 0.15 ± 0.01 by dynamic light scattering (DLS) (**Figure 4-2** c). The particles were stored at room temperature or incubated with bovine serum albumin (BSA) at 37 ^{o}C to test the stability during storage and blood circulation. No

precipitation formed during the stability test and negligible change on size and PDI could be observed (**Figure 4-3** a and b). To further confirm its stability, the drug released from particles was collected by ultrafiltration or dialysis. Ultrafilterable dugs appeared to be slightly more than dialyzable drugs, probably due to disruption of particle structure during centrifugation and ultrafiltration. Negligible amount of CisPt (measured by ICP-MS) or

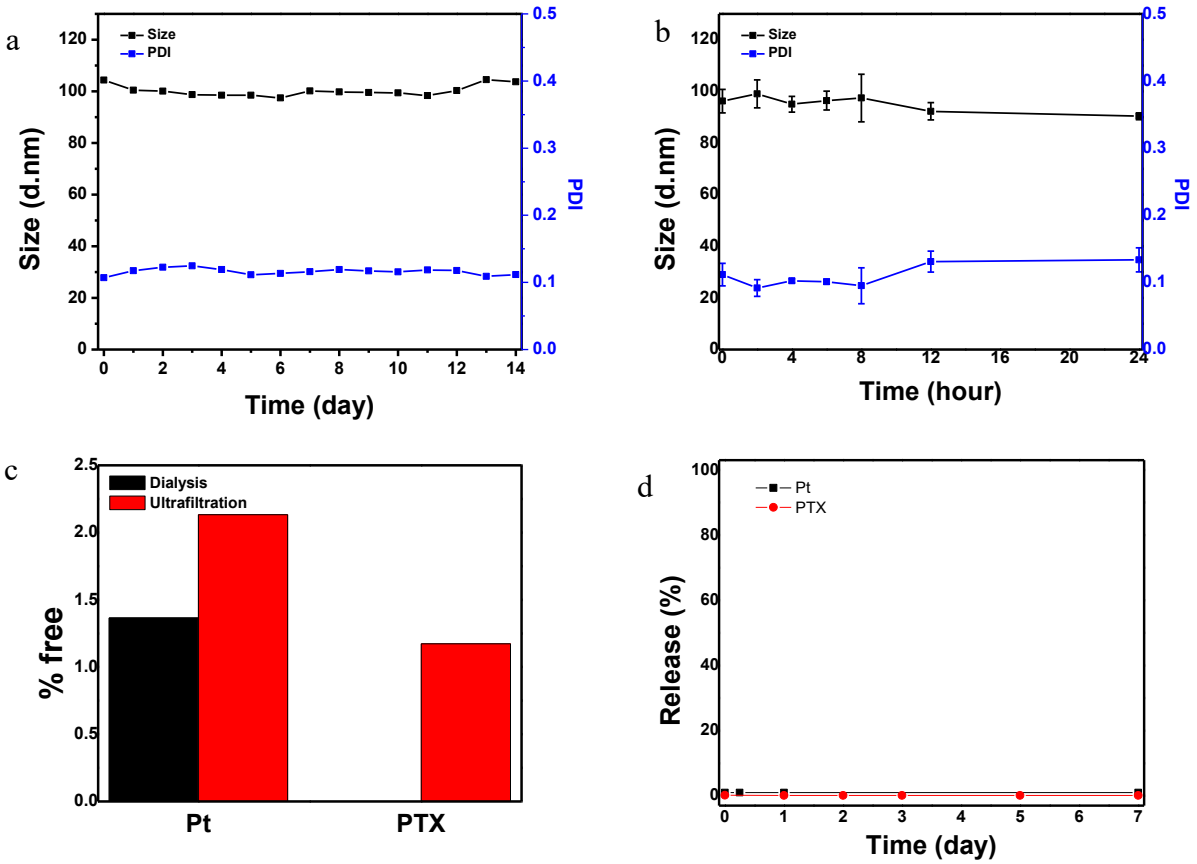

Figure 4-3. Stability test of CisPt/PTX. Change in size and PDI when CisPt was stored at room temperature (a) or incubated at 37 ^{o}C with 5% BSA (b). (c) Comparison of two methods of testing drug release on a CisPt/PTX sample stored for 24 h. (d) Pt and PTX observed outside of CisPt/PTX over time, measured by the dialysis method.

PTX (measured as chol-PTX using LC-MS) were observed outside of CisPt/PTX at room temperature for one week using the dialysis method, proving the high stability of the particle (**Figure 4-3** c and d).

4.2.2 Release of CisPt and PTX from CisPt/PTX

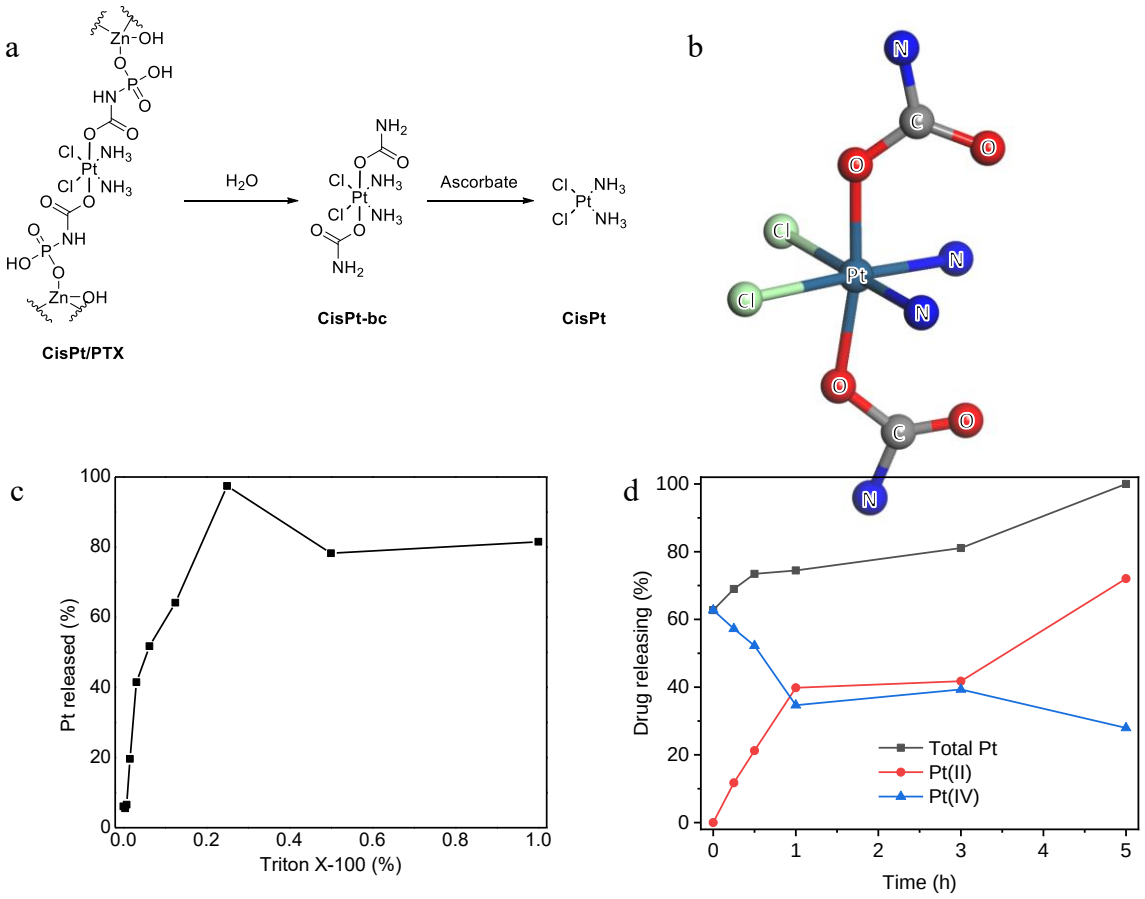

Figure 4-4. The release mechanism of CisPt. (a) Proposed mechanism of release. (b) Crystal structure of CisPt-bc. (c) Pt release form CisPt/PTX in varying concentrations of Triton X-100 in PBS. (d) Release of different Pt species from CisPt/PTX in 5 mM ascorbate in the presence of 0.5% Triton X-100 in PBS (v/v).

Drug release from CisPt/PTX was studied using the same method as described for OxPt/DHA in Chapter 2. CisPt can be released from the particle via a two-stage process: hydrolysis of the Zn^{2+}-CisPt complex to form a Pt^{IV} intermediate CisPt-bc and reduction of CisPt-bc to form active CisPt (**Figure 4-4** a). When incubated with detergent Triton X-100 to disrupt lipid bilayers, Pt release from the particle can be observed within 10 min and the amount of released Pt at 10 min is dependent on Triton X-100 concentration. 0.25% Triton X-100 (v/v) was sufficient for more than 80% release of Pt (**Figure 4-4** c). HR-LCMS showed that the major species containing the isotope pattern of Pt has an m/z of 420.9782 ($[M+Na]^+$, **Figure 4-5** a). The proposed intermediate could be synthesized by incubating the CisPt prodrug with 1 M HCl for 24 h. The structure was confirmed by X-ray crystallography (**Figure 4-4** b) and the pure compound showed a similar m/z peak of 420.9787 ($[M+Na]^+$, **Figure 4-5** b) and the same peak on LC-MS, indicating CisPt-bc is the intermediate released from the particle after the hydrolysis step. When CisPt-bc was further incubated with 5 mM ascorbate as a reducing agent, peaks of CisPt with m/z of 317.9874 ($[M+NH_4]^+$, **Figure 4-5** c) showed up on HRMS, corresponding to the second step of CisPt release. Incubating CisPt/PTX with 5 mM ascorbate in the presence of 0.5% Triton X-100 in PBS (v/v) showed almost complete release of Pt form the particle in 5 h, with 23% as the Pt(IV) species CisPt-bc and 69% as CisPt (**Figure 4-4** d).

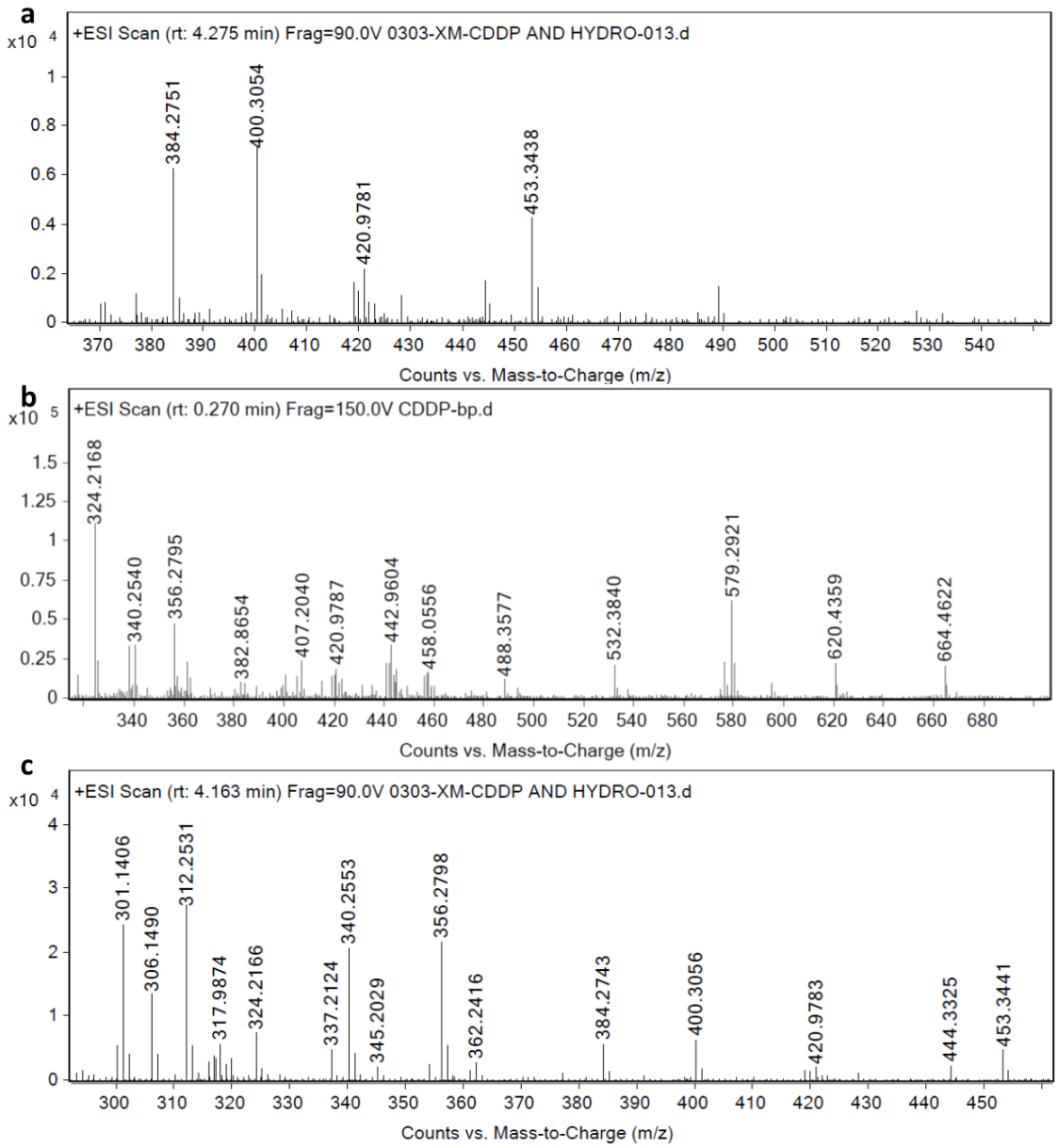

Figure 4-5. (a) HR-LCMS of CisPt/PTX incubated in PBS with Triton X-100 showing the formation of CisPt-bc (m/z = 420.9781 for $[M+Na]^+$). (b) HR-MS of CisPt-bc (m/z = 420.9787 for $[M+Na]^+$) from an aqueous solution of CisPt-bp. (c) HR-MS of CisPt/PTX incubated in PBS with Triton X-100 and 1 mM ascorbate showing the formation of CisPt-bc (m/z = 420.9783) and CisPt (m/z = 317.9874).

a

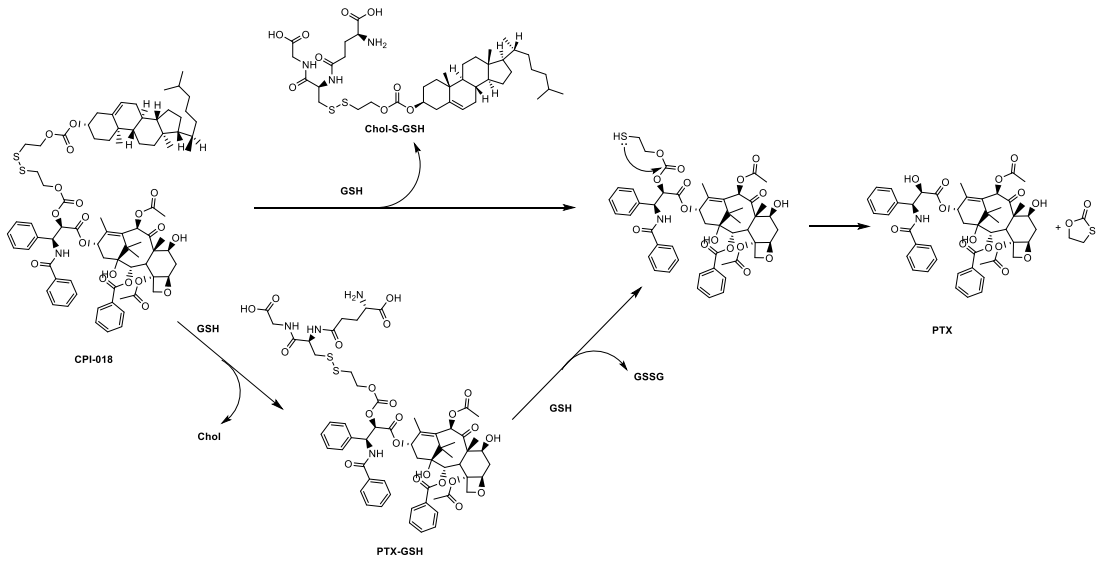

b

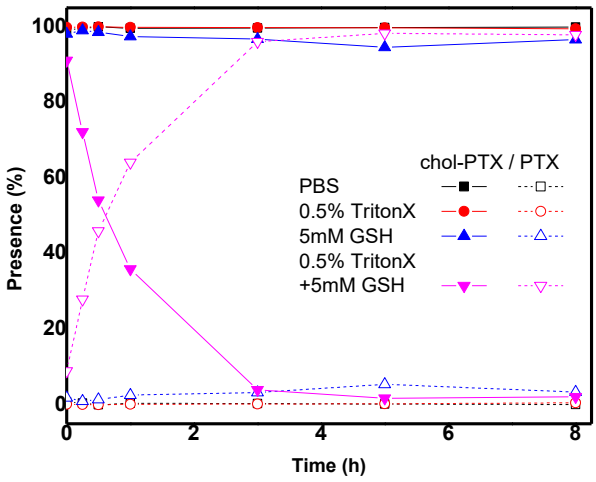

Figure 4-6. Mechanism of PTX release. (a) Disulfide exchange mechanism of PTX release. (b) PTX release from CisPt/PTX when incubated in PBS at 37 °C with or without 0.5% Triton X-100 and GSH.

PTX can be released from chol-PTX prodrug via disulfide exchange (**Figure 4-6** a). Study of PTX release from the prodrug was performed in a solution of 5 mM GSH in 50% THF/PBS (v/v) for better solubility. After incubation with GSH, disulfide exchange product chol-S-GSH (m/z = 796.4221) and PTX-GSH (m/z = 1263.4121) were detected by

HR-MS (**Figure 4-7**). Incubating CisPt/PTX without triton X-100 or GSH did not show significant changes in chol-PTX after 5 h, while 96% of chol-PTX was converted to PTX with both Triton X-100 and GSH at 37 ºC in 3 h (**Figure 4-6** b). The core-shell structure of NCP-1/PTX thus protects CisPt-bp and chol-PTX prodrugs from exposure to reductants during circulation and ensures selective drug activity in cells with abundant reducing agents, such as cancer cells.

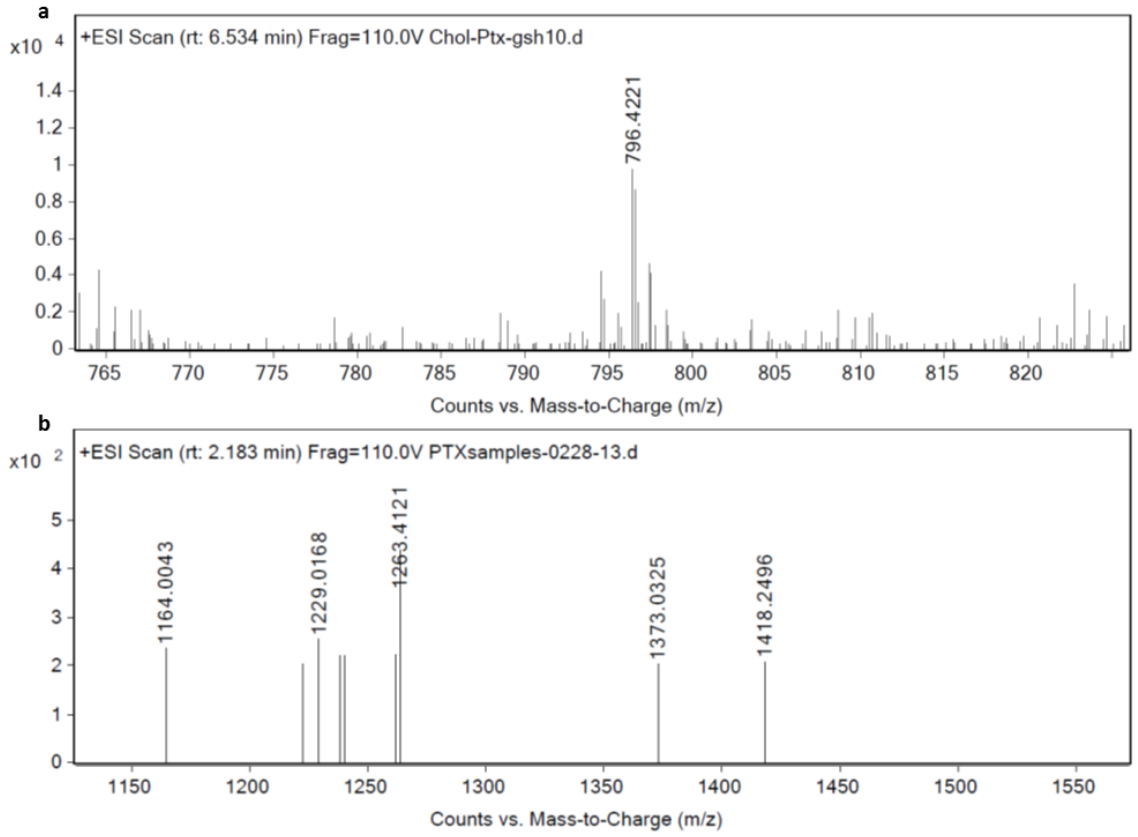

Figure 4-7. Intermediates of disulfide exchange when chol-PTX incubated with 5 mM GSH in PBS (a) Chol-S-GSH (m/z = 796.4221) (b) PTX-GSH (m/z = 1263.4121).

4.2.3 *In vitro* cytotoxicity and cell death

The cytotoxicity of CisPt/PTX and single drug control particles were studied on several human and murine cancer cells (**Table 4-1**). CisPt/PTX significantly lowered the IC_{50} values of both CisPt and PTX compared to single drug control particles in all tested cell lines. In the platinum-resistant human ovarian cell line A2780/CDDP, there was nearly 100% cell viability at the highest tested concentration of 20 μM Pt for CisPt-NCP but decreased to 0.84 μM with the help of PTX. A similar effect also happened on other cell lines, suggesting that the drugs may have some synergistic effects.

Table 4-1. Pt and PTX IC_{50} Values (μM) in some of human and murine cancer cells

	Origin	**Cell line**	**CisPtNCP**	**ZnP/PTX**	**CisPt/PTX**
Ovarian	Human	A2780	4.78 ± 0.04	(0.22 ± 0.15)[a]	0.50 ± 0.21
	Human	A2780/CDDP	>20	(0.62 ± 0.19)[a]	0.84 ± 0.18
	Human	SKOV-3	>20	(0.11 ±0.02)[a]	0.09 ± 0.04
Lung	Human	H460	18.34 ± 3.99	(0.42 ± 0.04)[a]	0.28±0.04
	Murine	LL/2	5.51 ± 1.32	(0.69 ± 0.13)[a]	1.40 ± 0.36

[a]The numbers in parentheses refer to PTX equivalents.

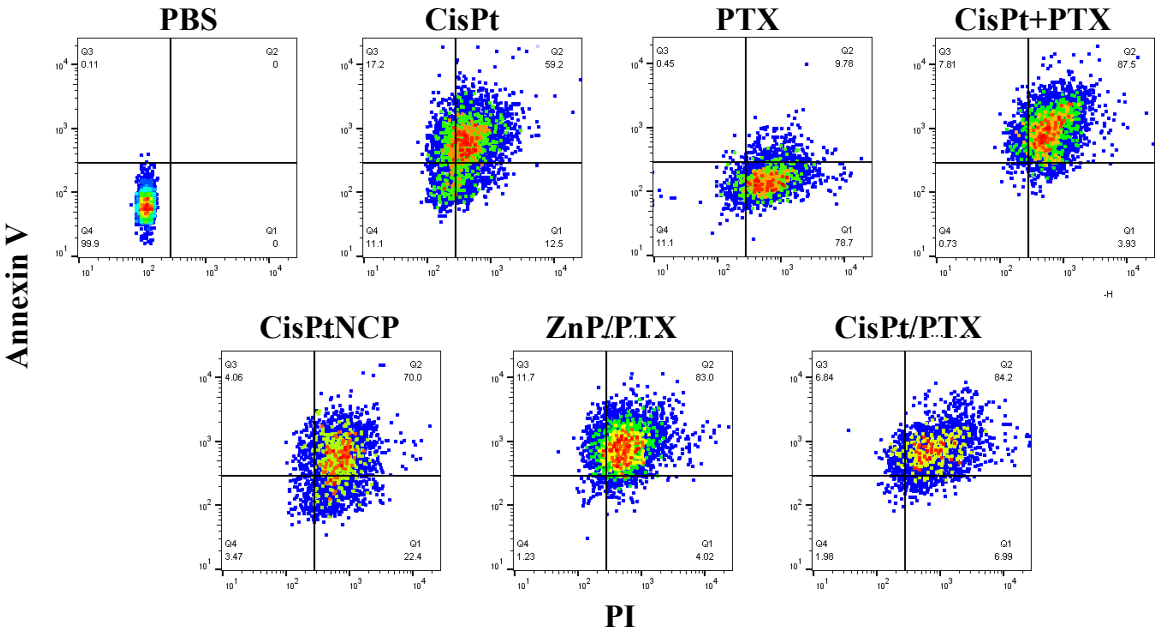

Figure 4-8. Annexin V/PI analysis of H460 cells dosed with CisPt, PTX, CisPt+PTX, CisPtNCP, Zn/PTX, or CisPt/PTX in H460 cells at 5 μM CisPt and/or 1.25 μM PTX equivalents. Quadrants clockwise from the lower left to lower right represent healthy, early apoptotic, late apoptotic/necrotic, and necrotic cells, respectively.

Apoptosis/necrosis of cells induced by different drugs was studied by Annexin V and PI staining. CisPt induced apoptosis in 76.4% of H460 cells when dosed with 5 μM while primarily necrosis (78.7%) was caused by 1.25 μM free PTX. The combination increased the percentage of apoptotic cells to 95.31%. However, CisPt-NCP, Zn/PTX, and CisPt/PTX all led to significant apoptosis at the same concentrations with >90% cell death after CisPt/PTX treatment, indicating NCP kept the cytotoxicity but may alter the mechanism of cell death *in vitro*.

4.2.4 Pharmacokinetics and biodistribution

NCP has been demonstrated to improve drug circulation and increase drug exposure. Pharmacokinetic and biodistribution studies of CisPt/PTX were carried out on healthy rats and 4T1 tumor-bearing mice, respectively. SD/CD rats received a bolus injection of free CisPt, free PTX, or CisPt/PTX at equivalent doses of 1.95 mg Pt/kg and 2.1 mg PTX/kg, and plasma samples were collected at various time points for analysis. At the beginning of injection, plasma Pt and PTX concentrations are around 12 and 35 times higher respectively, as shown by the 5 min data. Free Pt and PTX were below the detection limit 24 h after injection, while significant amounts of both drugs remained in blood circulation when dosed with CisPt/PTX (**Figure 4-9** a, b and c). The overall effect of encapsulation into NCP is an increase of about 512 and 442 times in the drug exposure of CisPt and PTX, respectively, determined by the areas under curve ($AUC_{0-\infty}$) values of the two drugs (**Table 4-2**).

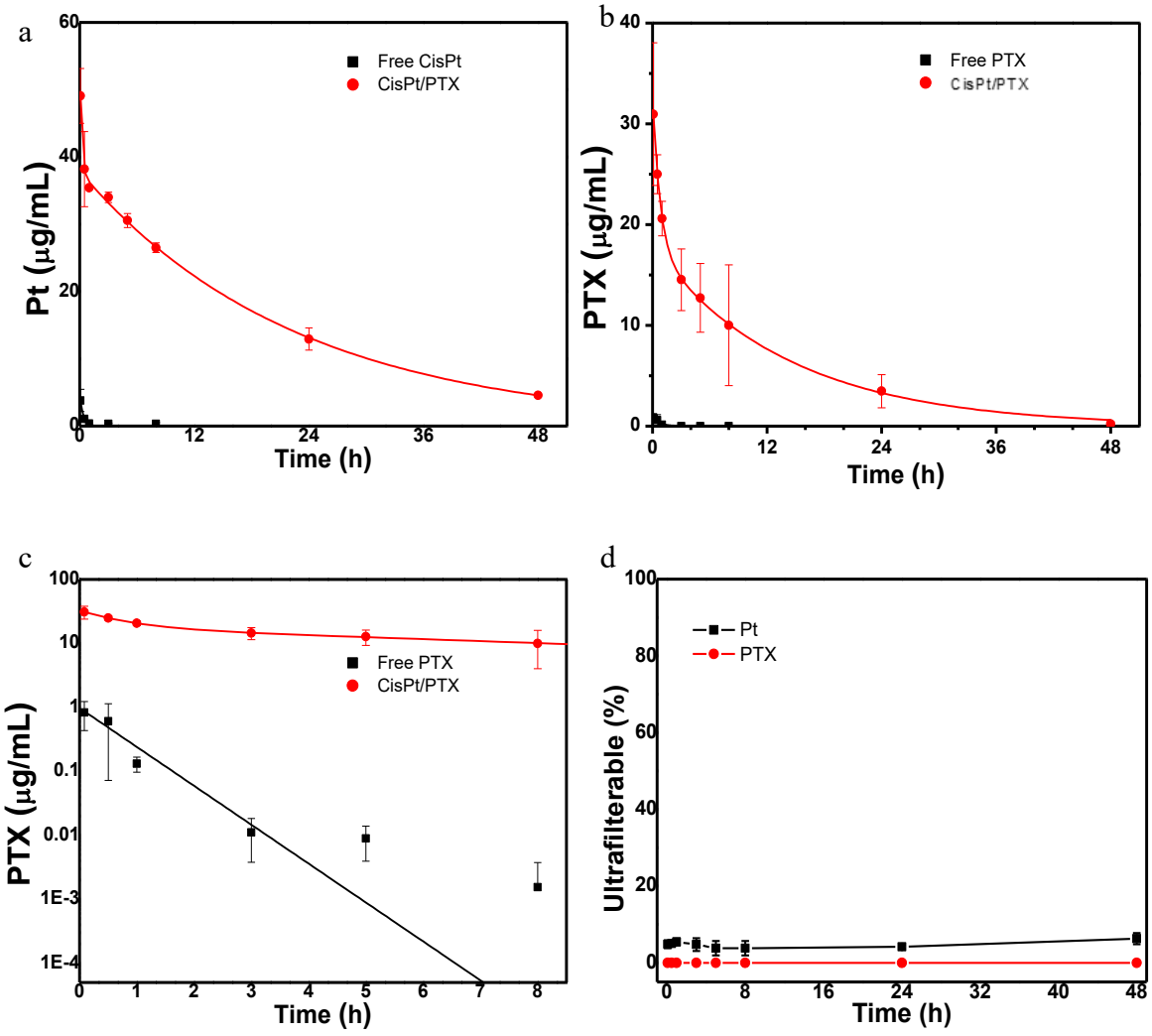

Figure 4-9. Pharmacokinetics of CisPt/PTX. (a) Plasma Pt concentration of CisPt/PTX comparing with free CisPt. (b) Plasma PTX concentration of CisPt/PTX comparing with free PTX. (c) Log-scaled curve of (b) for better illustration. (d) Ultrafilterable Pt and PTX form plasma of CisPt/PTX dosed rat.

Table 4-2. Pharmacokinetic parameters of CisPt and PTX

Parameters	**$AUC_{0\rightarrow\infty}$ (μg/mL•h)**	**AUMC (μg/mL•h^2)**	**$t_{½\alpha}$ (h)**	**$t_{½\beta}$ (h)**	**MRT (h)**
Free CisPt[a]	1.71 ± 0.35	0.65 ± 0.23	0.27 ± 0.09	____	0.39 ± 0.13
Free PTX	(0.70 ± 0.46)[b]	(0.50 ± 0.38)[b]	(0.49 ± 0.08)[b]	____	(0.71 ± 0.11)[b]
CisPt/PTX[a]	610.5 ± 174.2 (264.6 ± 113.8)[c]	11883.5 ± 5081.7 (3624.0 ± 2424.0)[c]	0.57 ± 1.37 (0.54 ± 0.91)[c]	13.65 ± 2.53 (12.62 ± 1.86)[b]	19.47 3.42 (13.69 ± 2.60)[c]

[a] Pt content was used for pharmacokinetic analysis

[b]The numbers in parentheses refer to PTX

[c]These numbers were detected as chol-PTX but expressed as PTX equivalent

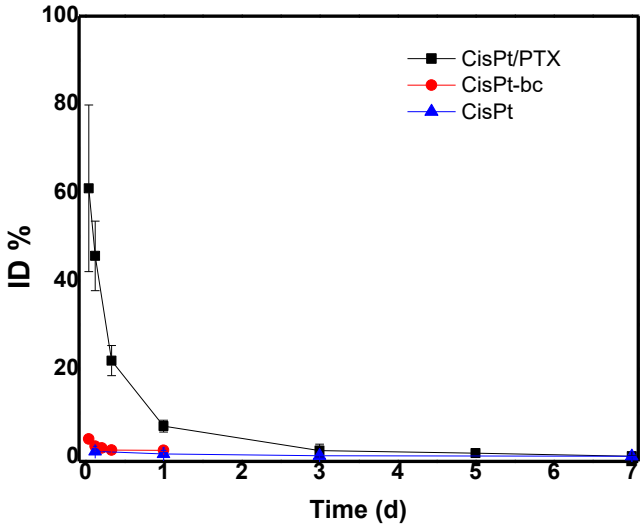

Figure 4-10. Plasma concentrations of Pt in BALB/c mice dosed with CisPt/PTX, CisPt-bc, or CisPt.

Importantly, when passing plasma through 3kDa Amicon Ultra Centrifugal Filter at 10,000 rpm (6708 g) for 30 min, ultrafilterable Pt detected from the plasma ultrafiltrate was consistently observed at 4-6% of the total Pt content, similar to the background Pt release of CisPt/PTX particle following the same protocol, which indicates that the circulating drug still existed in nanoparticle form (**Figure 4-9** d). Chol-PTX was also observed to be stable in circulation, free PTX was below the detection limit at all time points in CisPt/PTX treated rats. Similar improvements in the pharmacokinetics were observed in BALB/c mice: 45.6% of Pt remained in the plasma 3h after injection by CisPt/PTX compared to 2.5% and 1.3% remaining by CisPt-bc and CisPt, respectively (**Figure 4-10**). This further supports that the circulating Pt existed primarily in the form of NCPs rather than released CisPt-bc. At this dose level, CisPt/PTX was found to be relatively nontoxic to mice for at least two weeks, as observed by consistent body weight and activity.

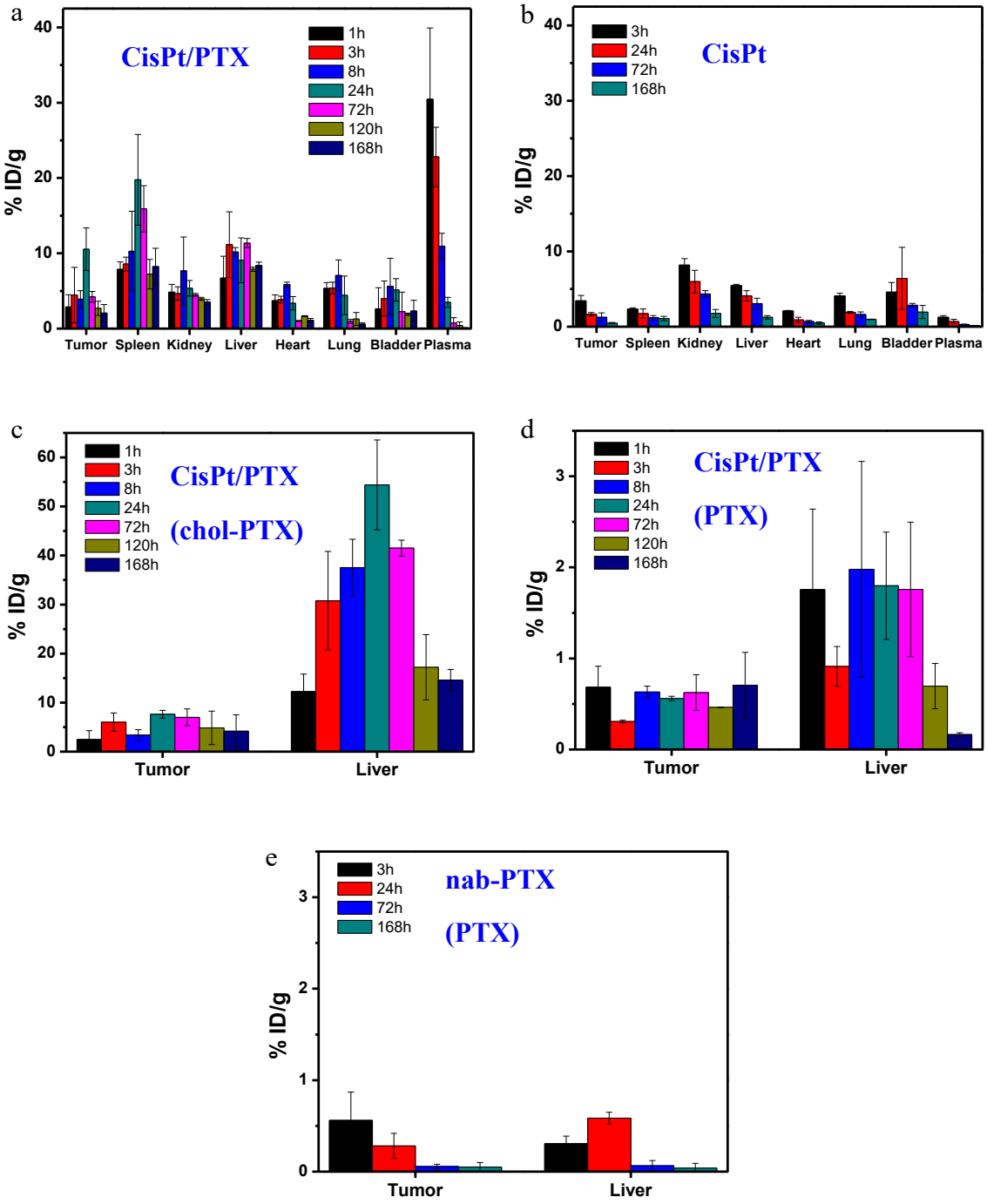

Figure 4-11. Biodistribution and tumor uptake of total Pt (a, b), chol-PTX (c), and PTX (d, e) in 4T1 tumor-bearing mice after i.v. injection of CisPt/PTX (a, c, d) or CAnP (b, e).

We synthesized a BSA-bound PTX (nab-PTX, commercial name abraxane®) that is currently used for PTX delivery clinically for comparison with CisPt/PTX-delivered PTX *in vivo*. Female mice bearing 4T1 tumors approximately 80-120 mm^3 in size were randomly divided into three groups and intravenously injected with CisPt and nab-PTX (CAnP) or CisPt/PTX at equivalent 0.65 mg Pt/kg and 0.71 mg PTX/kg doses. At predetermined time points, the mice were euthanized and the blood, tumor, spleen, kidney, liver, heart, lung, and bladder were harvested to determine the Pt concentrations by ICP-MS and the chol-PTX and PTX concentrations by LC/MS, wherever applicable (**Figure 4-11**). The Pt distribution was normalized against the injected dose and organ weight. CisPt/PTX significantly alters Pt circulation and distribution, with enhanced tumor uptake and a relatively low accumulation (<10 percent injected dose per gram tissue [% ID/g]) in the kidney, lung, and bladder. The tumor concentration reached a maximum of 10.5+2.8% ID/g tissue 24 h after intravenous injection with CisPt/PTX, compared to a maximum of 3.4+0.7% ID/g 3 h after intravenous injection with CisPt.

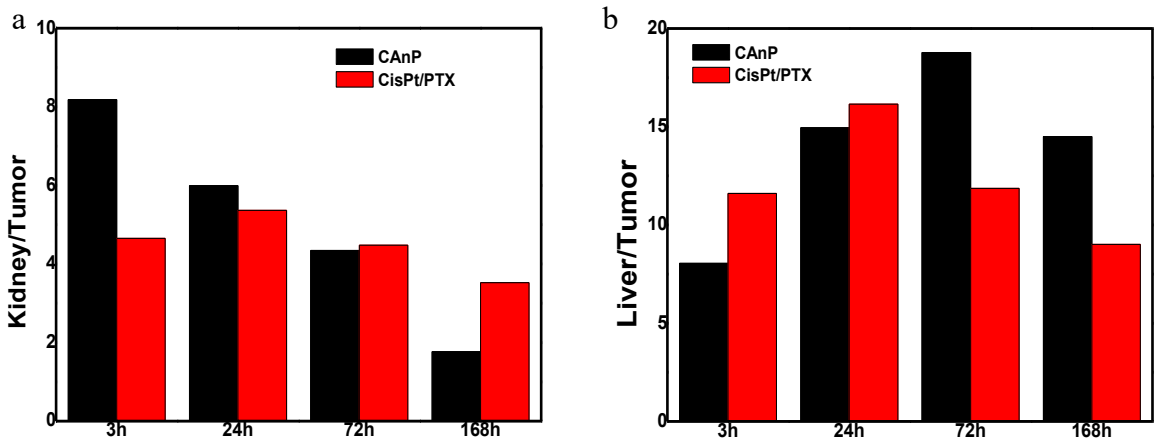

Figure 4-12. Ratio of Pt in major organs versus Pt in tumor at different time points in 4T1 tumor-bearing mice treated with CisPt/PTX or CAnP.

As a proxy for the renal clearance, the Pt accumulation in the kidney was not significantly different in mice dosed with CisPt/PTX compared to CisPt. The kidney/tumor Pt ratio was fairly consistent in mice dosed with Cis/PTX, whereas the kidney/tumor Pt ratio in mice dosed with CisPt steadily decreased over time. This indicates that the rapid renal clearance of free CisPt is flattened when switched to NCP particles, which helps to avoid the risk of renal toxicity from high maximum kidney concentration at similar tumor Pt levels (**Figure 4-12** a). In comparison, the liver to tumor Pt ratio increases with prolonged exposure to CisPt, potentially due to faster clearance of Pt from the tumor than the liver. In CisPt/PTX treated mice, the liver to tumor Pt ratio decreases with time due to faster clearance from the liver compared to the tumor and also showed a similar "flatten" effect to avoid high maximum liver concentration at similar tumor Pt levels (**Figure 4-12** b).

Significant liver accumulation of chol-PTX (up to 54.4 ± 9.2% ID/g) occurred in mice dosed with CisPt/PTX (**Figure 4-11** c). Importantly, chol-PTX shows little to no cytotoxic activity (**Figure 4-13** d) and is not easily metabolized by liver enzymes. PTX and chol-PTX incubated in murine liver microsomes in the presence of an NADPH generating system digested ~30% of PTX and negligible chol-PTX in 15 min at 37 °C (**Figure 4-13** a). This may contribute to the sustained chol-PTX and subsequent PTX concentrations in both the tumor and the liver. The free PTX levels remain only ~1-2% ID/g for at least 72 h after injection. Chol-PTX in the tumor hovers around 2.5-7.0% ID/g for up to one week, with corresponding free PTX levels continuously around 0.6% ID/g. This represents an intratumoral drug concentration of ~100 nM, which is higher than most reported IC_{50} levels for PTX. The tumor environment reduces chol-PTX to PTX much more efficiently than the liver environment. In comparison, the highest tumor accumulation in mice dosed with

nab-PTX occurs 3 h after administration. This level of 0.56+0.31% ID/g is similar to the peak concentration in NCP-1/PTX treated mice, but the PTX concentration cannot be maintained.

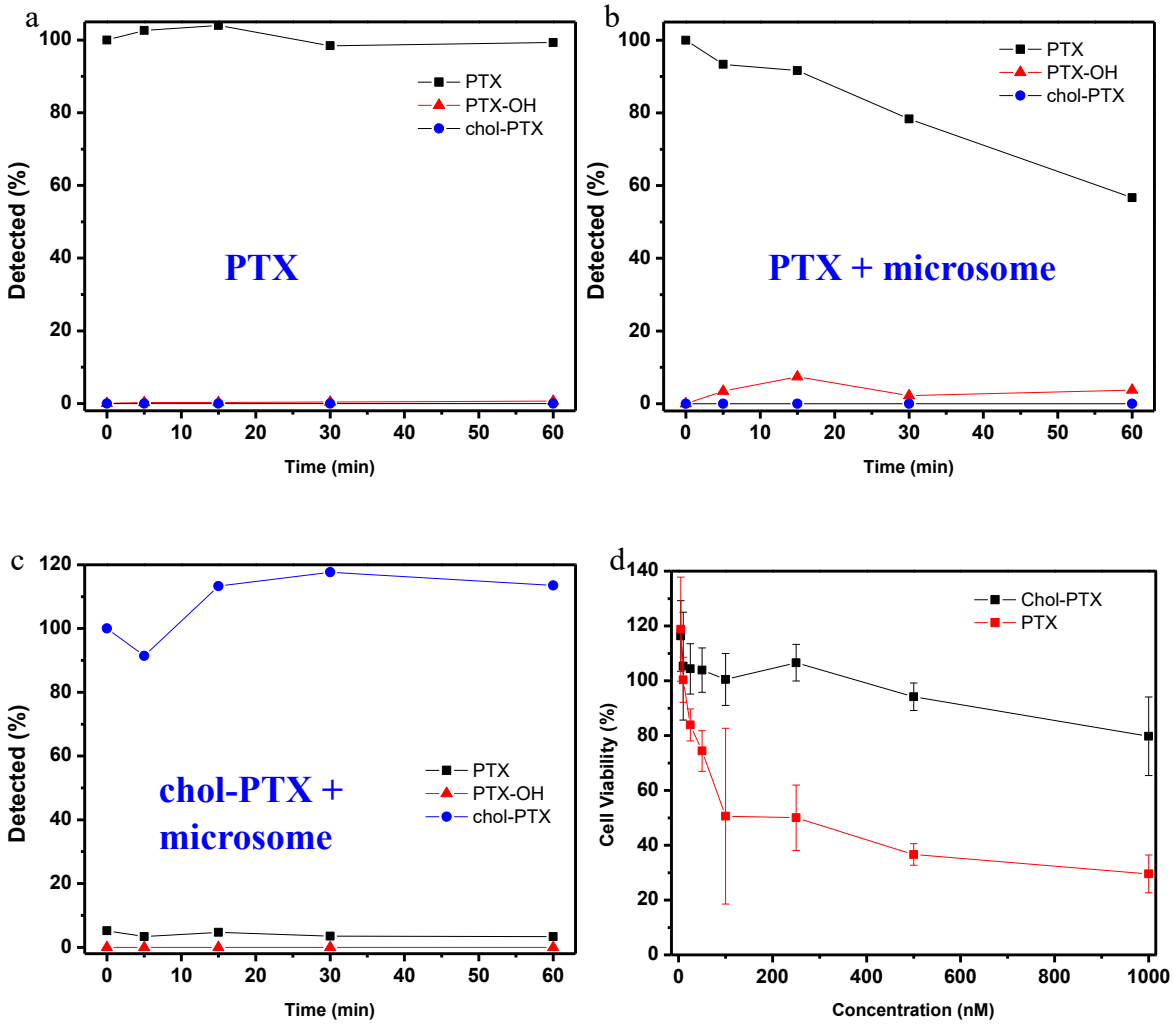

Figure 4-13. Stability of PTX (a and b) and chol-PTX (c) against liver microsomes and cytotoxicity of PTX and chol-PTX.

4.2.5 *In vivo* anticancer efficacy

The *in vivo* anticancer efficacy of CisPt/PTX was evaluated in subcutaneous human and murine ovarian (human A2780, A2780/CDDP, and SKOV-3), lung (human H460 and murine LL/2), and breast (murine 4T1) xenografts (**Figure 4-14**). When the tumors reached 70-120 mm3 in volume, mice were injected intravenously once a week with CisPt/PTX at a dose of 0.49 mg Pt/kg and 0.53 mg PTX/kg or with the combination of free CAnP at a dose of 3.9 mg Pt/kg and 8.0 mg PTX/kg. In all tested models, CisPt/PTX led to significant tumor growth inhibition with minimal toxicity observed by both weight and histopathology of the major organs. In the human xenograft model of Pt-sensitive ovarian carcinoma A2780 on athymic nude mice, 25% of CisPt/PTX treated mice had no discernible tumor by day 13 post first treatment and a total of 99.5% tumor growth inhibition (TGI, defined as $1-(RTV_t/RTV_c)$ where RTV = endpoint tumor volume). In the human H460 and murine LL/2 lung cancer models on athymic nude mice and C57Bl/6 mice, respectively, CisPt/PTX showed significantly greater anticancer efficacy than CAnP. Despite 8 times increase in CisPt dose and 15 times increase in PTX dose, the anticancer efficacy of free CisPt and nab-PTX (65.2% and 69.6% TGI for H460 and LL/2, respectively) led to less tumor growth inhibition than CisPt/PTX (88.1% and 83.8% TGI for H460 and LL/2, respectively). Importantly, CisPt/PTX was well tolerated by mice compared to free CisPt and nab-PTX where several mice were moribund by the end of the study with splenic hemorrhage, seen as orange-brown spots indicative of hemosiderin, and necrosis in the liver. Similar results were observed in the murine 4T1 triple-negative breast cancer model on BALB/c mice.

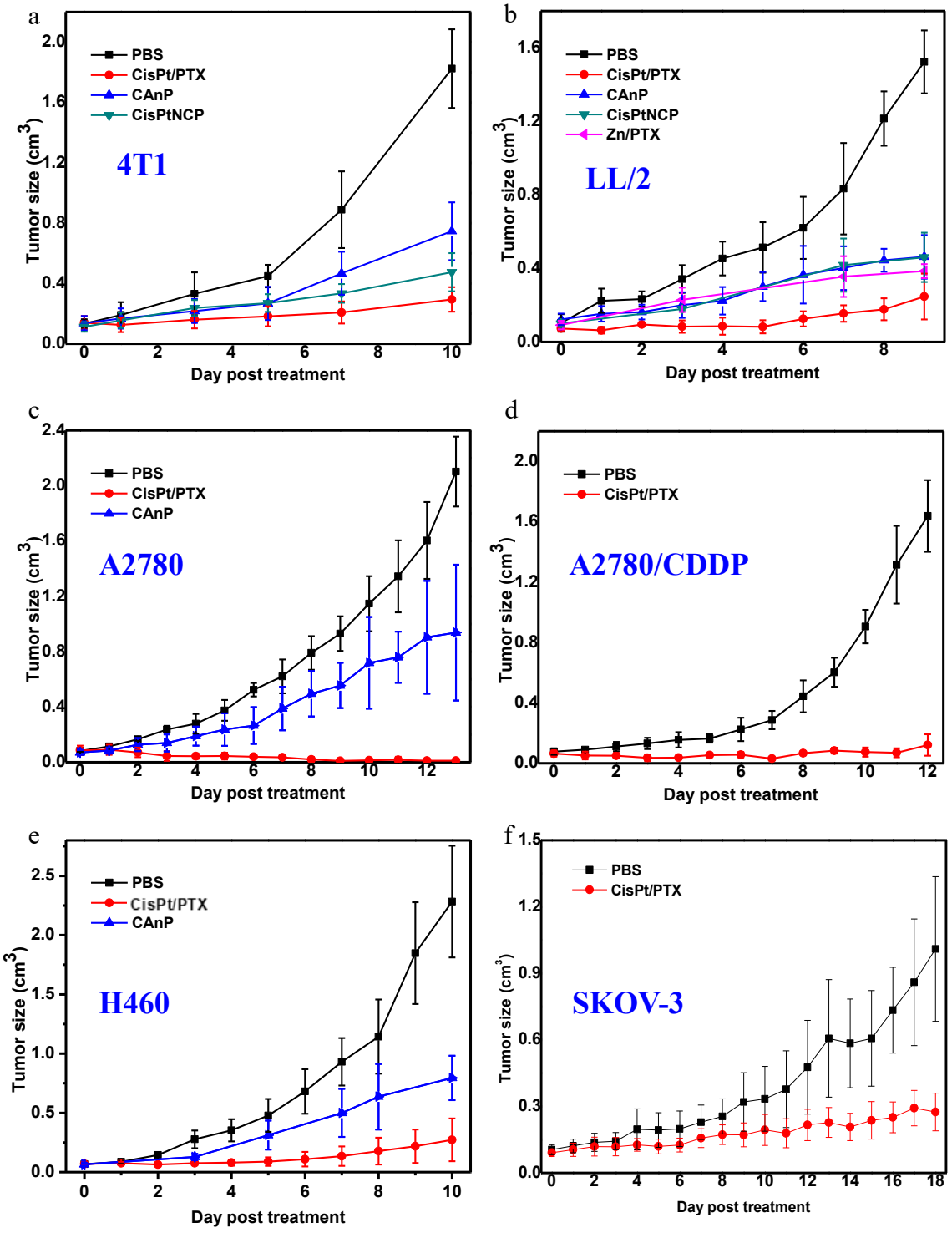

Figure 4-14. *In vivo* anticancer efficacy of CisPt/PTX on various types of tumor models.

a

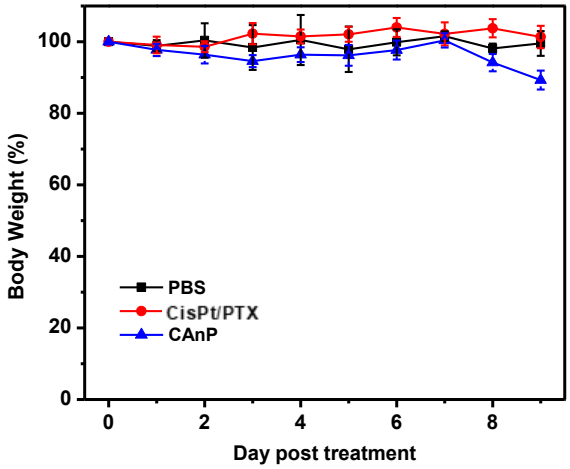

b

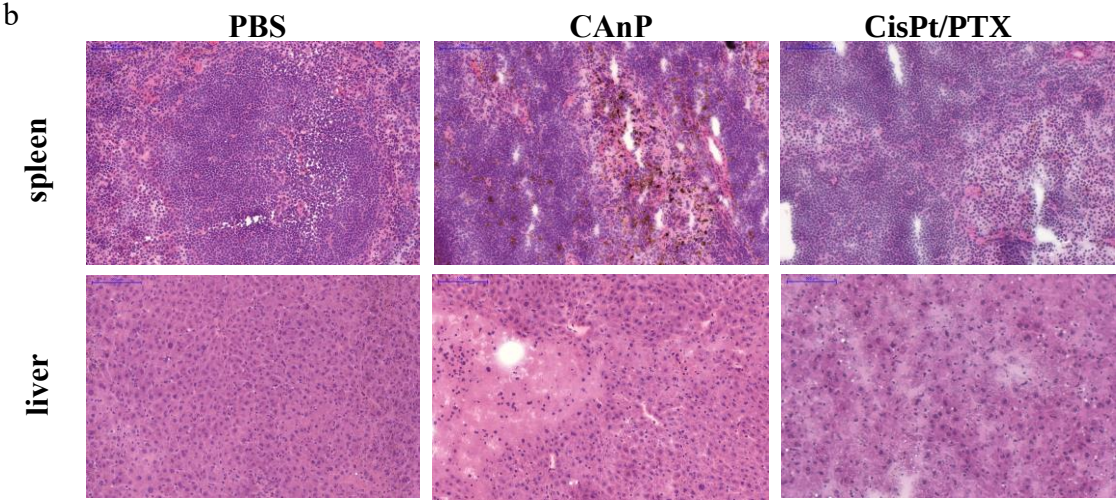

Figure 4-15. Toxicity of CAnP and CisPt/PTX by body weight (a) and histology (b).

4.2.6 Interaction between Cis/PTX and liver lipids

Although CisPt/PTX was stable under physiological conditions (e.g., 5% BSA at 37 ^{o}C) and a negligible amount of chol-PTX was detected in plasma ultrafiltrates of rats dosed with CisPt/PTX, CisPt/PTX showed different pharmacokinetic parameters for CisPt and PTX. Chol-PTX is cleared faster from plasma than CisPt, with a longer mean retention

time (MRT) (19.47 ± 3.42 h for CisPt and 13.69 ± 2.60 h for chol-PTX) (**Table 4-2**). In addition, approximately 10% CisPt remained in blood circulation 48 h post injection of CisPt/PTX but less than 1% chol-PTX remained in circulation at this time point (**Figure 4-9**). As CisPt/PTX is stable in blood and chol-PTX is completely water-insoluble, we hypothesize that chol-PTX is transferred from CisPt/PTX to plasma proteins and circulates as a chol-PTX/plasma protein complex in the blood.

Chol-PTX has a long retention time in the liver upon i.v. injection of CisPt/PTX to mice. After i.v. administration of CisPt/PTX to 4T1 tumor-bearing Balb/c mice, the chol-PTX uptake in the liver peaked at >50% ID/g and remained 15% ID/g after one week (**Figure 4-11** c). While Abraxane[49, 50] and Doxil[51, 52] showed low levels of liver uptake, ^{99m}Tc-labeled LDL showed long drug retention in the liver.[53] Since the liver is the key organ for generating and recycling lipoproteins and LDL is the main lipoprotein nanoparticle responsible for the homeostasis of cholesterol esters, we believe that LDL transfers chol-PTX from CisPt/PTX and acts as a carrier for chol-PTX in blood circulation.

The livers of CisPt/PTX-treated Balb/c mice were analyzed to support the interaction between chol-PTX and LDL. As LDL is responsible for lipid circulation, a portion of a molecule that circulates with LDL is trapped in the lipid that is stored in the liver. We found that ~10% chol-PTX was present in the intercellular space at all time points, while the remaining chol-PTX was nearly equally distributed in liver cells and lipids (**Figure 4-16**). The percentage of chol-PTX in the lipid appeared to slightly increase over time. This result suggests that chol-PTX can hijack the lipid homeostasis pathway via its interaction with LDL.

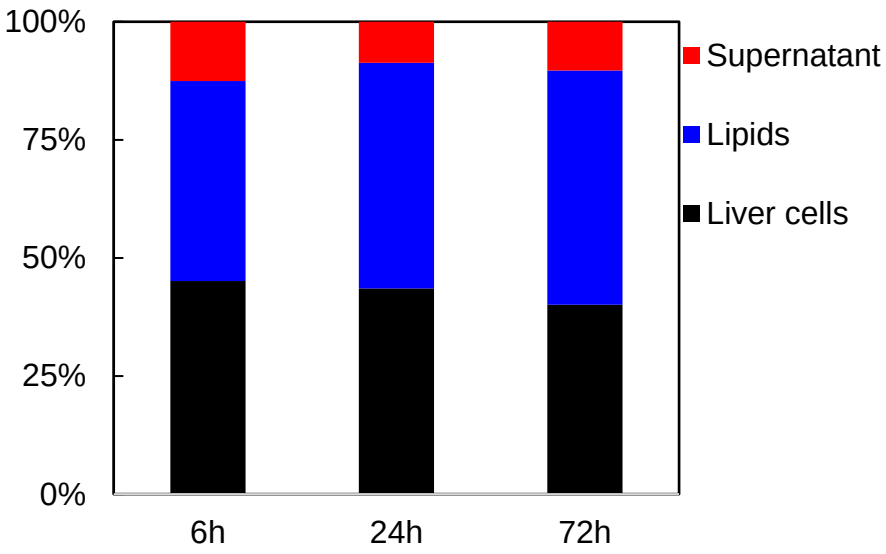

Figure 4-16. Distribution of chol-PTX in mouse liver.

4.2.7 CisPt/PTX interacts with LDL *in vitro* and *in vivo*.

To further investigate the interaction between LDL and CisPt/PTX, we carried out more direct studies on rat plasma. Plasma was collected from SD/CD rats 2 h after receiving a bolus injection of CisPt/PTX at equivalent doses of 2.1 mg PTX/kg. Blank rat plasma was incubated with the same concentration of CisPt/PTX at 37 ^{o}C for 2 h and CisPt/PTX incubated in PBS were prepared as the control group. All samples were treated with an equal volume of LDL precipitation buffer (Abcam, ab105138) for 10 min and then centrifuged at 2000 g to collect LDL as precipitates. The precipitate and supernatant were analyzed by LC-MS to determine the concentration of chol-PTX. In plasma samples incubated with CisPt/PTX, 50% of chol-PTX were found in the precipitates while in PBS control, only 7% chol-PTX was precipitated by the LDL precipitation buffer. In plasma collected from CisPt/PTX-treated rats, 28% of chol-PTX was found in the precipitate.

These results indicate that chol-PTX interacts with LDL in rat plasmas *in vivo* and *ex vivo* (**Figure 4-17** a).

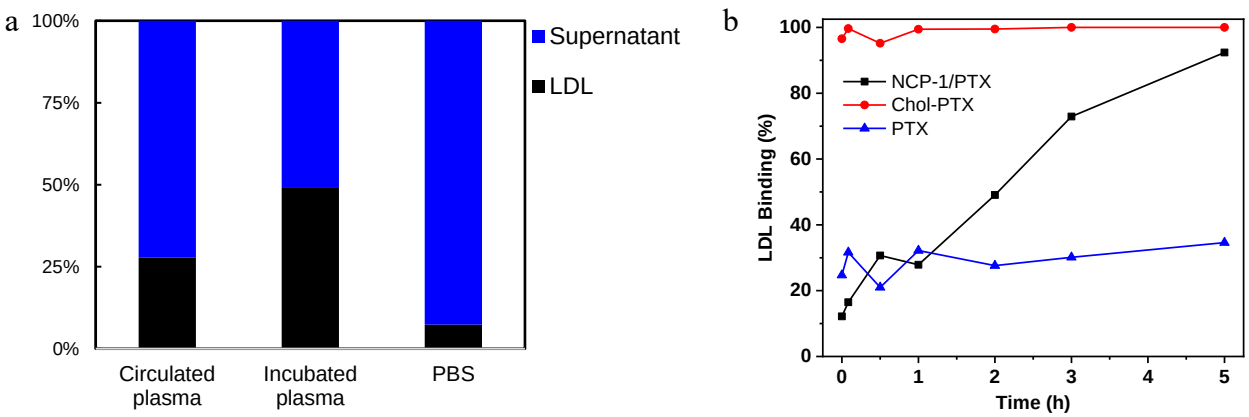

Figure 4-17. (a) The percentage of LDL-bound chol-PTX in plasma incubated with CisPt/PTX or collected from CisPt/PTX-treated rats. (b) The kinetic profile of chol-PTX or PTX binding with LDL.

A time-dependent study was carried out to determine the kinetics of LDL-NCP interaction by incubating CisPt/PTX or drug solutions with rat plasma at 37 ^{o}C. Chol-PTX dissolved in DMSO was instantaneously absorbed by LDL in rat plasma. In contrast, only 30% PTX dissolved in DMSO was adsorbed by LDL in rat plasma. The majority of PTX was bound to other plasma proteins (likely albumin). CisPt/PTX showed a time-dependent interaction with LDL. Chol-PTX was transferred to LDL when incubated in plasma and LDL uptook 90% chol-PTX from CisPt/PTX in 5 hours (**Figure 4-17** b).

4.2.8 Cellular uptake of chol-based drugs is mediated by LDL receptor

A cell uptakes LDL via the interaction between the LDL receptor (LDLR) on the cell surface and Apo B-100 protein on the surface of the LDL particle. LDL uptake by cells can be inhibited by blocking with an LDLR antibody. To prove this hypothesis, DiI-labeled LDL and LDLR recombinant rabbit monoclonal antibody (32) (Invitrogen) were used to test the inhibition of LDL uptake. LDL uptake was inhibited by 60% and 90%, respectively, with 1 μg/ml and 10 μg/ml antibody, while the cellular uptake of a fluorescently labeled NCP (FL-NCP) with chol-pyro on the surface was not affected by LDLR antibody (**Figure 4-18** a). Plasma background was tested using the same method to rule out possible contributions from background fluorescence (**Figure 4-18** b).

The interaction between LDL and NCP was studied *ex vivo* and *in vivo* using the same method. FL-NCP was either incubated with mouse plasma at 37 ^{o}C for 3 h or injected into living mice and circulated for 3 h. Collected plasma with FL-NCP was incubated with 4T1 cells blocked by LDLR antibody. Parallel experiments were performed on fresh plasma with DiI-LDL as positive controls.

Both incubated plasma (**Figure 4-18** c) and circulating plasma (**Figure 4-18** d) showed similar results in response to LDLR blocking. The uptake of chol-pyro in NCP matched with the uptake of LDL in the same dose-dependent manner: 40-50% reduction with 1 μg/ml antibody and 80-90% reduction with 10 μg/ml antibody. This result suggests that LDL not only transfers chol-based prodrugs from NCP but also mediates the delivery and uptake of chol-based prodrugs *in vitro* and *in vivo*.

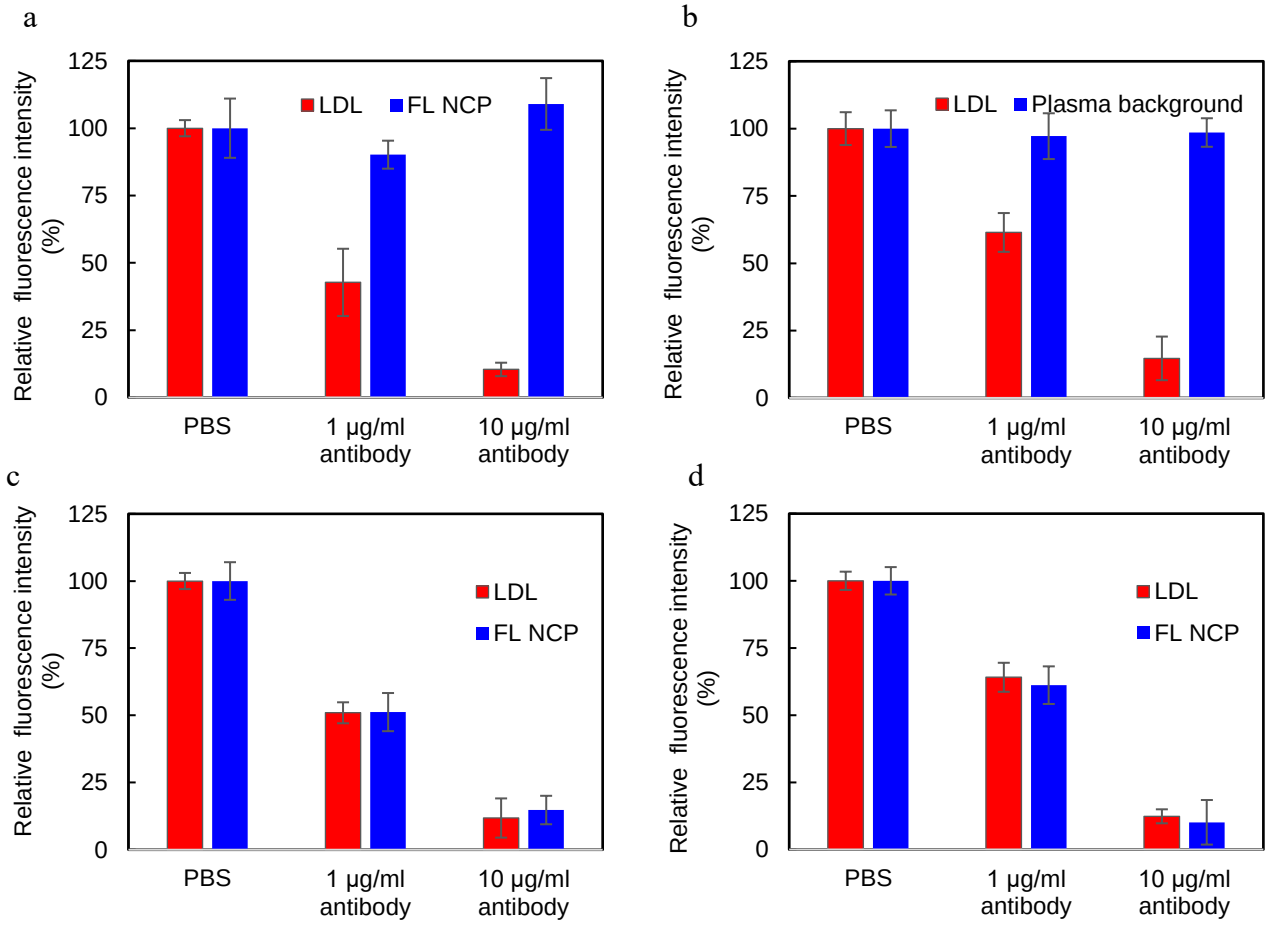

Figure 4-18. (a) Cellular uptake of LDL or FL-NCP when blocked by LDLR antibody. (b) Influence of plasma background on LDL uptake experiment. (c) and (d) Uptake of FL-NCP blocked by LDLR antibody after incubated with plasma (c) or circulated in blood (d) for 3 h.

4.2.9 Mathematical modeling of LDL-mediated circulation of chol-PTX

Knowing the kinetic parameters of chol-PTX transfer and LDL circulation, the difference of pharmacokinetic parameters between Pt and PTX can be explained by mathematical modeling. The circulation half-life of CisPt/PTX was chosen to be 13 h, which is the Pt half-life. The circulation half-life of LDL in literature various in different reports,[54-56] 8h was chosen as an average value of LDL half-life. From the LDL precipitation experiment, the rate of LDL transfer is slower when circulating in rats than incubating *ex vivo*. 28%-7%=21% of chol-PTX was found on LDL after 2h. Based on the formula $N_t = N_0 \left(\frac{1}{2}\right)^{\frac{t}{t_{1/2}}}$ where N_0 and N_t represent the concentration at the beginning and at 2h, the half-life of chol-PTX transfer was calculated to be 6.2 h. But considering the fact that the rate of clearance of chol-PTX in LDL form is 1.6 times that of NCP, the actual half-life of chol-PTX transfer should be shorter than 6.2 h. Here 4 h was chosen as an estimation of chol-PTX transfer half-life. Based on the information above, assuming all processes involved are first-ordered since the measured curves of all processes are close to exponential decay, two equations can be derived:

$$-\frac{d[c]_{NCP}}{dt} = k_1[c]_{NCP} + k_2[c]_{NCP} \quad \text{.....(1)}$$

$$-\frac{d[c]_{LDL}}{dt} = -k_2[c]_{NCP} + k_3[c]_{LDL} \text{.....(2)}$$

Where $[c]_{NCP}$ and $[c]_{LDL}$ stand for the concentrations of chol-PTX located on NCP and LDL, k_1, k_2, and k_3 are rate constants of NCP decay, chol-PTX transfer, and LDL decay, respectively, and t is the time after injection, expressed in hours.

Rate constants can be directly calculated by the half-lives using the formula $k = \frac{ln2}{t_{1/2}}$. From equation (1), $[c]_{NCP}$ can be expressed as $[c]_{NCP} = c_0 e^{-0.2266t}$, where c_0 is the initial concentration of chol-PTX. Applying this expression into equation (2) and take $[c]_{LDL}$=0 at time 0, we can get $[c]_{LDL} = 1.2382c_0(e^{-0.08664t} - e^{-0.2266t})$. So the total plasma concentration of chol-PTX c_{total} is the sum of chol-PTX concentrations in both forms: $c_{total} = [c]_{NCP} + [c]_{LDL} = 1.2382c_0e^{-0.08664t} - 0.2382c_0e^{-0.2266t}$

Concentrations of chol-PTX at different time points can be then calculated and compared with the measured values; they match well the observed values (**Figure 4-19**).

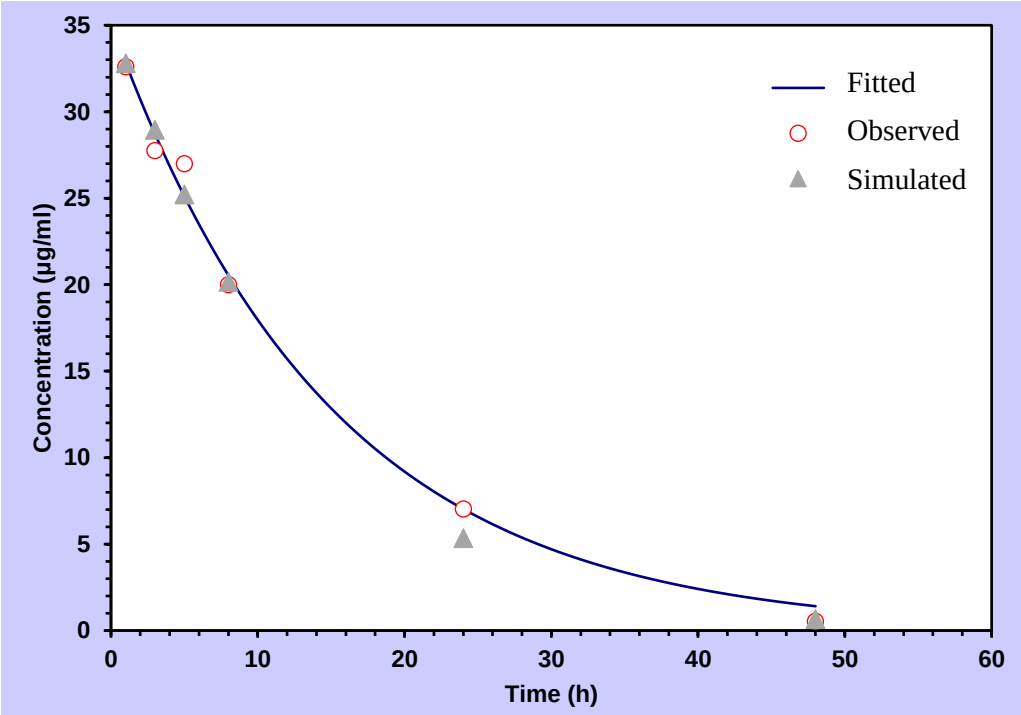

Figure 4-19. Comparison of measured plasma concentration of chol-PTX and mathematically simulated result based on LDL mechanism.

4.3 Discussion

Paclitaxel is a potent anticancer drug, widely used in chemotherapy regimens across a range of cancers with solid tumors. Though preclinical in vitro data has consistently shown the cytotoxicity of PTX on cancer cells, the in vivo preclinical and clinical doses have been similar to or higher than doses of drugs with IC_{50} values one or two orders of magnitude higher than PTX. This may be related to the inefficient delivery of PTX to the tumor and oxidation of PTX by liver P450 enzymes in both the Cremophor EL/ethanol and albumin-bound forms. Our prodrug approach of conjugating cholesterol and PTX via a disulfide bond minimizes active drug exposure in normal tissues, such as the liver, by requiring a biological trigger (i.e. a reducing environment) for drug release. Chol-PTX can escape intact from the liver and be transported to the tumor for continual chol-PTX accumulation and reduction, sustaining active drug levels in the tumor for up to one week.

Using a single nanoparticle to deliver a frequently used clinical combination chemotherapy regimen can simplify therapy. The dose-limiting toxicities of CisPt and PTX are associated with the free drug levels circulating in the bloodstream, requiring pre- and post-hydration for CisPt treatment and long infusion times of up to 24 h for PTX treatment. The NCP core-shell structure limits drug exposure in the bloodstream and drug activity in organs other than the target cancer cells. The long circulation half-life and sustained tumor drug concentrations allow for infrequent dosing. Furthermore, the tunable drug loading can accommodate variable drug regimens, dependent on the requirements of the patient.

CisPt/PTX uses nanotechnology to improve the well-established combination CAP therapy. Prodrugs for CisPt and PTX allowed for stable incorporation into the NCP structure and triggered the release of active drug components. This allowed for nontoxic prodrug depots

in the liver and made it possible to re-enter blood via lipid circulation. The particle showed strong interaction with LDL in circulation and organic prodrugs loaded on the lipid bilayer structure can be transferred into LDL. As rapidly growing tumor requires more cholesterol provided by LDL, the mechanism can further improve the targeting effect. The improved pharmacokinetic and biodistribution properties led to increased anticancer efficacy at lower doses in a range of tumor models. These results taken together support the potential for CisPt/PTX as a promising clinical candidate.

4.4 Experimental

4.4.1 Synthesis of prodrugs

Synthesis of CisPt prodrug

3.0 g cisplatin and 30 mL deionized water were charged to a 50 mL round bottom flask with a stir bar. The mixture was stirred and cooled over an ice bath to 0 ^{o}C. 5.45 mL 30% hydrogen peroxide was slowly added to the mixture in 15 minutes. The reaction mixture was stirred in the dark overnight at room temperature. The mixture was carefully concentrated to approximately 5 mL on a rotary evaporator, then added 25mL ethanol and cooled at -20 ^{o}C for 3 hours. The white solid was collected by vacuum filtration followed by washing with cold water (2 x 20 mL) and cold ethanol (2 x 20 mL) to give a quantitative yield (3.3 g) of $Cis(OH)_2$

3.0 g $Cis(OH)_2$ was charged to an oven-dried 50mL round bottom flask with a stir bar. 10 mL anhydrous DMF was added to the flask and the flask was purged with N_2 for 30 min. The mixture was cooled over an ice bath for 15 min and then diethoxyphosphinyl

isocyanate (2.2 mL, 2.55 g, 2.05 eq.) was added dropwisely through a syringe. Then the mixture was slowly warmed up to room temperature and stirred in dark overnight. The resulting mixture was directly loaded on a silica column packed with hexanes and DMF was removed by flushing the column using 1:1 DCM/hexanes mixture. Then the product Cis-ester was collected by flushing the column with 10% methanol in DCM. Yield: 5.5 g (88%)

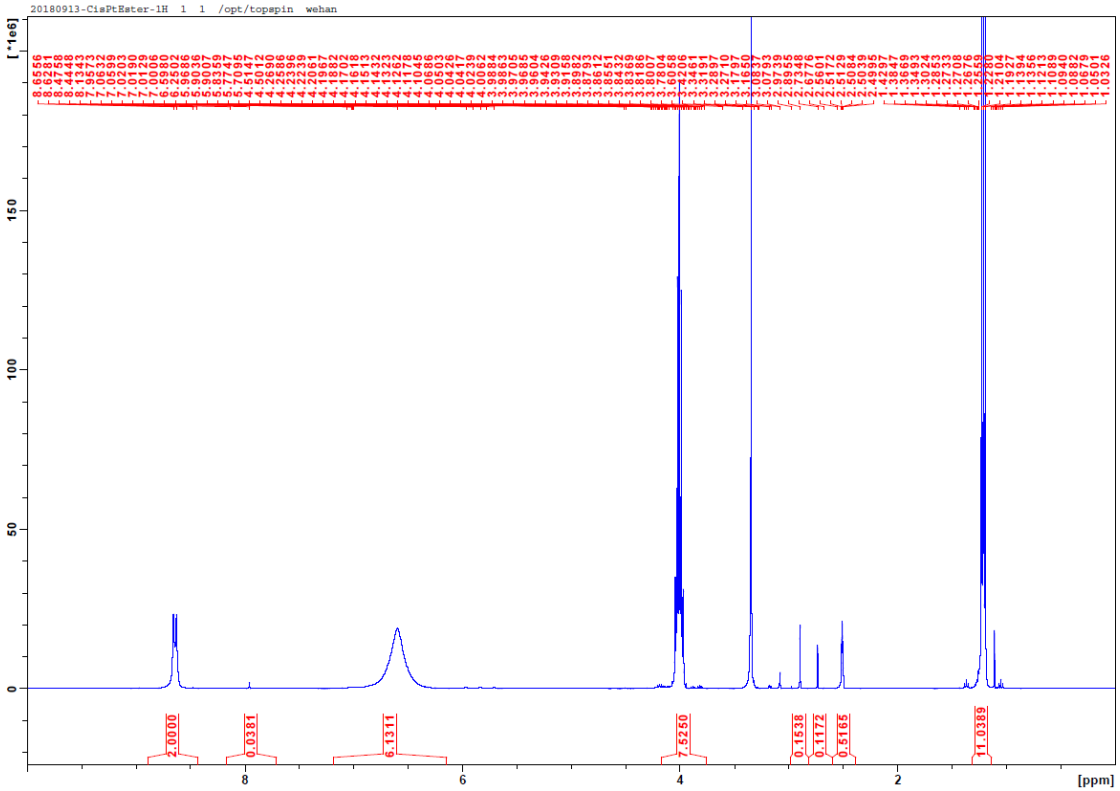

Figure 4-20. ^{1}H-NMR spectrum of Cis-ester

1.0 g Cis-ester was charged to an oven-dried 50 mL round bottom flask with and stir bar. 20 mL anhydrous DCM was added and the flask was purged with N_2 for 30 min. The flask was cooled over an ice bath for 15 min. 2.5 mL bromotrimethylsilane in 5 mL DCM was

added dropwise through a syringe. The reaction mixture was slowly warmed to room temperature and stirred in the dark overnight. The solvent was then removed by rotary evaporation and further dried under high vacuum for 2 hours. Then 5 mL cold methanol was added to the flask and stirred for 30 minutes at room temperature. The product was crushed out by adding 30 mL DCM to the methanol solution and collected by centrifugation at 13000 rpm for 10 min. Yield: 0.6g, 72%.

Synthesis of chol-PTX

To a mixture of cholesterol (500 mg, 1.3 mmol) and 4-N,N-dimethylaminopyridine (DMAP, 0.32 g, 2.8 mmol) in anhydrous DCM, a solution of triphosgene (128 mg, 0.43 mmol) in anhydrous DCM (2 mL) was added dropwise over an ice bath with stirring. The resultant solution was warmed to room temperature and further stirred for 20 min and then added dropwise to a solution of bis(2-hydroxyethyl) disulfide (440 mg, 2.8 mmol) in anhydrous DCM (5 mL) over an ice bath. The reaction mixture was then warmed to room temperature and stirred for 12 h. After removal of solvent, the residue was purified to afford cholest-5-en-3-ol (3β)-, 3-(2-((2-hydroxyethyl)disulfanyl)ethyl) carbonate (Chol-S-S-OH) by column chromatography on silica gel with ethyl acetate/hexane (1:2, v/v). Yield: 0.44 g (60%).

To a mixture of Chol-S-S-OH (83.5 mg, 0.15 mmol) and DMAP (54 mg, 0.44 mmol) in anhydrous DCM (2 mL), a solution of triphosgene (15 mg, 0.05 mmol) in anhydrous DCM (1 mL) was added dropwise over an ice bath with stirring. The resultant solution was warmed to room temperature and further stirred for 1 h and then added dropwise to a solution of PTX (50 mg, 0.058 mmol) in anhydrous DCM (5 mL) over an ice bath. The

reaction mixture was then warmed to room temperature and stirred for 12 h. After removal of solvent, the residue was purified by column chromatography on silica gel with hexane/ethyl acetate (7:1, v/v) to yield 53 mg of Chol-PTX. ^{1}H-NMR (500MHz, $CDCl_3$): 0.87-2.01 (m, 56H), 2.25-2.49 (m, 11H), 2.95 (m, 4H), 3.82 (d, 1H), 4.25 (q, 1H), 4.34 (m, 3H), 4.43 (m, 3H), 4.97 (d, 1H), 5.38 (d, 1H), 5.42 (s, 1H), 5.70 (d, 1H), 6.01 (d, 1H), 6.32 (m, 2H), 7.04 (d, 1H), 7.43 (m, 7H), 7.54 (m, 3H), 7.63 (m, 1H), 7.77 (d, 2H), 8.16 (d, 2H). ESI-MS: m/z=1468.8 ($[M+Na]^+$).

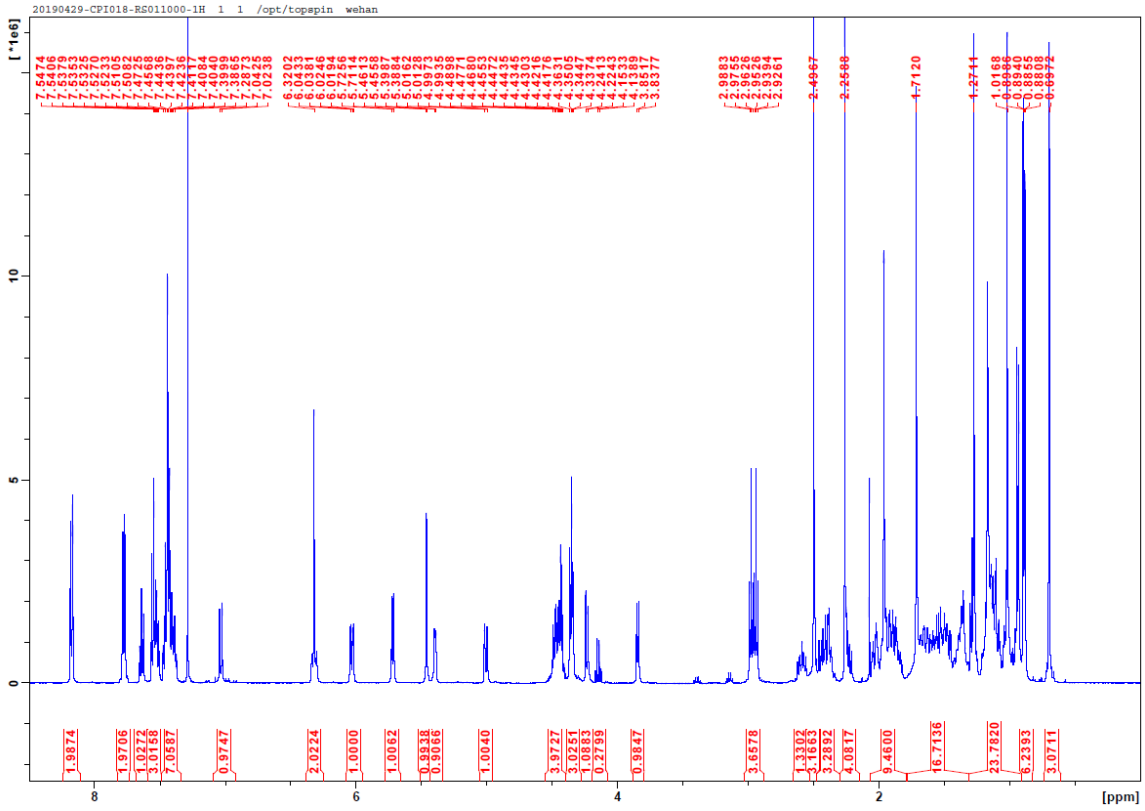

Figure 4-21. ^{1}H-NMR spectrum of chol-PTX.

4.4.2 Preparation and characterization of CisPt/PTX

CisPt core was synthesized according to our previously reported method, with minor modifications.[57] The loadings of CisPt in the particles were determined by inductively coupled plasma-mass spectrometry (ICP-MS, Agilent 7700X, Agilent Technologies, USA) after digestion with nitric acid. CisPt/PTX was prepared by adding a THF solution (80 μL) of DOPC, cholesterol, DSPE-PEG2k (2:1:1 in molar ratio), chol-PTX, and CisPt core to 500 μL of 30% (v/v) ethanol/water at 50 °C. The mixture was stirred at 1,700 rpm for 1 min. THF and ethanol were completely evaporated and the solution was allowed to cool down to room temperature. The particle size and zeta potential were determined by dynamic light scattering (DLS) using a Zetasizer (Nano ZS, Malvern, UK). Transmission electron microscopy (TEM, Tecnai Spirit, FEI, USA) was used to observe the morphology. To determine chol-PTX loading, CisPt/PTX was centrifuged at 13,000 rpm for 30 min, the supernatant was removed and the particles were re-suspended in THF which dissolves the lipid layer to release chol-PTX. The amount of chol-PTX in the nanoparticle suspension was then determined by liquid chromatography-mass spectrometry (LC-MS).

4.4.3 LC-MS method for chol-PTX analysis

1 μL 100 ppm chol-AS solution in acetonitrile was spiked into 100 μL sample as internal standard (ISTD), then the sample was further diluted with 5 μL 20% Triton X-100 and 100 μL saturated NaCl. The mixture was extracted by 100 μL EtOAc and centrifuged at 10000 rpm for 10 min. LC-MS was performed on an Agilent 6540 ESI-Q-Tof LC-HRMS using an Agilent Zorbax SB C-18, 2.1 x 50 mm column with 10 mm guard column. Both chol-DHA and ISTD were eluted by a mixture of 95% methanol and 5% water containing 10 mM ammonium acetate and 0.1% formic acid. The integration area of chol-PTX peak

divided by the area of chol-AS peak was used to determine the concentration of chol-PTX in the original sample.

4.4.4 Analysis of chol-PTX distribution in liver

Livers collected from mice treated with CisPt/PTX were collected 6 h, 24 h, and 72 h after the injection, then digested with 1 μg/ml collagenase IV for 15 min and homogenized. Liver cells were collected by centrifuging the homogenized mixture at 800 rpm for 5 min. The supernatants were further centrifuged at 2500 rpm for 5 min to collect the white lipid components from the liver. Liver cells, lipids, and the final supernatant were analyzed by LC-MS to determine the amount of chol-PTX.

4.4.5 Time-dependent study of chol-PTX transfer in plasma

18 μL CisPt/PTX (1.1 mg/ml by Chol-PTX) or equivalent amount of PTX, chol-PTX solution in DMSO was mixed with 1 ml freshly collected rat plasma and incubated at 37 ^{o}C. Samples were collected at 0 min, 10 min, 30 min, 1 h, 3 h, and 5 h time points. At each time point, 100 μL plasma was collected from the mixture and immediately mixed with 100 μL 2X LDL precipitation buffer, incubated 10 min at room temperature for complete precipitation of LDL and then centrifuged at 2000 g for 10 min to remove LDL in plasma. The supernatant from each sample was collected and extracted with EtOAc, analyzed by LC-MS.

4.4.6 LDLR blocking study

2×10^5 4T1 cells were seeded in each well of 6-well plates and cultured 24 h in medium with 10% FBS, then starved in FBS free medium for 2 h before the study. The LDLR antibody was diluted to 1 μg/ml or 10 μg/ml using FBS-free medium to provide a gradient in antibody concentration. Cells were washed by FBS free medium once and 1 ml of 1 μg/ml antibody, 10 μg/ml antibody, or FBS free medium was added to each well. After 1.5 h incubation at 37 ^{o}C, 5 μL 1 mg/ml DiI labeled LDL, 10 μL FL NCP particle or plasma sample was added to each well and cells were further incubated for another 4.5 h before analysis by flow cytometry.

10 μL FL NCP (0.2 mg/ml by Chol-SS-pyro) was mixed with 500 μL freshly collected mouse plasma and incubated at 37 ^{o}C for 3 h to obtain equilibrated plasma samples. 40 μL FL NCP was dosed intravenously to Balb/c mice and mouse plasma was collected 3 h post injection to obtain circulating plasma samples. More particles were dosed to mice due to clearance of particles during circulation. 50 μL incubated plasma or circulating plasma was used per well in the study. Signals from the APC channel was recorded as fluorescence from chol-pyro on labeled NCP.

4.4.7 *In vitro* cytotoxicity

Various types of cells were seeded in 96-well plates at a density of 2×10^3 cells per well and allowed to adhere for 24 h. Cells were then treated with different concentrations of CisPtNCP, ZnP/PTX, or CisPt/PTX for another 72 h. Cell viability was detected by MTS assay (Promega, USA) according to the manufacturer's instructions.

4.4.8 *In vivo* antitumor efficacy

Various types of cancer cells were subcutaneously injected into the right flank region of 6-week old mice. 12 days later, mice were intravenously (i.v.) injected with CisPt/PTX at a dose of 0.49 mg Pt/kg and 0.53 mg PTX/kg or with the combination of free CAnP at a dose of 3.9 mg Pt/kg and 8.0 mg PTX/kg once a week. To evaluate the therapeutic efficacy, tumor growth and body weight evolution were monitored. Tumor size was measured with a digital caliper every day. Tumor volumes were calculated as follows: $(\text{width}^2 \times \text{length})/2$. All mice were euthanized when the tumor size of the control group exceeded 2 cm^3 and the excised tumors were photographed and weighed.

4.5 References

1. Ho, G. Y.; Woodward, N.; Coward, J. I. G., Cisplatin versus carboplatin: comparative review of therapeutic management in solid malignancies. *Critical reviews in oncology/hematology* **2016,** *102*, 37-46.

2. Yao, X.; Panichpisal, K.; Kurtzman, N.; Nugent, K., Cisplatin nephrotoxicity: a review. *The American journal of the medical sciences* **2007,** *334* (2), 115-124.

3. Moroso, M. J.; Blair, R. L., A review of cis-platinum ototoxicity. *The Journal of otolaryngology* **1983,** *12* (6), 365.

4. Helson, L.; Okonkwo, E.; Anton, L.; Cvitkovic, E., Cis-platinum ototoxicity. *Clinical toxicology* **1978,** *13* (4), 469-478.

5. Mollman, J. E., Cisplatin neurotoxicity. Mass Medical Soc: 1990.

6. Ries, F.; Klastersky, J., Nephrotoxicity induced by cancer chemotherapy with special emphasis on cisplatin toxicity. *American journal of kidney diseases* **1986,** *8* (5), 368-379.

7. Dentino, M.; Luft, F. C.; Yum, M. N.; Williams, S. D.; Einhorn, L. H., Long term effect of Cis-Diamminedichloride platinum (CDDP) on renal function and structure in man. *Cancer* **1978,** *41* (4), 1274-1281.

8. Ellerby, R. A.; Davis Jr, H. L.; Ansfield, F. J.; Ramirez, G., Phase I clinical trial of combined therapy with 5-FU (NSC 19893) and cis-platinum (II) diaminedichloride (NSC 119875). *Cancer* **1974,** *34* (4), 1005-1010.

9. Gerstman, H. L., Handbook of Clinical Audiology. *JAMA* **1972,** *221* (1), 92-92.

10. Schell, M. J.; McHaney, V. A.; Green, A. A.; Kun, L. E.; Hayes, F. A.; Horowitz, M.; Meyer, W. H., Hearing loss in children and young adults receiving cisplatin with or without prior cranial irradiation. *Journal of Clinical Oncology* **1989,** *7* (6), 754-760.

11. Ozols, R. F.; Young, R. C. In *High-dose cisplatin therapy in ovarian cancer*, 1985; pp 21-30.

12. Litterst, C. L.; Gram, T. E.; Dedrick, R. L.; Leroy, A. F.; Guarino, A. M., Distribution and disposition of platinum following intravenous administration of cis-diamminedichloroplatinum (II)(NSC 119875) to dogs. *Cancer Research* **1976,** *36* (7 Part 1), 2340-2344.

13. Rowinsky, E. K.; Donehower, R. C., Paclitaxel (taxol). *New England Journal of Medicine* **1995,** *332* (15), 1004-1014.

14. Rowinsky, E. K.; Cazenave, L. A.; Donehower, R. C., Taxol: a novel investigational antimicrotubule agent. *JNCI: Journal of the National Cancer Institute* **1990,** *82* (15), 1247-1259.

15. Schiff, P. B.; Fant, J.; Horwitz, S. B., Promotion of microtubule assembly in vitro by taxol. *Nature* **1979,** *277* (5698), 665-667.

16. Schiff, P. B.; Horwitz, S. B., Taxol stabilizes microtubules in mouse fibroblast cells. *Proceedings of the National Academy of Sciences* **1980,** *77* (3), 1561-1565.

17. Gatzemeier, U.; Von Pawel, J.; Gottfried, M.; Velde, G. P. M. t.; Mattson, K.; DeMarinis, F.; Harper, P.; Salvati, F.; Robinet, G.; Lucenti, A., Phase III comparative study of high-dose cisplatin versus a combination of paclitaxel and cisplatin in patients with advanced non–small-cell lung cancer. *Journal of clinical oncology* **2000,** *18* (19), 3390-3399.

18. Roth, A. D.; Maibach, R.; Martinelli, G.; Fazio, N.; Aapro, M. S.; Pagani, O.; Morant, R.; Borner, M. M.; Herrmann, R.; Honegger, H., Docetaxel (Taxotere®)-cisplatin (TC): An effective drug combination in gastric carcinoma. *Annals of oncology* **2000,** *11* (3), 301-306.

19. Kornek, G. V.; Raderer, M.; Schüll, B.; Fiebiger, W.; Gedlicka, C.; Lenauer, A.; Depisch, D.; Schneeweiss, B.; Lang, F.; Scheithauer, W., Effective combination chemotherapy with paclitaxel and cisplatin with or without human granulocyte colony-stimulating factor and/or erythropoietin in patients with advanced gastric cancer. *British journal of cancer* **2002,** *86* (12), 1858-1863.

20. Ilson, D. H.; Ajani, J.; Bhalla, K.; Forastiere, A.; Huang, Y.; Patel, P.; Martin, L.; Donegan, J.; Pazdur, R.; Reed, C., Phase II trial of paclitaxel, fluorouracil, and cisplatin in patients with advanced carcinoma of the esophagus. *Journal of clinical oncology* **1998,** *16* (5), 1826-1834.

21. Nicolaou, K. C.; Riemer, C.; Kerr, M. A.; Rideout, D. R.; Wrasidlo, W. W., Design, synthesis and biological activity of protaxols. *Nature* **1993,** *364* (6436), 464-466.

22. Greenwald, R. B.; Pendri, A.; Bolikal, D.; Gilbert, C. W., Highly water soluble taxol derivatives: 2′-polyethyleneglycol esters as potential prodrugs. *Bioorganic & Medicinal Chemistry Letters* **1994,** *4* (20), 2465-2470.

23. Tarr, B. D.; Yalkowsky, S. H., A new parenteral vehicle for the administration of some poorly water soluble anti-cancer drugs. *PDA Journal of Pharmaceutical Science and Technology* **1987,** *41* (1), 31-33.

24. Weiss, R. B.; Donehower, R. C.; Wiernik, P. H.; Ohnuma, T.; Gralla, R. J.; Trump, D. L.; Baker Jr, J. R.; Van Echo, D. A.; Von Hoff, D. D.; Leyland-Jones, B., Hypersensitivity reactions from taxol. *Journal of clinical oncology* **1990,** *8* (7), 1263-1268.

25. Gelderblom, H.; Verweij, J.; Nooter, K.; Sparreboom, A., Cremophor EL: the drawbacks and advantages of vehicle selection for drug formulation. *European journal of cancer* **2001,** *37* (13), 1590-1598.

26. Waugh, W. N.; Trissel, L. A.; Stella, V. J., Stability, compatibility, and plasticizer extraction of taxol (NSC-125973) injection diluted in infusion solutions and stored in various containers. *American Journal of Hospital Pharmacy* **1991,** *48* (7), 1520-1524.

27. Alkan-Onyuksel, H.; Ramakrishnan, S.; Chai, H.-B.; Pezzuto, J. M., A mixed micellar formulation suitable for the parenteral administration of taxol. *Pharmaceutical research* **1994,** *11* (2), 206-212.

28. Miwa, A.; Ishibe, A.; Nakano, M.; Yamahira, T.; Itai, S.; Jinno, S.; Kawahara, H., Development of novel chitosan derivatives as micellar carriers of taxol. *Pharmaceutical research* **1998,** *15* (12), 1844-1850.

29. Ceruti, M.; Crosasso, P.; Brusa, P.; Arpicco, S.; Dosio, F.; Cattel, L., Preparation, characterization, cytotoxicity and pharmacokinetics of liposomes containing water-soluble prodrugs of paclitaxel. *Journal of controlled release* **2000,** *63* (1-2), 141-153.

30. Crosasso, P.; Ceruti, M.; Brusa, P.; Arpicco, S.; Dosio, F.; Cattel, L., Preparation, characterization and properties of sterically stabilized paclitaxel-containing liposomes. *Journal of Controlled Release* **2000,** *63* (1-2), 19-30.

31. Singla, A. K.; Garg, A.; Aggarwal, D., Paclitaxel and its formulations. *International journal of pharmaceutics* **2002,** *235* (1-2), 179-192.

32. Petrelli, F.; Borgonovo, K.; Barni, S., Targeted delivery for breast cancer therapy: the history of nanoparticle-albumin-bound paclitaxel. *Expert opinion on pharmacotherapy* **2010,** *11* (8), 1413-1432.

33. Ma, P.; Mumper, R. J., Paclitaxel nano-delivery systems: a comprehensive review. *Journal of nanomedicine & nanotechnology* **2013,** *4* (2), 1000164.

34. Deeks, E. D., Pembrolizumab: a review in advanced melanoma. *Drugs* **2016,** *76* (3), 375-386.

35. Schleicher, E.; Wieland, O. H., Kinetic analysis of glycation as a tool for assessing the half-life of proteins. *Biochimica et Biophysica Acta (BBA)-General Subjects* **1986,** *884* (1), 199-205.

36. Franco, R. S., Measurement of red cell lifespan and aging. *Transfusion medicine and hemotherapy* **2012,** *39* (5), 302-307.

37. Rudman, D.; Hollins, B.; Bixler, T. J.; Mosteller, R. C., Transport of drugs, hormones and fatty acids in lipemic serum. *Journal of Pharmacology and Experimental Therapeutics* **1972,** *180* (3), 797-810.

38. Van der Vies, J., Drug-delivery systems and the biological activity of steroids. *Journal of Steroid Biochemistry* **1975,** *6* (3-4), 215-220.

39. Brown, M. S.; Kovanen, P. T.; Goldstein, J. L., Regulation of plasma cholesterol by lipoprotein receptors. *Science* **1981,** *212* (4495), 628-635.

40. Bilheimer, D. W.; Eisenberg, S.; Levy, R. I., The metabolism of very low density lipoprotein proteins I. Preliminary in vitro and in vivo observations. *Biochimica et Biophysica Acta (BBA)-Lipids and Lipid Metabolism* **1972,** *260* (2), 212-221.

41. Sigurdsson, G.; Nicoll, A.; Lewis, B., Conversion of very low density lipoprotein to low density lipoprotein. A metabolic study of apolipoprotein B kinetics in human subjects. *The Journal of clinical investigation* **1975,** *56* (6), 1481-1490.

42. Pattnaik, N. M.; Montes, A.; Hughes, L. B.; Zilversmit, D. B., Cholesteryl ester exchange protein in human plasma isolation and characterization. *Biochimica et Biophysica Acta (BBA)-Lipids and Lipid Metabolism* **1978,** *530* (3), 428-438.

43. Chajek, T.; Fielding, C. J., Isolation and characterization of a human serum cholesteryl ester transfer protein. *Proceedings of the National Academy of Sciences* **1978,** *75* (7), 3445-3449.

44. Firestone, R. A., Low-density lipoprotein as a vehicle for targeting antitumor compounds to cancer cells. *Bioconjugate chemistry* **1994,** *5* (2), 105-113.

45. Lundberg, B. O.; Suominen, L., Preparation of biologically active analogs of serum low density lipoprotein. *Journal of lipid research* **1984,** *25* (6), 550-558.

46. Dubowchik, G. M.; Firestone, R. A., Improved cytotoxicity of antitumor compounds deliverable by the LDL pathway. *Bioconjugate chemistry* **1995,** *6* (4), 427-439.

47. Chu, A. C. Y.; Tsang, S. Y.; Lo, E. H. K.; Fung, K. P., Low density lipoprotein as a targeted carrier for doxorubicin in nude mice bearing human hepatoma HepG2 cells. *Life sciences* **2001,** *70* (5), 591-601.

48. Masquelier, M.; Vitols, S.; Peterson, C., Low-density lipoprotein as a carrier of antitumoral drugs: in vivo fate of drug-human low-density lipoprotein complexes in mice. *Cancer research* **1986,** *46* (8), 3842-3847.

49. Ernsting, M. J.; Murakami, M.; Undzys, E.; Aman, A.; Press, B.; Li, S.-D., A docetaxel-carboxymethylcellulose nanoparticle outperforms the approved taxane nanoformulation, Abraxane, in mouse tumor models with significant control of metastases. *Journal of controlled release* **2012,** *162* (3), 575-581.

50. Park, J.; Park, J. E.; Hedrick, V. E.; Wood, K. V.; Bonham, C.; Lee, W.; Yeo, Y., A Comparative In Vivo Study of Albumin-Coated Paclitaxel Nanocrystals and Abraxane. *Small* **2018,** *14* (16), 1703670.

51. Soundararajan, A.; Bao, A.; Phillips, W. T.; Perez Iii, R.; Goins, B. A., [186Re] Liposomal doxorubicin (Doxil): in vitro stability, pharmacokinetics, imaging and biodistribution in a head and neck squamous cell carcinoma xenograft model. *Nuclear medicine and biology* **2009,** *36* (5), 515-524.

52. Working, P. K.; Newman, M. S.; Huang, S. K.; Mayhew, E.; Vaage, J.; Lasic, D. D., Pharmacokinetics, biodistribution and therapeutic efficacy of doxorubicin encapsulated in Stealth® liposomes (Doxil®). *Journal of Liposome Research* **1994,** *4* (1), 667-687.

53. Ponty, E.; Carton, M.; Soula, G.; Favre, G.; Benaniba, R.; Boneu, A.; Lucot, H., Biodistribution study of 99mTc-labeled LDL in B16-melanoma-bearing mice. Visualization of a preferential uptake by the tumor. *International journal of cancer* **1993,** *54* (3), 411-417.

54. Hay, R. V.; Pottenger, L. A.; Reingold, A. L.; Getz, G. S.; Wissler, R. W., Degradation of I125-labelled serum low density lipoprotein in normal and estrogen-treated male rats. *Biochemical and biophysical research communications* **1971,** *44* (6), 1471-1477.

55. Mahley, R. W.; Weisgraber, K. H.; Melchior, G. W.; Innerarity, T. L.; Holcombe, K. S., Inhibition of receptor-mediated clearance of lysine and arginine modified lipoproteins from the plasma of rats and monkeys. *Proceedings of the National Academy of Sciences* **1980,** *77* (1), 225-229.

56. Vallabhajosula, S.; Paidi, M.; Badimon, J. J.; Le, N.-A.; Goldsmith, S. J.; Fuster, V.; Ginsberg, H. N., Radiotracers for low density lipoprotein biodistribution studies in vivo: technetium-99m low density lipoprotein versus radioiodinated low density lipoprotein preparations. *Journal of nuclear medicine* **1988,** *29* (7), 1237-1245.

57. He, C.; Duan, X.; Guo, N.; Chan, C.; Poon, C.; Weichselbaum, R. R.; Lin, W., Core-shell nanoscale coordination polymers combine chemotherapy and photodynamic therapy to potentiate checkpoint blockade cancer immunotherapy. *Nature communications* **2016,** *7* (1), 1-12.

Chapter 5. Lysosome-Targeting Self-assembled Nanophotosensitizers for Photodynamic Therapy

5.1 Introduction

As acidic organelles, lysosomes play vital roles in regulating cell homeostasis by digesting extracellular materials uptaken via endocytosis and intracellular materials from autophagy.[1] Disruption of lysosomal functions via lysosomal membrane permeabilization (LMP) can efficiently cause cell death via apoptotic and necrotic pathways.[2] For example, cathepsins and other enzymes released from disrupted lysosomes trigger cell death by either directly degrading antiapoptotic proteins such as Bcl-2 family proteins or turning on apoptotic signaling pathways.[3] LMP can be induced by a variety of methods, including disruption of the lysosomal membrane by detergents, osmotic membrane lysis, and regulation by caspases.[2]

Among all of the methods for LMP induction, photodynamic therapy (PDT) has been explored as a potential strategy for cancer treatment. As a local therapy, PDT uses light irradiation to excite photosensitizers (PSs) in tumor cells. PSs then transfer energy to molecular oxygen to generate reactive oxygen species (ROS), particularly singlet oxygen ($^1O_2$), to damage nearby molecules and organelles.[4] Several lysosome-targeting PSs were studied as anticancer LMP inducers in recent years. Ir^{III} complexes,[5] Ru^{II},[6-8] and some organic PSs[9-10] showed lysosomal localization and *in vitro* efficacy by PDT alone or in combination with other anticancer approaches. Despite their *in vitro* efficacy, only a few of them were studied *in vivo* via intratumoral injection.[5, 7] The *in vivo* efficacies of these lysosome-targeting PSs are limited by their suboptimal pharmacokinetic and pharmacodynamic properties.

Another drawback for existing lysosome-targeting PSs is their leakage from lysosomes and redistribution to the cytoplasm or nucleus caused by PDT-induced LMP.[11-12] Cancer cells can recover from this kind of lysosomal disruption by reducing lysosome exposure towards photochemical damage.[13] The PDT efficacy can be substantially enhanced if lysosome-targeting PSs do not leak from lysosomes during the whole light irradiation process, which can cause continuous LMP and irreparable damage to lysosomes.

In this chapter, we report the synthesis of a novel BODIPY based lysosome-targeting organic photosensitizer **QAS** (**Figure 5.1**). The amphiphilic structure of **QAS** can self-assemble into nanoparticles in an aqueous solution. We show that self-assembled **QAS** can accumulate in lysosomes of cancer cells and stick on lysosomes during light irradiation. Self-assembled **QAS** also showed promising pharmacokinetic and pharmacodynamic properties which allow for great *in vivo* efficacy and potential clinical applications.

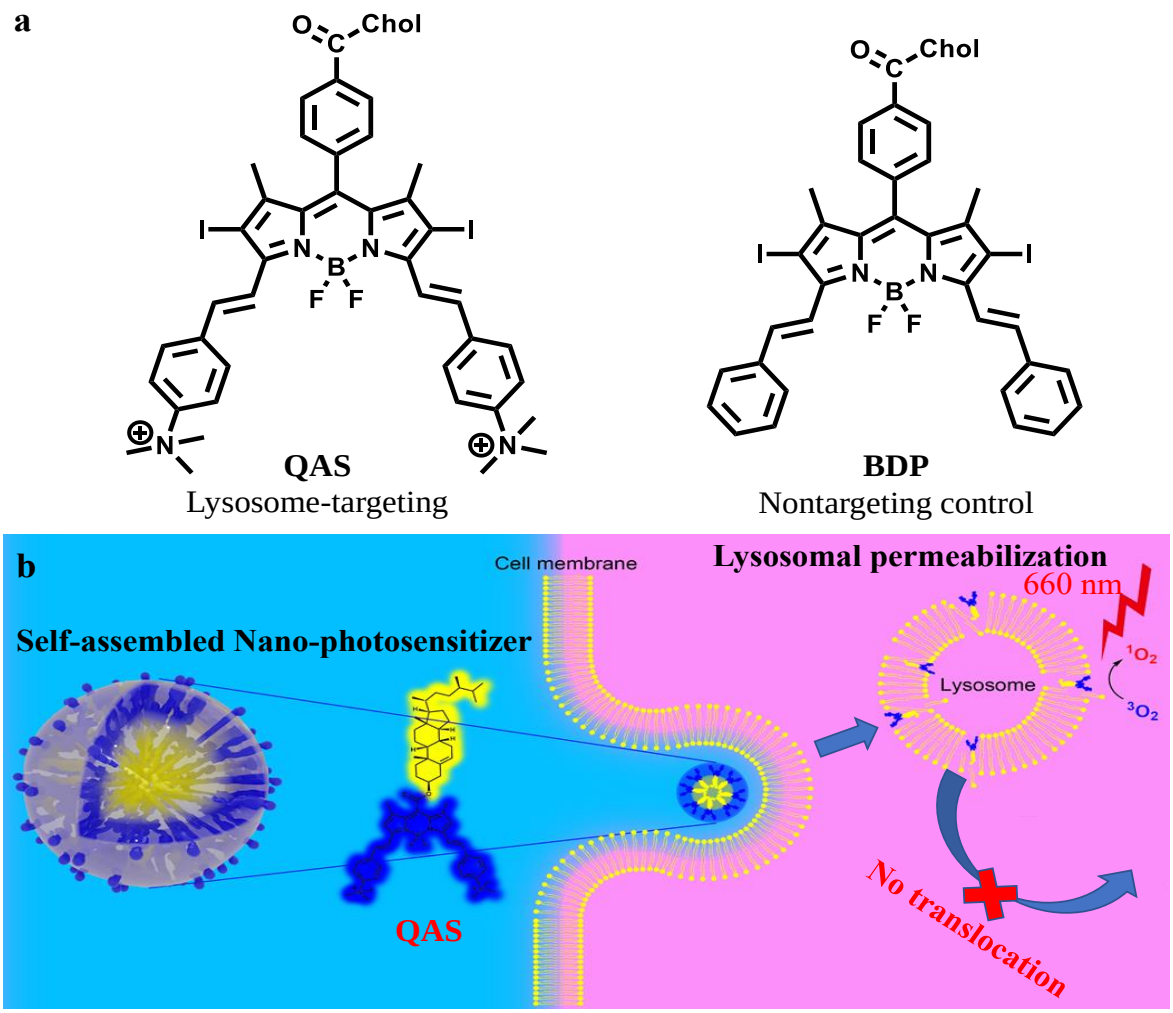

Figure 5.1. (a) Molecular structures of **QAS** and **BDP** (Chol = cholesterol). (b) Schematic showing the self-assembly of QAS to an nPS and attachment of QAS to lysosomal membranes for PDT induced LMP.

5.2 Results and Discussion

5.2.1 Synthesis and characterization of photosensitizers and nanoparticles

Two new PSs, QAS and BDP, were constructed based on the well-studied boron-dipyrromethene (BODIPY) scaffold through an aldol-type condensation with

benzaldehydes. BODIPY derivatives have several ideal properties for PDT, including high molar extinction coefficients, low dark toxicity, resistance to photobleaching, and chemical stability in biological environments.[14] Heavy atom substitution of BODIPY significantly increases $^1O_2$ yield by enhancing intersystem crossing via spin-orbit coupling,[15] while enlargement of conjugation systems red-shifts the absorption toward the near-infrared (NIR) region which has deeper tissue penetration.[16]

We have recently shown the noncovalent insertion of cholesterol-based prodrugs into phospholipid bilayers for drug delivery.[17-18] We hypothesized that cholesterol could act as an anchor to insert cholesterol-linked PSs into lipid bilayers on lysosomes. BODIPY was first iodinated and coupled to cholesterol via carbodiimidazole-mediated esterification. This chol-BODIPY intermediate was conjugated with benzaldehyde to form **BDP** or 4-dimethylaminobenzaldehyde followed by quaternization with methyl iodide to form **QAS**. **BDP** and **QAS** showed similar UV-Vis spectra with absorption maxima at ~650 nm (**Figure 5-2** a) and displayed similar intense fluorescence at ~660 nm when excited at 640 nm (**Figure 5-4** a).

The addition of 1 mL of 0.28 mM **QAS** in DMSO into 17 mL phosphate buffered saline (PBS) afforded self-assembled nanoparticles of **QAS**, **QAS-nPS**, with a Z-averaged diameter of 130 nm and a polydispersity index (PDI) of 0.19. The surface charge of **QAS-nPS** was +24 mV in water, suggesting the formation of nanoparticles with cholesterol groups interdigitating with each other in the middle and positively charged ammonium groups on the surface. Under the same conditions, **BDP** aggregated into larger particles of **BDP-nPS** with a Z-averaged size of 460 nm, a PDI of 0.27, and a surface charge of +0.03 mV (**Figure 5-2** b). **QAS-nPS** was stable with no change in size

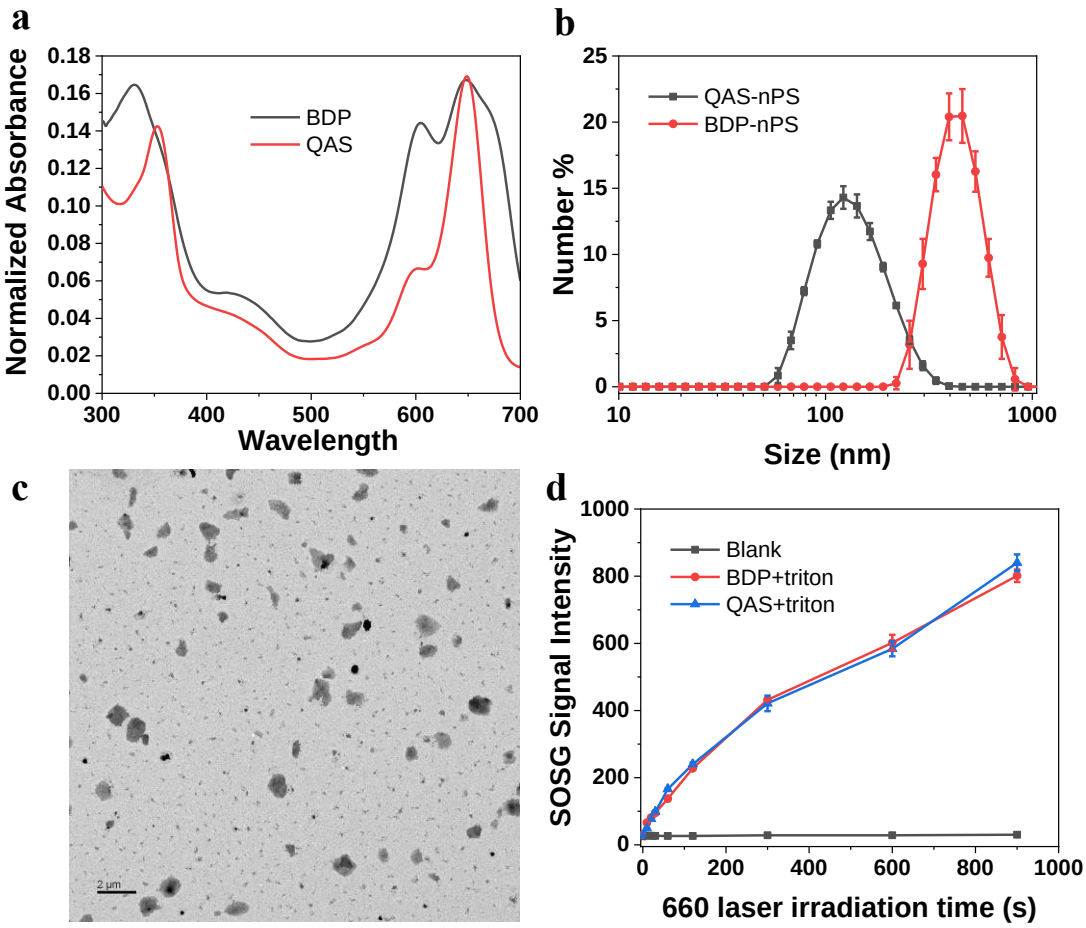

Figure 5-2. (a) Normalized UV-Vis spectra of QAS and BDP. (b) Size distribution of self-assembled QAS-nPS and BDP-nPS. (c) TEM image of QAS-nPS. (d) SOSG fluorescence signals of 1.25 μM QAS and BDP in PBS solution with 0.5% (V/V) Triton X-100 upon irradiation at 660 nm. n = 3.

or PDI at 25 °C for 48 h (**Figure 5-3**). The size of **QAS-nPS** is within the range for enhanced tumor accumulation by avoiding renal clearance and penetrating the leaky tumor vasculatures. Their formation was also confirmed through the characterization of TEM (**Figure 5-2** c).

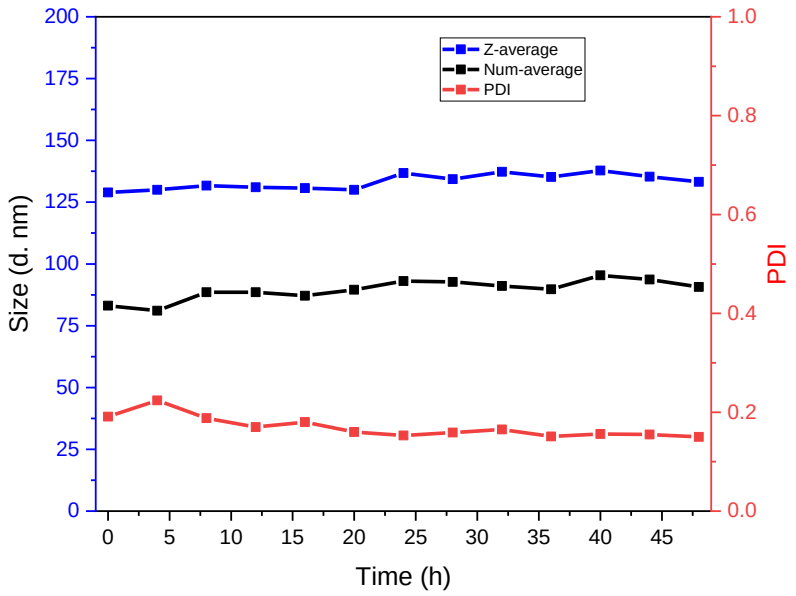

Figure 5-3. Stability test of **QAS-nPS** at 25 °C in DMSO/PBS (v/v, 3:50).

5.2.2 Cellular uptake and lysosome targeting and disruption

As shown in **Figure 5-4** b and c, **QAS** and **BDP** showed similar uptake in murine colon cancer CT26 cells. We next studied the subcellular localization of **QAS** by confocal microscopy. CT26 cells were treated with **QAS** and then stained using lysotracker and mitotracker. Most **QAS** signal colocalized with lysotracker but very little **QAS** signal colocalized with mitotracker (**Figure 5-5**), suggesting that **QAS** targets lysosomes after cell uptake due to its amphiphilic nature.

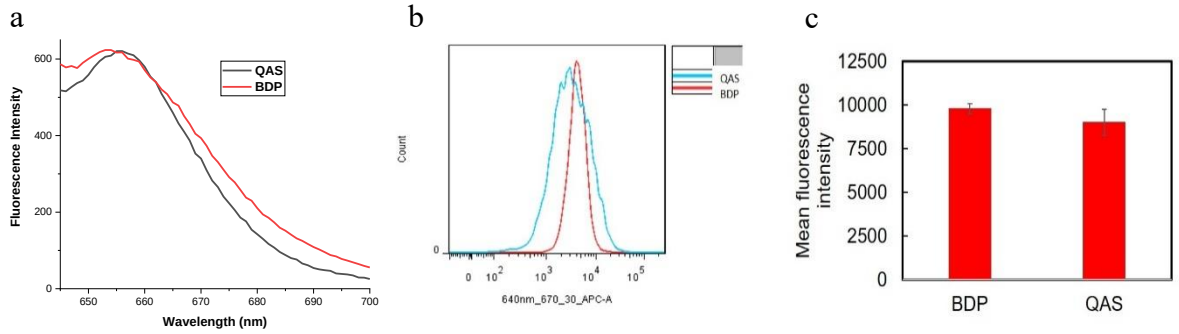

Figure 5-4. (a) Normalized fluorescence spectrum of **QAS** and **BDP** in DMSO/PBS (v/v, 3:50) when excited at 640 nm. (b) and (c) cellular uptake of **QAS** and **BDP** measured by flow cytometry.

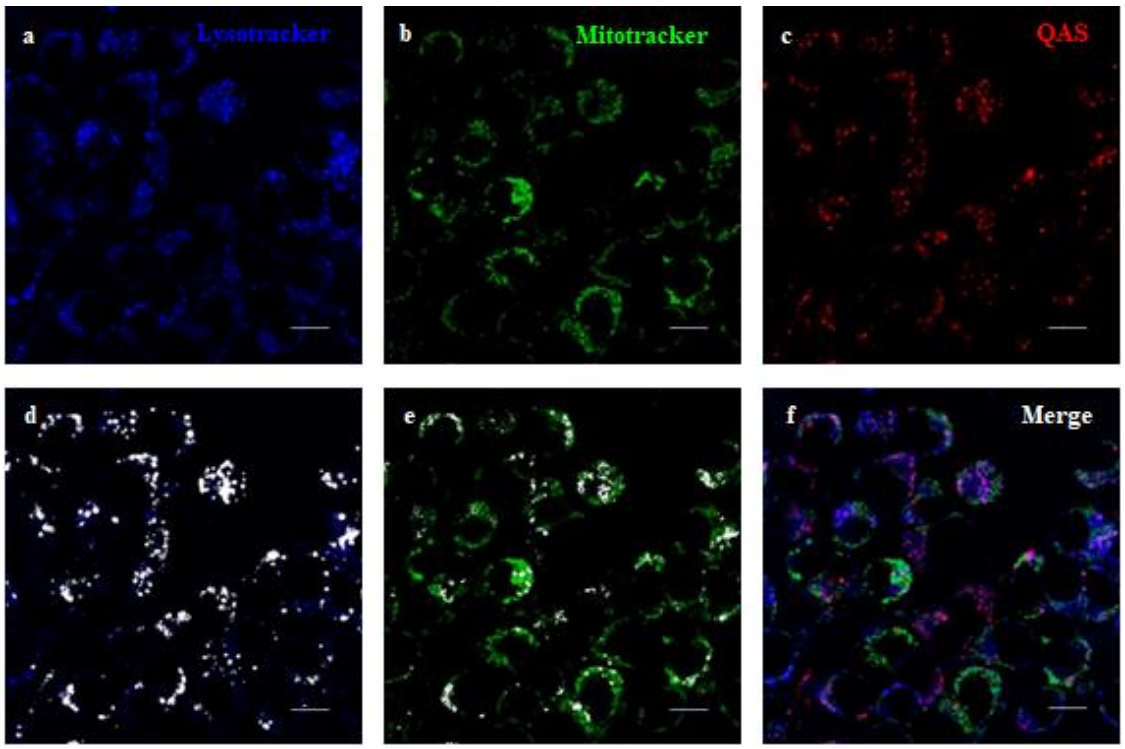

Figure 5-5. Confocal images showing (a) lysosome, (b) mitochondria, (c) **QAS**, (d) colocalization between lysosome and **QAS** (white), (e) colocalization between mitochondria and **QAS** (white) and (f) merged color image where magenta represents the colocalization between lysosome and **QAS** while green shows mitochondria. Scale bar: 10 μm.

The colocalization of **QAS** and lysotracker prompted us to examine LMP by **QAS**-mediated PDT. Acridine orange (AO) labels acidic organelles by emitting orange-red fluorescence in acidic conditions but green fluorescence at physiological pH upon 488 nm light excitation. AO is widely used to study LMP based on the orange-red fluorescence; LMP disrupts lysosomes and hence increase local pH, which turns off orange-red fluorescence from AO.[12] **QAS** or **BDP** treated cells were stained using AO and analyzed

by confocal microscopy and flow cytometry (**Figure 5-6**). Here pseudocolor is used for better illustration: green fluorescence from normal AO is shown in blue, orange-red fluorescence from lysosomes is shown in green, and PS is shown in red. **QAS**- or **BDP**-treated cells were first stained with AO. Before light irradiation, lysosomes were stained by AO and there was 84.6% colocalization between AO and **QAS** (**Figure 5-6** a). After light irradiation, the orange-red AO fluorescence almost completely disappeared for cells treated with 10 nM **QAS**, leaving 27.1% colocalization between AO and **QAS**. This colocalization factor decreased to 11.3% and 0.14% for cells treated with 40 and 80 nM **QAS**, respectively. Furthermore, **QAS** signal persisted in lysosomes after light irradiation, suggesting that QAS did not redistribute to the cytoplasm during PDT to give the maximum irreparable damage to lysosomes. We believe cholesterol and cationic

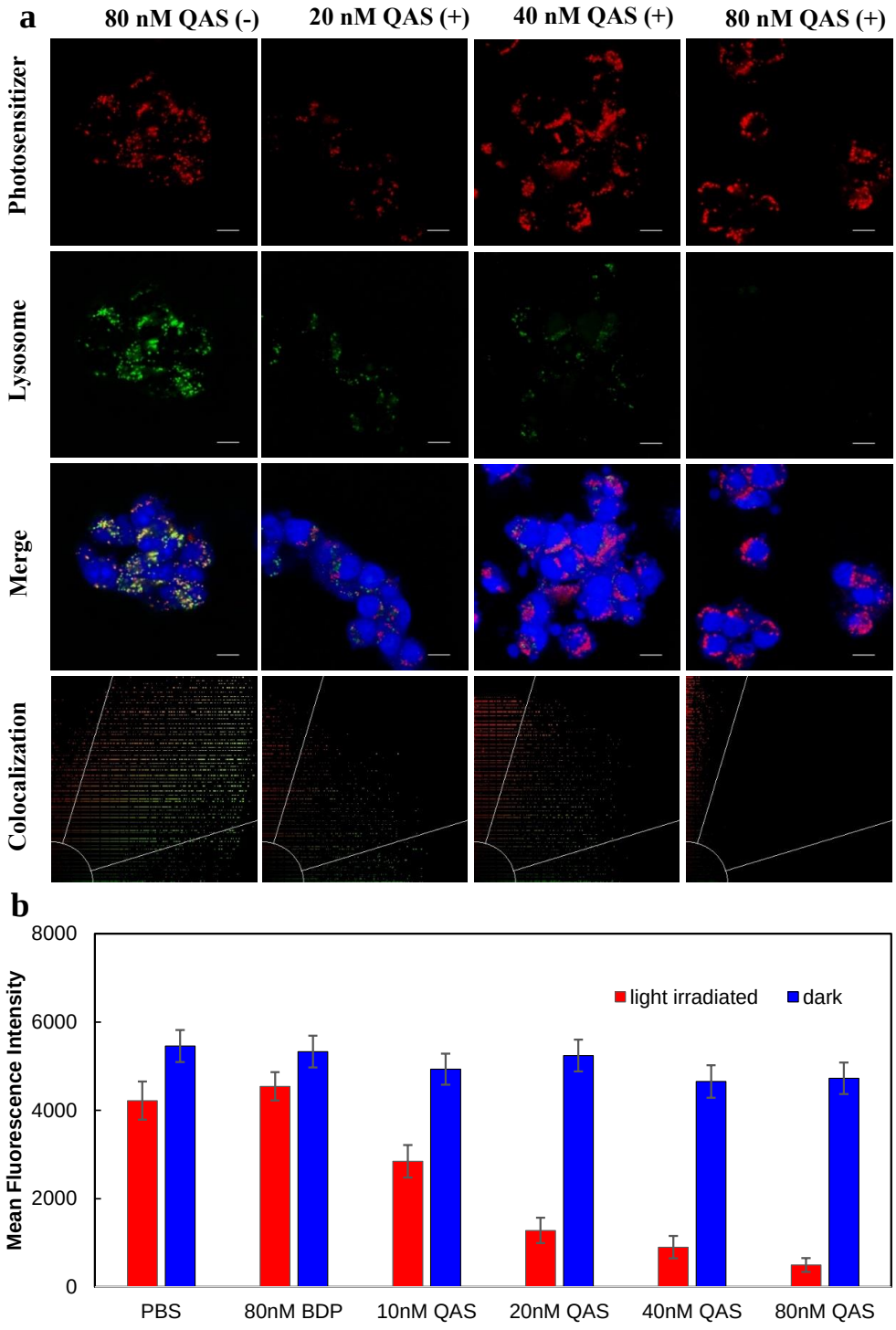

Figure 5-6. (a) Lysosome targeting and disruption shown by AO staining. (b) Quantitative analysis of AO staining result by flow cytometry.

ammonium groups of **QAS** strongly interact with hydrophobic interior and anionic phosphate head groups of the lysosomal membrane, respectively, to prevent **QAS** leakage during lysosomal swelling. To our knowledge, **QAS** is the first lysosome-targeting PS with negligible leakage from the lysosomal membrane after PDT.

5.2.3 Singlet oxygen and ROS generation

We tested $^1O_2$ generation by **QAS** and **BDP** in PBS containing 0.5% triton X-100 using the singlet oxygen generation green (SOSG) kit. **QAS** and **BDP** generated comparable amounts of $^1O_2$ upon irradiation at 660 nm with similarly high $^1O_2$ quantum yields (**Figure 5-2** d). The continuous increase of $^1O_2$ signals during 15 min light irradiation also demonstrated the photostability of **QAS** and **BDP**. $^1O_2$ generation by **QAS** and **BDP** was also studied *in vitro*. CT26 cells were incubated with PSs and SOSG before light irradiation. The green fluorescence signal from SOSG was analyzed using flow cytometry and confocal imaging. Surprisingly, **QAS** showed much higher $^1O_2$ generation than **BDP** in CT26 cells (**Figure 5-7** a), likely because $^1O_2$ generated by non-targeted **BDP** was easily eliminated by redox-active enzymes and other biomolecules in the cytoplasm.

LMP can cause cathepsin release, which may further damage mitochondria and increase cellular ROS level. The total ROS level in cells was studied by H_2DCF through CLSM imaging and flow cytometry (**Figure 5-7** b). After light irradiation, the green fluorescence signal from oxidized H_2DCF appeared. Although both PSs elevated ROS levels after light irradiation, **QAS** showed a much higher level of ROS than **BDP**. This result suggests that disruption of lysosomes by **QAS** triggers downstream events in addition to generating $^1O_2$ to damage cells.

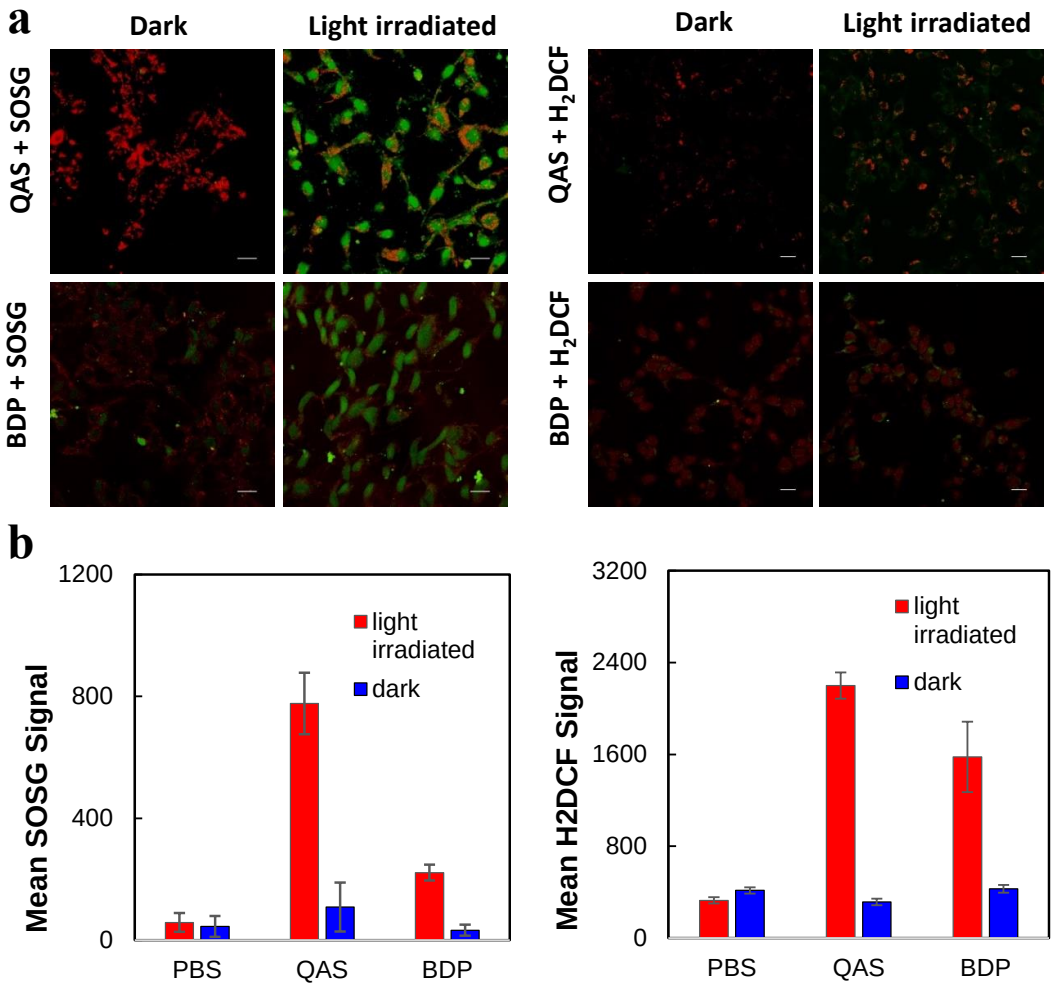

Figure 5-7. (a) CLSM images and (b) flow cytometry analysis results of singlet oxygen (left) and ROS (right) generation by **QAS** and **BDP**-treated cell groups, scale bar = 25 m. 15 min irradiation at 660 nm (54 J/cm^2, 60 mW/cm^2).

5.2.4 *In vitro* toxicity

Despite their similar $^1O_2$ generation in PBS, **QAS** and **BDP** showed a very large difference in cytotoxicity by MTS assay (**Figure 5-8** a). **QAS** showed an IC_{50} of 37 nM, nearly 100 times smaller than that of **BDP** (3.6 μM). Cell apoptosis/necrosis was

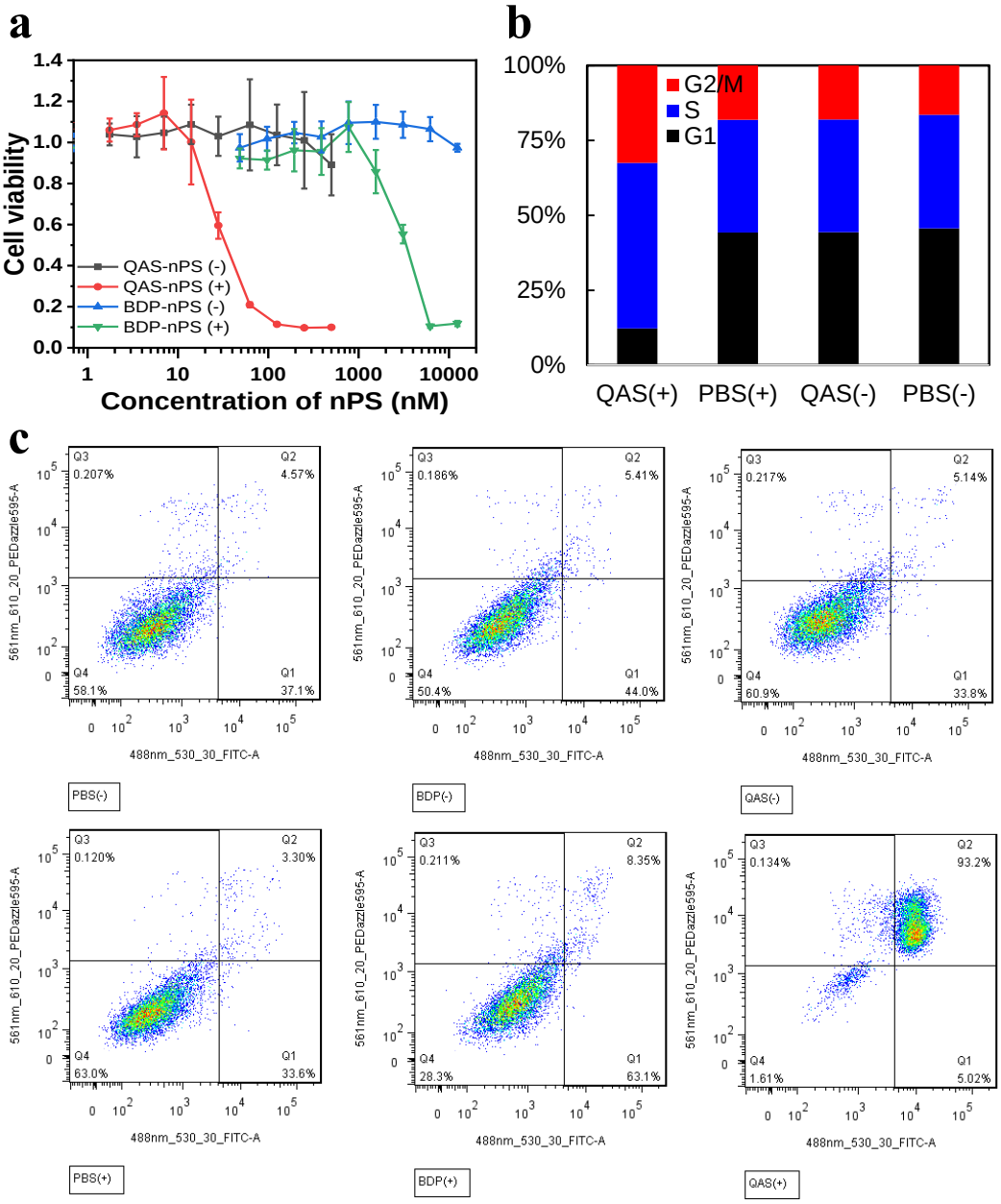

Figure 5-8. (a) Cytotoxicity of **QAS** and **BDP** by MTS assay. (b) Cell cycle study. (c) Apoptosis/necrosis study by annexin V/PI staining. (+) and (-) represent cells with or without 15 min irradiation at 660 nm (54 J/cm^2, 60 mW/cm^2).

confirmed by Annexin V/PI staining assay. When treated with 40 nM **QAS** and light irradiation, 93.2% of cells were in the late apoptosis/necrosis stage while the same concentration of **BDP** only showed 8.4% cells in late apoptosis/necrosis (**Figure 5-8** c). These results show that a lysosome-targeting PS with a strong affinity to the lysosomal membrane can significantly increase its cytotoxicity.

We performed cell cycle analysis using the cell cycle kit (**Figure 5-8** b). Cells treated with **QAS** and light irradiation increased percentages of G2/M and S phases from 22% and 45% (for PBS) to 30% and 51%, respectively. The arrest in cell cycle suggests that **QAS** may trigger cell death via different mechanisms such as endoplasmic reticulum (ER) stress caused by mitochondrial dysfunction as a downstream event of LMP and cathepsin release.

5.2.5 Biodistribution

Blood circulation and biodistribution of **QAS-nPS** were examined on CT26 tumor-bearing mice. After intravenously dosed with 0.2 mg **QAS** in DMSO/PBS (v/v, 1:100), mice were sacrificed at 1 h, 3 h, 8 h, and 24 h post injection. Organs and plasma of these mice were imaged using IVIS (**Figure 5-9** a). **QAS** did not show accumulation in hearts and exhibited low accumulation in kidneys for a few hours, indicating that **QAS-nPS** was not significantly cleared through kidney. Lungs, spleens, and livers showed some **QAS** accumulation in the first 8 hours, but the **QAS** signal was cleared at 24 h post injection. On the contrary, although tumor did not show significant **QAS** signal at the beginning, the concentration of **QAS** gradually increased to reach a high level at 24 h post injection. **QAS-nPS** thus shows a good passive targeting effect towards tumor tissues to minimize general toxicity to normal tissues.

5.2.6 *In vivo* efficacy

CT26 tumor-bearing mice were intravenously injected with 10 mg/kg **QAS-nPS** when the tumors reached 100 mm^3 on day 7 post tumor inoculation. The tumors were irradiated using 670 nm LED at 100 mW/cm^2 for 30 min (180 J/cm^2) 24 h post injection. The treatment was repeated on day 9 and day 11. Tumor size of each mouse was monitored (**Figure 5-9** b). Surprisingly, 3 out of 6 treated mice in **QAS-nPS(+)** group (+ denotes light irradiation) were completely cured after the treatment and the rest also showed significant shrinkage of tumors, while **QAS** treated mice without light irradiation did not show efficacy (**Figure 5-9** d). **BDP** PDT group showed tumor growth inhibition, but not nearly as significant as **QAS**. It is likely that the hydrophobic nature of **BDP** leads to poor pharmacokinetic property *in vivo*. The nontargeted PDT by **BDP** also cannot trigger specific and lethal cell damage. The tumor weight of the **QAS-nPS(+)** group was also much smaller than other groups, which is consistent with the trend observed for the tumor volumes (**Figure 5-9** e). Furthermore, all treatment groups did not show body weight loss during the treatment, suggesting that the treatment did not cause severe systemic toxicity (**Figure 5-9** c).

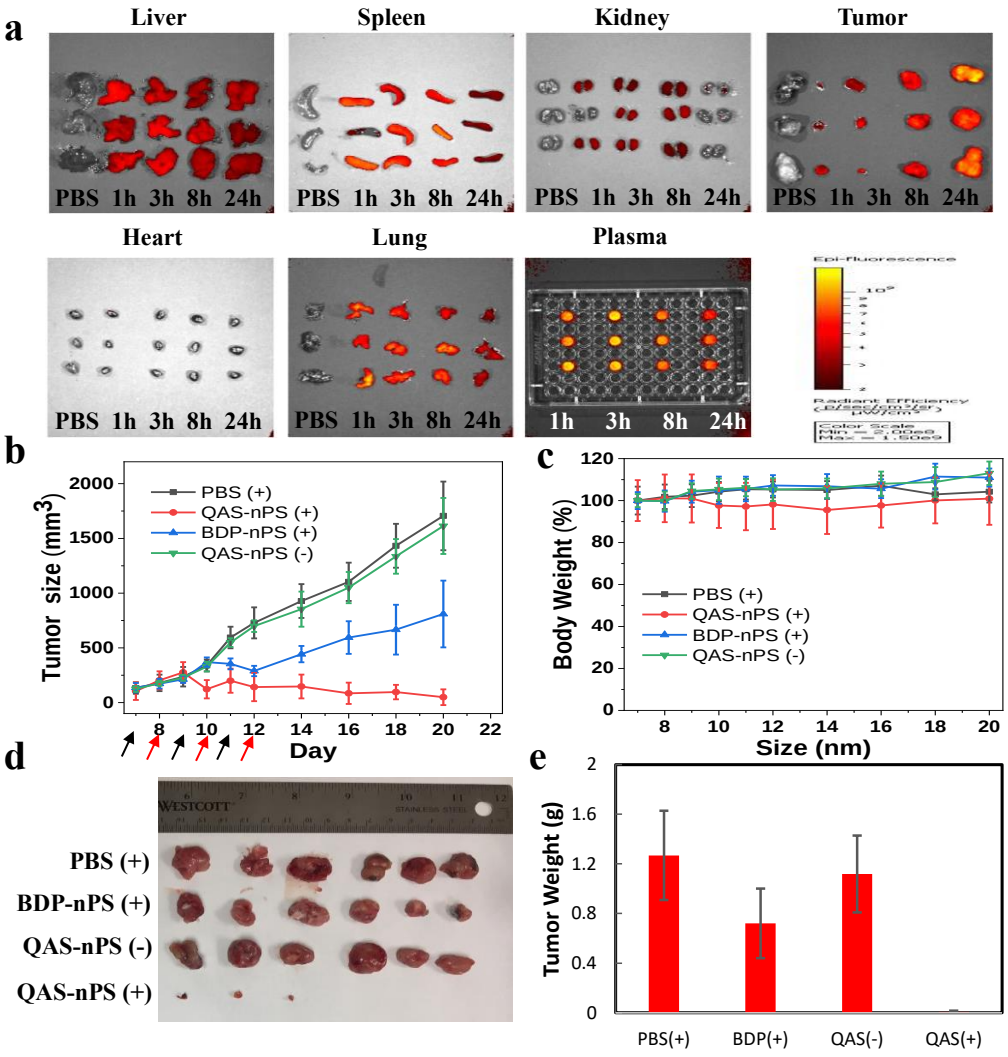

Figure 5-9. (a) Biodistribution of **QAS** micelle by IV-IS excited at 650 nm. (b) CT 26 tumor growth curve (n = 6), mice were dosed on day 7, 9, 11, and irradiated on day 8, 10, 12. (c) Body weight of mice in each group. (d) Image of tumors at day 20. (e) Weight of tumor at day 20. (+) and (-) represent mice with or without 30 min irradiation at 670 nm (180 J/cm^2, 100 mW/cm^2).

5.3 Conclusion

We synthesized a self-assembled BODIPY-based photosensitizer **QAS** as the first specific lysosomal targeting photosensitizer that has no leakage during the whole PDT process. **QAS** also self-assembled into a nanophotosensitizer in aqueous solution due to its amphiphilic nature. In addition to generating singlet oxygen, **QAS** causes LMP continuously at nanomolar concentrations. This unique property makes **QAS** a much more phototoxic photosensitizer than the nontargeting counterpart, with the ability to trigger cell apoptosis and necrosis at a very low concentration. **QAS** shows great PDT treatment efficacy on CT26 tumor model without causing systemic toxicity, providing a large therapeutic window for cancer treatments. **QAS** illustrates the potential to combine molecular design and nanostructures for the development of lysosome-targeting photosensitizers for clinical applications.

5.4 Experimental

5.4.1 Synthesis of photosensitizers

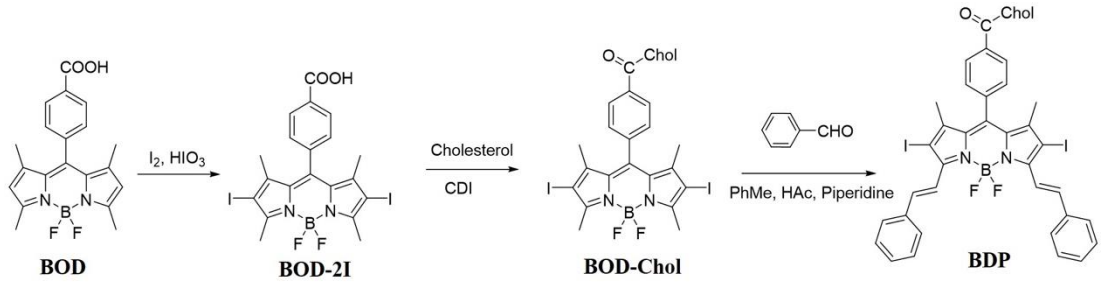

Figure 5-10. Synthesis route of **BDP**

Preparation of BOD-2I.

4-(5,5-difluoro-1,3,7,9-tetramethyl-5H-4l4,5l4-dipyrrolo[1,2-c:2',1'-f][1,3,2]diazaborinin-10-yl)benzoic acid (**BOD**) was synthesized by the previously reported method.[19] To a solution of BOD (543 mg, 1.48 mmol) and iodine (980 mg, 3.70 mmol) in 10 mL EtOH was added 5.5 mL iodic acid (543 mg, 2.96 mmol) in aqueous solution. The mixture was the stirred at 60 ^{o}C for 1 h. After cooling to room temperature, saturated $Na_2S_2O_3$ solution was added and the product was extracted with CH_2Cl_2. The CH_2Cl_2 solution was evaporated and the residue was purified by silica gel column chromatography [CH_2Cl_2/ethyl acetate/HAc = 10:1:0.02, (v/v)] to afford 4-(5,5-difluoro-2,8-diiodo-1,3,7,9-tetramethyl-5H-4l4,5l4-dipyrrolo[1,2-c:2',1'-f][1,3,2]diazaborinin-10-yl)benzoic acid (**BOD-2I**) as a red solid (916 mg, 100% yield). ^{1}H-NMR (500MHz, $CDCl_3$): δ 1.39 (s, 6H), 2.66 (s, 6H), 7.43 (d, 2H), 8.28 (d, 2H).

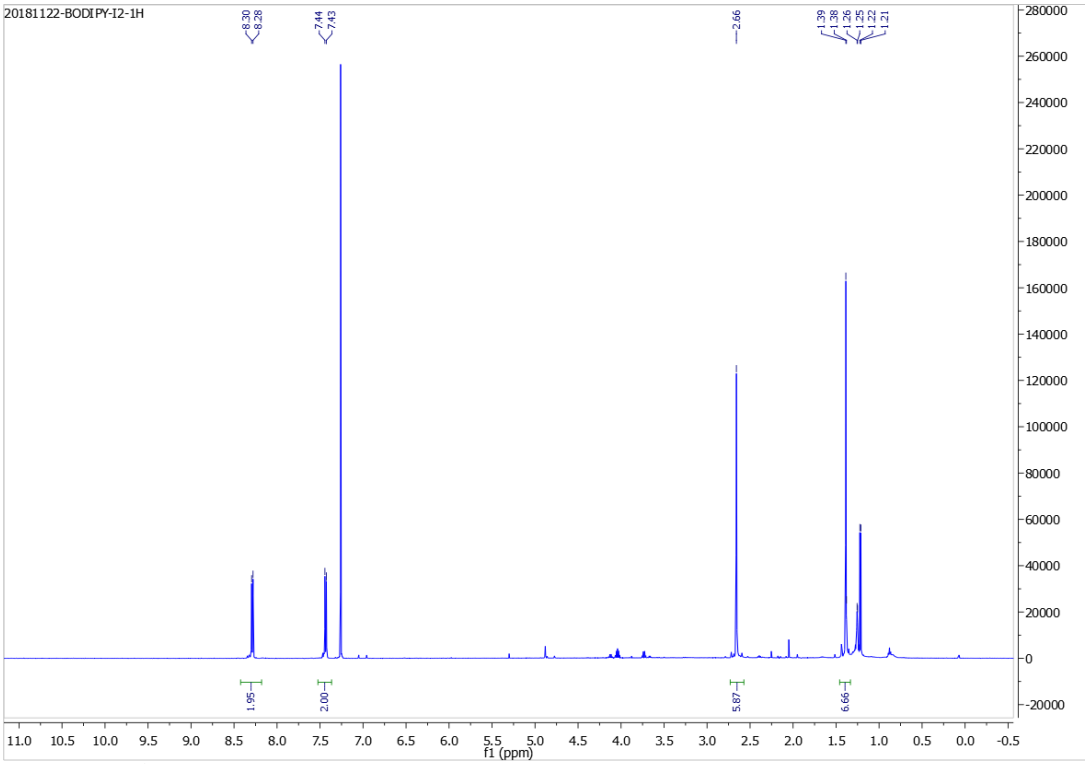

Figure 5-11. ^{1}H-NMR spectrum of **BOD-2I**.

Preparation of Cholest-5-en-3-ol (3β) 4-(5,5-difluoro-2,8-diiodo-1,3,7,9-tetramethyl-5H-4l4,5l4-dipyrrolo[1,2-c:2',1'-f][1,3,2]diazaborinin-10-yl)benzoate (**BOD-Chol**).

Carbonyldiimidazole (CDI) (71 mg, 0.44 mmol) was added to a solution of **BOD-2I** (180 mg, 0.29 mmol) in 10 mL of dry THF under continuous stirring at room temperature. The mixture was stirred at room temperature for 1 h. To this mixture under continuous stirring was then added a solution of cholesterol (170 mg, 0.44 mmol) and NaH (40 mg, 1.67 mmol) in 10 mL dry THF over 20 min at room temperature through a 0.2 µm polytetrafluoroethylene (PTFE) syringe driven filter. The mixture solution was heated at 80 ^{o}C overnight. After removal of the solvents, the dry pink solid was purified by silica gel column chromatography [hexanes/ethyl acetate, 20:1 (v/v)] to afford BOD-Chol as a red solid (229 mg, 80% yield). ^{1}H-NMR (500MHz, $CDCl_3$): δ 0.70 (s, 3H), 0.85 (q, 6H), 0.92 (d, 3H), 1.02 (m, 2H), 1.09 (s, 3H), 1.33 (s, 2H), 1.37 (s, 8H), 1.45 (m, 2H), 1.52 (m, 4H), 1.59 (m, 5H), 1.83 (m, 3H), 1.97 (m, 2H), 2.04 (m, 3H), 2.51 (d, 2H), 2.65 (s, 6H), 4.91 (m, 1H), 5.44 (d, 1H), 7.36 (d, 2H), 8.20 (d, 2H).

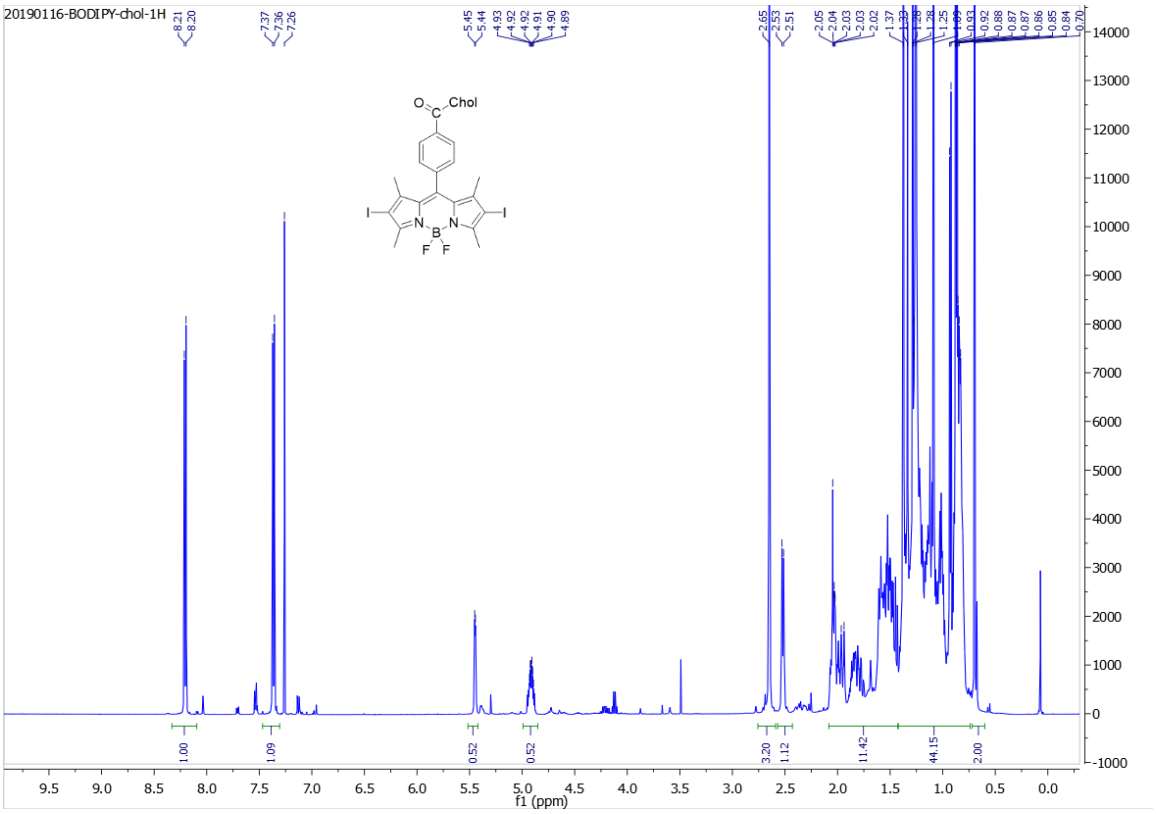

Figure 5-12. ^{1}H-NMR spectrum of BOD-Chol.

Preparation of Cholest-5-en-3-ol (3β) 4-(5,5-difluoro-2,8-diiodo-1,9-dimethyl-3,7-di((E)-styryl)-5H-4l4,5l4-dipyrrolo[1,2-c:2',1'-f][1,3,2]diazaborinin-10-yl)benzoate (**BDP**).

To a solution of **BOD-Chol** (140 mg, 0.14 mmol) and benzaldehyde (60 μL, 0.56 mmol) in 10 mL dry toluene in a thick-walled pressure bottle with molecular sieve, 710 μL glacial acetic acid and 710 μL piperidine were added. The mixture was heated in the closed bottle at 115 ^{o}C for 2.5 h. After cooling to room temperature, the organic volatiles were evaporated. The residue was purified by silica gel column chromatography [hexanes/ethyl acetate, 10:1 (v/v)]. The resultant solid was dissolved in a small amount of THF and from recrystallized diethyl ether to afford pure **BDP** as a dark blue solid (81 mg, 50% yield). ^{1}H-

NMR (500MHz, $CDCl_3$): δ 0.73 (s, 3H), 0.87 (q, 6H), 0.95 (d, 3H), 1.03-1.42 (m, 10H), 1.48 (s, 6H), 1.50-1.59 (m, 6H), 1.63 (m, 5H), 1.84 (m, 3H), 2.00 (m, 2H), 2.07 (m, 3H), 2.55 (d, 2H), 4.95 (m, 1H), 5.49 (d, 1H), 7.37 (m, 2H), 7.4 (m, 6H), 7.69 (d, 4H), 7.72 (d, 2H), 8.18 (d, 2H), 8.25 (d, 2H).

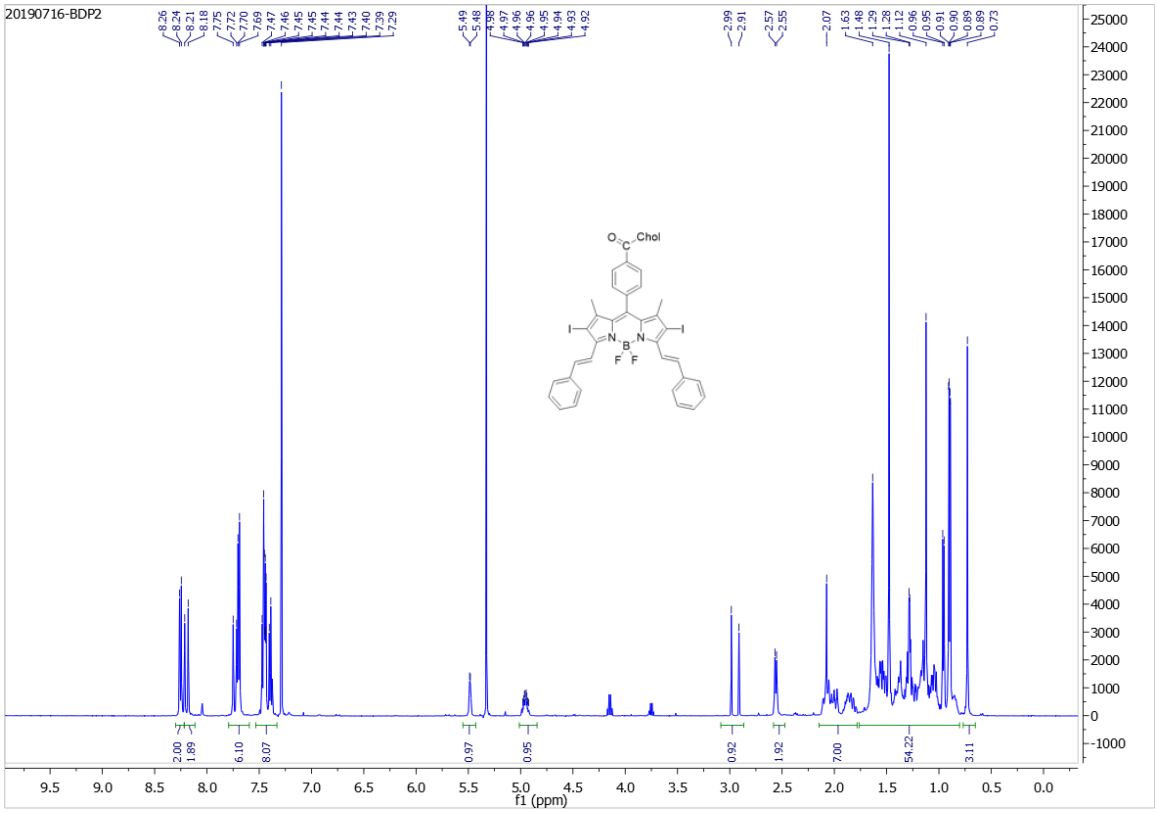

Figure 5-13. ^{1}H-NMR spectrum of **BDP**.

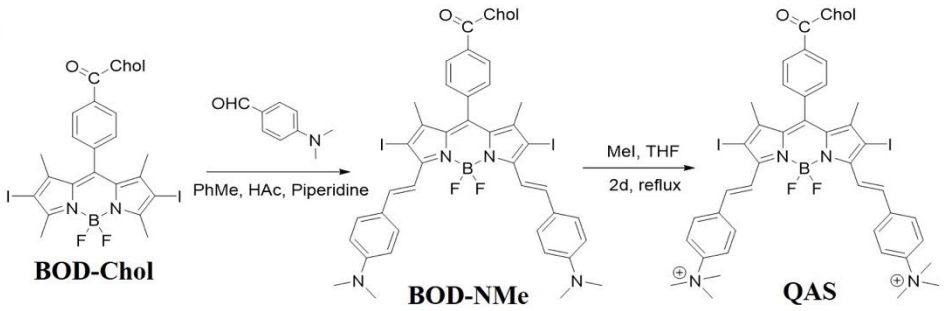

Figure 5-14. Synthesis route of **QAS.**

Preparation of Cholest-5-en-3-ol (3β) 4-(3,7-bis((E)-4-(dimethylamino)styryl)-5,5-difluoro-2,8-diiodo-1,9-dimethyl-5H-4l4,5l4-dipyrrolo[1,2-c:2',1'-f][1,3,2]diazaborinin-10-yl)benzoate (**BOD-NMe**).

To a solution of **BOD-Chol** (140 mg, 0.14 mmol) and 4-dimethylaminobenzaldehyde (350 mg, 2.35 mmol) in 10 mL dry toluene in a thick-walled pressure bottle with molecular sieve, 710 μL glacial acetic acid and 710 μL piperidine were added. The mixture was heated in the closed bottle at 115 oC for 4 h. After removal of organic volatles, the residue was purified by silica gel column chromatography with CHCl3/MeOH = 15:1 (v/v). The solid product was recrystallized in diethyl ether to afford **BOD-NMe** as a gray solid (105 mg, 60% yield)

Preparation of ((4-((E)-2-(5,5-difluoro-2,8-diiodo-10-(4-(cholest-5-en-3-oxycarbonyl)phenyl)-1,9-dimethyl-7-((E)-4-(trimethylammonio)styryl)-5H-4l4,5l4-dipyrrolo[1,2-c:2',1'-f][1,3,2]diazaborinin-3-yl)vinyl)phenyl)dimethyl-l4-azaneyl)methylium diiodide (**QAS**).

A solution of **BOD-NMe** (100 mg, 0.08 mmol) and methyl iodide (2 mL, 32 mmol) in 10 mL dry THF in a closed thick-walled pressure bottle was heated at 70 ^{o}C for 2 days. The solvents were evaporated. The solid was suspended in CH_2Cl_2 and then centrifugated at 14000 rpm for 15 min. The solid was dissolved in DMF and then centrifugated at 14000 rpm for 15 min. The solution was evaporated to afford **QAS** as a dark blue solid (110 mg, 0.07 mmol, 90% yield). ^{1}H-NMR (DMSO-d_6, 500 MHz): δ 0.65 (s, 3H), 0.86 (q, 6H), 0.88

(d, 3H), 1.03 (s, 3H), 1.12 (m, 2H), 1.30 (m, 6H), 1.34 (s, 3H), 1.41 (m, 6H), 1.50 (m, 6H), 1.74 (m, 4H), 1.95 (m, 4H), 3.58 (m, 3H), 3.62 (m, 18H), 4.76 (m, 1H), 5.41 (d, 1H), 7.53 (d, 2H), 7.66 (d, 2H), 7.87 (d, 4H), 8.02 (m, 6H), 8.16 (d, 2H)

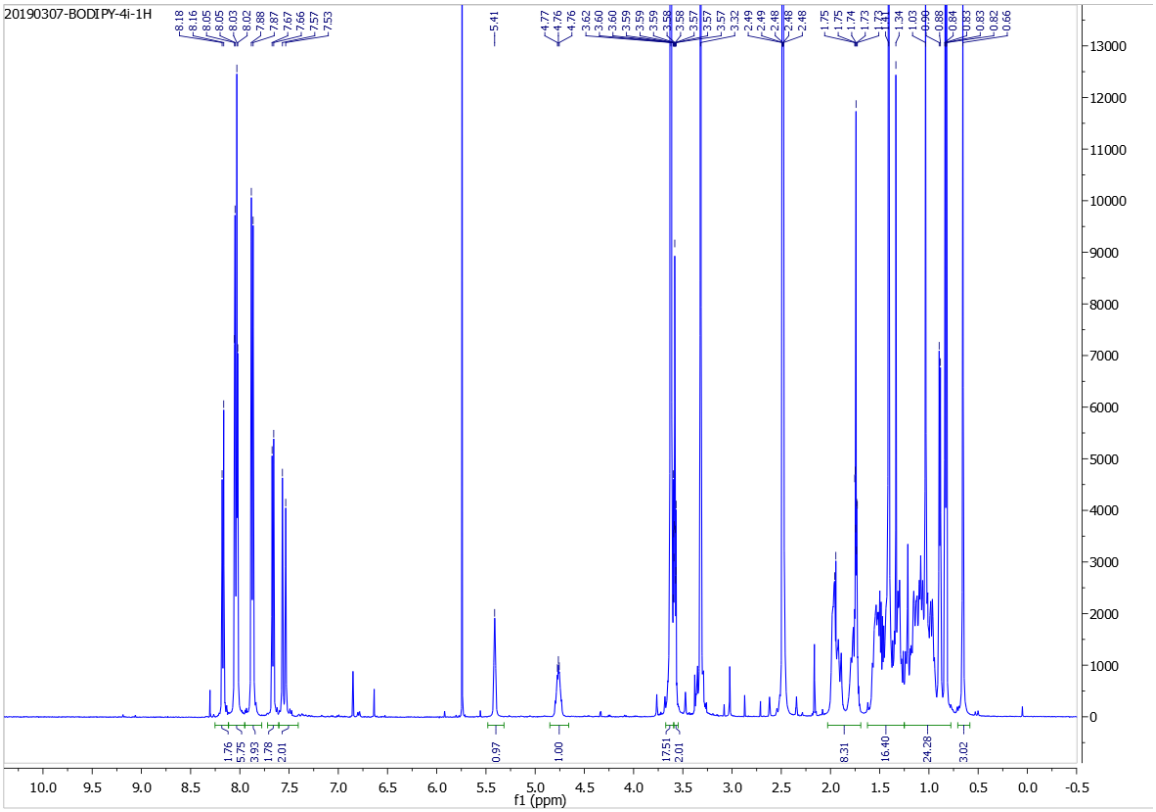

Figure 5-15. ^{1}H-NMR spectrum of QAS

5.4.2 Cellular uptake and subcellular localization

The subcellular localization was studied by staining QAS or BDP treated CT26 cells with both lysotracker DND-26 and mitotracker. 10^5 cells were seeded in live-cell imaging dishes and incubated with 100nM QAS or BDP for 24 h, then stained by 5 μM mitotracker and lysotracker before imaging with a confocal microscope.

5.4.3 PDT induced apoptosis and necrosis

CT26 cells were seeded in 96 well plates (2500 cells per well) and incubated with QAS or BDP at different concentrations for 24 h. Then the medium was removed and cells were washed by PBS once. Fresh culture medium was then added to each well and groups need light irradiation were irradiated at 650 nm for 15 min. Cells were further incubated for another 48 h. Cell viability was tested by MTS assay.

CT26 cells seeded in 6 well plates (10^5 cells per well) were incubated with 40 nM QAS or BDP for 24 h before 90 mW/cm^2 light irradiation for 15 min. Then further incubated for 24 h in fresh medium without photosensitizers. Cells were harvested and washed with PBS twice, then stained with annexin V and PI in dark for 15 min at room temperature before analysis using flow cytometry.

5.4.4 Cell cycle analysis

CT26 cells seeded in 6 well plates (10^5 cells per well) were incubated with 40 nM QAS or BDP for 24 h. Medium was then removed, and cells were washed by 2 mL PBS once. Fresh medium without photosensitizers was added to each well and light treatment groups were irradiated 90 mW/cm^2 for 15 min.

Cells were further incubated for 24 h and harvested. Harvested cells were washed with PBS twice and fixed with 70% ethanol for 1 h at 4 ^{o}C. Ethanol was then removed and fixed cells were stained with stain buffer for 15min at room temperature in dark before analysis using flow cytometry.

5.4.5 Singlet oxygen generation and cellular ROS production

CT26 cells seeded in 6 well plates (10^5 cells per well) were incubated with 40 nM QAS or BDP for 6 h. Then cells were washed by FBS free RPMI1640 medium twice, incubated with SOSG or H_2DCF for 30 min, irradiated for another 15 min. Cells were collected, washed with PBS three times before flow cytometry analysis or confocal imaging.

5.4.6 Lysosome disruption

10^5 CT26 cells were treated by QAS or BDP at different concentrations for 6 h and stained with 5 μM acridine orange for 30 min. Then cells were washed by culture medium twice and further incubated in fresh culture medium for 30 min to remove excess dyes before 15 min light irradiation. Cells were analyzed using flow cytometry or confocal imaging.

5.4.7 Circulation and tumor accumulation

Micelles containing 0.2 mg QAS-nPS were intravenously dosed to 8-week old CT26 tumor-bearing mice. Mice were sacrificed at different time points, plasma, tumors, and other organs were collected and imaged by IV-IS through cy5.5 channel.

5.4.8 *In vivo* efficacy

36 6-week old male balb/c mice were inoculated with 2 million CT26 cells in the left flank of each mouse. When tumor size reaches 100-150 mm^3 on Day 7, mice were randomly distributed into 6 groups. 0.2 mg **QAS** or **BDP** (10 mg/kg dosage) in DMSO/PBS (v/v,

1:100) were intravenously dosed to each mouse in treatment groups. 24 h later, the tumors were irradiated (670 nm, 100 mW/cm^2) for 30 min. This treatment cycle was repeated twice every other day with each injection given 24 h after previous light irradiation. All mice were sacrificed when one mouse in the PBS group reached 2000 mm^3. All tumors were collected, photographed, and weighed.

5.5 References

1. Repnik, U.; Česen, M. H.; Turk, B., Lysosomal membrane permeabilization in cell death: concepts and challenges. *Mitochondrion* **2014,** *19*, 49-57.

2. Boya, P.; Kroemer, G., Lysosomal membrane permeabilization in cell death. *Oncogene* **2008,** *27* (50), 6434-6451.

3. Repnik, U.; Stoka, V.; Turk, V.; Turk, B., Lysosomes and lysosomal cathepsins in cell death. *Biochimica et Biophysica Acta (BBA)-Proteins and Proteomics* **2012,** *1824* (1), 22-33.

4. Lucky, S. S.; Soo, K. C.; Zhang, Y., Nanoparticles in photodynamic therapy. *Chemical reviews* **2015,** *115* (4), 1990-2042.

5. Wang, F.-X.; Chen, M.-H.; Lin, Y.-N.; Zhang, H.; Tan, C.-P.; Ji, L.-N.; Mao, Z.-W., Dual functions of cyclometalated iridium (III) complexes: anti-metastasis and lysosome-damaged photodynamic therapy. *ACS applied materials & interfaces* **2017,** *9* (49), 42471-42481.

6. Tian, Z.; Li, J.; Zhang, S.; Xu, Z.; Yang, Y.; Kong, D.; Zhang, H.; Ge, X.; Zhang, J.; Liu, Z., Lysosome-targeted chemotherapeutics: half-sandwich ruthenium (II) complexes that are selectively toxic to cancer cells. *Inorganic chemistry* **2018,** *57* (17), 10498-10502.

7. Zhang, D.-Y.; Zheng, Y.; Tan, C.-P.; Sun, J.-H.; Zhang, W.; Ji, L.-N.; Mao, Z.-W., Graphene oxide decorated with Ru (II)–polyethylene glycol complex for lysosome-targeted imaging and photodynamic/photothermal therapy. *ACS applied materials & interfaces* **2017,** *9* (8), 6761-6771.

8. Zhang, D.-Y.; Zheng, Y.; Zhang, H.; He, L.; Tan, C.-P.; Sun, J.-H.; Zhang, W.; Peng, X.; Zhan, Q.; Ji, L.-N., Ruthenium complex-modified carbon nanodots for lysosome-targeted one-and two-photon imaging and photodynamic therapy. *Nanoscale* **2017,** *9* (47), 18966-18976.

9. Tian, J.; Ding, L.; Ju, H.; Yang, Y.; Li, X.; Shen, Z.; Zhu, Z.; Yu, J. S.; Yang, C. J., A multifunctional nanomicelle for real-time targeted imaging and precise near-infrared cancer therapy. *Angewandte Chemie International Edition* **2014,** *53* (36), 9544-9549.

10. Ramu, V.; Gautam, S.; Kondaiah, P.; Chakravarty, A. R., Diplatinum (II) Catecholate of Photoactive Boron-Dipyrromethene for Lysosome-Targeted Photodynamic Therapy in Red Light. *Inorganic chemistry* **2019,** *58* (14), 9067-9075.

11. Berg, K.; MADSLIEN, K.; BOMMER, J. C.; OFTEBRO, R.; WINKELMAN, J. W.; MOAN, J., Light induced relocalization of sulfonated meso-tetraphenylporphines in NHIK 3025 cells and effects of dose fractionation. *Photochemistry and photobiology* **1991,** *53* (2), 203-210.

12. Peng, Q.; Farrants, G.; Madslien, K.; Bommer, J.; Moan, J.; Danielsen, H.; Nesland, J., Subcellular localization, redistribution and photobleaching of sulfonated aluminum phthalocyanines in a human melanoma cell line. *International journal of cancer* **1991,** *49* (2), 290-295.

13. Lin, C. W.; Shulok, J. R.; Kirley, S. D.; Bachelder, C. M.; Flotte, T. J.; Sherwood, M. E.; Cincotta, L.; Foley, J. W., Photodynamic destruction of lysosomes mediated by Nile blue photosensitizers. *Photochemistry and photobiology* **1993,** *58* (1), 81-91.

14. Kamkaew, A.; Lim, S. H.; Lee, H. B.; Kiew, L. V.; Chung, L. Y.; Burgess, K., BODIPY dyes in photodynamic therapy. *Chemical Society Reviews* **2013,** *42* (1), 77-88.

15. Detty, M. R.; Merkel, P. B., Chalcogenapyrylium dyes as potential photochemotherapeutic agents. Solution studies of heavy atom effects on triplet yields, quantum efficiencies of singlet oxygen generation, rates of reaction with singlet oxygen, and emission quantum yields. *Journal of the American Chemical Society* **1990,** *112* (10), 3845-3855.

16. Wan, S.; Parrish, J. A.; Anderson, R. R.; Madden, M., Transmittance of nonionizing radiation in human tissues. *Photochemistry and photobiology* **1981,** *34* (6), 679-681.

17. Duan, X.; Chan, C.; Guo, N.; Han, W.; Weichselbaum, R. R.; Lin, W., Photodynamic therapy mediated by nontoxic core–shell nanoparticles synergizes with immune checkpoint blockade to elicit antitumor immunity and antimetastatic effect on breast cancer. *Journal of the American Chemical Society* **2016,** *138* (51), 16686-16695.

18. Duan, X.; Chan, C.; Han, W.; Guo, N.; Weichselbaum, R. R.; Lin, W., Immunostimulatory nanomedicines synergize with checkpoint blockade immunotherapy to eradicate colorectal tumors. *Nature communications* **2019,** *10* (1), 1-15.

19. Guo, S.; Zhang, H.; Huang, L.; Guo, Z.; Xiong, G.; Zhao, J., Porous material-immobilized iodo-Bodipy as an efficient photocatalyst for photoredox catalytic organic reaction to prepare pyrrolo [2, 1-a] isoquinoline. *Chemical Communications* **2013,** *49* (77), 8689-8691.